

**POLYVINYLIDENE FLUORIDE/CLAY
NANOCOMPOSITES: PREPARATION AND
CHARACTERIZATION**

A THESIS
SUBMITTED TO THE
UNIVERSITY OF PUNE
FOR THE DEGREE OF
DOCTOR OF PHILOSOPHY
(IN PHYSICS)

BY
PRIYA. L.
POLYMER SCIENCE AND ENGINEERING DIVISION,
NATIONAL CHEMICAL LABORATORY,
PUNE 411008,
INDIA

JUNE 2005

CERTIFICATE

Certified that the work incorporated in the thesis, “**POLYVINYLIDENE FLUORIDE/CLAY NANOCOMPOSITES: PREPARATION AND CHARACTERIZATION**”, submitted by Mrs. Priya. L. was carried out by the candidate under my supervision. Such material as has been obtained from other sources has been duly acknowledged in the thesis.

(Dr. (Mrs.) Jyoti P. Jog)

Research Guide

Polymer Science and Engineering Division

National Chemical Laboratory,

Pune- 411008.

DECLARATION

I hereby declare that the work presented in the thesis entitled “**POLYVINYLIDENE FLUORIDE/CLAY NANOCOMPOSITES: PREPARATION AND CHARACTERIZATION**”, submitted for Ph. D. Degree to the University of Pune, has been carried out by me at National Chemical Laboratory, Pune under the supervision of Dr. (Mrs.) Jyoti P. Jog. The work is original and has not been submitted in part or in full by me for any degree or diploma to this or any other University.

Date:

National Chemical Laboratory

Pune-411008

(Priya. L.)

Dedicated to my parents

ACKNOWLEDGEMENTS

I would like to express my gratitude to Dr. Jyoti P. Jog for her invaluable guidance, constant encouragement, deep concern and affection. I learnt a great deal from interacting with her.

It is my honour to acknowledge Dr. S. Sivaram, Director, NCL, and Dr. Paul Ratnaswamy, Ex-Director, NCL, for giving me an opportunity to work in NCL. I would like to acknowledge Dr. M. G. Kulkarni, Head, Polymer Science and Engineering Division and Dr. B. D. Kulkarni, Head, Chemical Engineering Division for their cooperation.

I would like to thank Dr. C. Ramesh, Dr. Veda Ramaswamy, Mrs. Renu Parischa, and Mrs. Deepa Dhobale for their kind cooperation. I would also like to express my thanks to Dr. M. R. Anantharaman (Cochin University of Science and Technology), Dr. Raghu (CMET, Trisoor) and Dr. A. D. Kulkarni of IIT (Bombay). I would like to express my debt and gratitude to many of my colleagues and friends. It is my pleasure to thank my lab mates, Dr. (Mrs.) Neelima Bulakh, Mrs. Sangeeta Hambir, Mr. Rajendra Kalgaonkar and Mr. Santosh Wanjale. It was a wonderful experience to work with them. Many thanks are also due to my friends Subhangi, Smitha, Shailesh, Suhas, Grace, Mohan, Vipin, Bhoje and Malli. I would like to thank all NCL staff in particular Mr. Borkar, Mr. Dinadyalan, Mr. Dhupe, for their cooperation.

I greatly acknowledge the financial assistance from Council of Scientific and Industrial Research (CSIR) for providing a research fellowship for carrying out the doctoral work.

Table of Contents

List of Figures	vii
List of Tables	xii
List of Abbreviations	xiv
List of Symbols	xv
Abstract	1
Chapter 1	6
1 Introduction	6
1.1 Polymer Nanocomposites	6
1.2 Layered Silicates	6
1.3 Montmorillonite	8
1.3.1 Structure and Morphology	8
1.3.2 Cation Exchange	9
1.3.3 Cation Exchange Capacity	10
1.4 Methods of Preparation of Nanocomposites	10
1.5 Types of Nanocomposite	10
1.6 Literature Search	12
1.6.1 Types of Polymers used in Preparation of Nanocomposite	12
1.6.2 Thermodynamics of Intercalation Process	13
1.6.3 Theoretical Models	14
1.6.4 Characterization Techniques	15
1.6.4.1 X-ray Diffraction	15
1.6.4.2 Transmission Electron Microscopy (TEM)	16
1.6.4.3 Nuclear Magnetic Resonance (NMR)	16
1.6.4.4 Morphology	17
1.6.4.4.1 Crystallinity, Crystallization, and Polymorphism	17
1.6.4.4.2 Optical Properties	18
1.6.5 Properties of Nanocomposites	18
1.6.5.1 Thermal Properties	18
1.6.5.1.1 Melting Point	18
1.6.5.1.2 Thermal Stability and Degradation	18

1.6.5.1.3	Coefficient of Thermal Expansion (CTE)	19
1.6.5.1.4	Heat Distortion Temperature (HDT)	19
1.6.5.2	Mechanical Properties	20
1.6.5.2.1	Modulus and Strength	20
1.6.5.2.2	Creep Studies	20
1.6.5.3	Dynamic Mechanical Properties - Storage Modulus and $\tan \delta$	21
1.6.5.4	Melt Rheology	22
1.6.5.4.1	Linear rheological properties	22
1.6.5.4.2	Nonlinear Rheological Properties	24
1.6.5.5	Electrical Properties	24
1.6.5.6	Flammability and fire retardant property	25
1.6.5.7	Barrier Properties	25
1.7	Polyvinylidene Fluoride	26
1.7.1	Chemistry	26
1.7.2	Phases, Preparation routes, Crystallization and Crystal Structure	26
1.7.3	XRD peaks for various phases of PVDF	28
1.7.4	IR Vibration modes	29
1.7.5	Morphology	30
1.7.6	Thermal Properties	30
1.7.7	Crystallinity	30
1.7.8	Viscoelastic Properties	30
1.7.9	Mechanical Properties	31
1.7.10	Electrical Properties	32
1.7.11	Dielectric Behavior	32
1.7.12	Ferroelectric Properties	33
1.7.13	Piezoelectricity and pyroelectricity	34
1.7.14	Other Properties	34
1.8	PVDF Composites	34
1.9	Scope of Present Investigation	36
1.10	Objectives	36

Chapter 2	60
2 Experimental Details, Characterization Techniques and Analysis	60
2.1.1 PVDF Grade SOLEF 1008	60
2.1.2 PVDF Grade HYLAR 460	60
2.1.3 Organically Modified Clays	61
2.2 Melt Compounding Techniques	63
2.2.1 Batch Mixer	63
Sample preparation conditions	63
2.2.2 Twin Screw Extruder	63
2.3 Sample Preparation Techniques	64
2.3.1 Compression Molding	64
2.3.2 Injection Molding	64
2.4 Characterization Techniques	65
2.4.1 X-ray Diffraction (XRD)	65
2.4.2 Transmission Electron Microscope (TEM)	67
Sample preparation	68
2.4.3 Optical Microscopy	69
2.4.4 Differential Scanning Calorimeter (DSC)	70
2.4.4.1 Non-isothermal Experiments	70
2.4.4.2 Isothermal Crystallization Experiments	71
2.4.5 Fourier Transform Infrared Analysis (FTIR)	73
2.4.6 Mechanical Properties	73
2.4.6.1 Stress-Strain Properties	73
2.4.7 Impact Properties	74
2.4.8 Dynamic Mechanical Analysis (DMA)	75
2.4.9 Coefficient of Thermal Expansion	77
2.4.10 Creep Studies	78
2.4.11 Melt Rheology	79
2.4.12 Dielectric Analysis (DEA)	80

Chapter 3	84
3 Melt intercalated PVDF (SOLEF 1008)/Clay Nanocomposites	84
3.1 Introduction	84
3.2 Results and Discussion	84
3.2.1 Structure of Nanocomposites	84
3.2.1.1 X-ray Diffraction (XRD)	84
3.2.1.2 Fourier Transform Infrared Spectroscopy (FTIR)	87
3.2.2 Morphology	88
3.2.2.1 Optical Microscopy	88
3.2.3 Thermal Properties- Differential Scanning Calorimetry	90
3.2.3.1 Melting and Non-Isothermal Crystallization	90
3.2.3.2 Isothermal Crystallization	91
3.2.4 Dynamic Mechanical Analysis	92
3.2.5 Coefficient of Thermal Expansion	96
3.2.6 Melt Rheology	97
3.2.7 Stability of β Phase in PVDF Nanocomposites	101
3.3 Conclusions	103
Chapter 4	106
4 PVDF (SOLEF 1008)/Clay Nanocomposites: Effect of modifier and Concentration	106
4.1 Introduction	106
4.2 Melt intercalation using Batch mixer	106
4.2.1 Results and Discussion	107
4.2.1.1 Structure of Nanocomposites	107
4.2.1.1.1 X-ray Diffraction	107
4.2.1.1.2 Transmission Electron Microscopy	109
4.2.1.2 Morphology	111
4.2.1.3 Thermal Properties-Differential Scanning Calorimetry	112
4.2.1.3.1 Melting and Non-Isothermal Crystallization	112
4.2.1.3.2 Isothermal Crystallization	113
4.2.1.4 Dynamic Mechanical Analysis	114

4.2.1.5	Coefficient of Thermal Expansion	117
4.2.1.6	Melt Rheology	118
4.2.1.7	Dielectric Properties	121
4.2.1.8	Stability of β Phase in PVDF/20A Nanocomposites	123
4.3	Effect of Modifier Treatment	124
4.3.1	Results and Discussion	125
4.3.1.1	Structure of Composites	125
4.3.1.2	Morphology- Optical Microscopy	126
4.3.1.3	Thermal Properties- Differential Scanning Calorimetry	128
4.3.1.3.1	Melting and Non-isothermal Crystallization	128
4.3.1.3.2	Isothermal Crystallization	129
4.3.1.4	Dynamic Mechanical Analysis	130
4.3.1.5	Linear Rheology	131
4.3.1.6	Dielectric Properties	132
4.4	Effect of Modifier Concentration	134
4.5	PVDF/20A Extruded Nanocomposites	138
4.5.1	Results and Discussion	139
4.5.1.1	Structure of Nanocomposites- X-Ray Diffraction	139
4.5.1.2	Optical Microscopy	141
4.5.1.3	Differential Scanning Calorimetry	143
4.5.1.3.1	Melting and Non-isothermal Crystallization	143
4.5.1.3.2	Isothermal Crystallization	144
4.5.1.4	Static Mechanical Properties	146
4.5.1.4.1	Tensile Properties	146
4.5.1.4.2	Impact Properties	146
4.5.1.5	Dynamic Mechanical Analysis	147
4.5.1.6	Melt Rheology	149
4.6	Conclusions	150

Chapter 5	154
5 PVDF (HYLAR 460)/Clay Nanocomposites: Properties and Creep Studies	154
5.1 Introduction	154
5.2 Results and Discussion	154
5.2.1 Structure of Nanocomposites	154
5.2.1.1 X-ray Diffraction	154
5.2.1.2 Transmission Electron Microscopy	156
5.2.2 Morphology	158
5.2.3 Thermal Properties- Differential Scanning Calorimetry	159
5.2.4 Static Mechanical properties	159
5.2.4.1 Tensile Properties	159
5.2.4.2 Impact Properties	160
5.2.5 Dynamic Mechanical Analysis	161
5.2.6 Creep Studies	163
5.3 Conclusions	170
Chapter 6	173
6 Conclusions and Scope for Future Work	173
6.1 Conclusions	173
6.2 Scope for Future Work	174
List of Publications	176

List of Figures

Figure 1.3.1: Structure of Montmorillonite	8
Figure 1.5.1: Types of Nanocomposites	11
Figure 1.7.1: Dielectric relaxations in PVDF	32
Figure 2.4.1: Bragg's law of X-ray diffraction	66
Figure 2.4.2: Bragg Brentano Para focusing geometry of XRD in reflection in mode	67
Figure 2.4.3: Basic components of a Transmission Electron Microscope	68
Figure 2.4.4: Melting and Non-isothermal Crystallization	71
Figure 2.4.5: Isothermal Crystallization	72
Figure 2.4.6: Stress-strain curve	74
Figure 2.4.7: Linear and Non-linear region of testing	75
Figure 2.4.8: Principle of dynamic testing	76
Figure 2.4.9: A Typical Creep Curve	78
Figure 2.4.10: Frequency response curve of G' and G''	79
Figure 2.4.11: Sample holder for dielectric Testing	81
Figure 3.2.1: XRD of 6A and PVDF/6A Nanocomposites	85
Figure 3.2.2: XRD showing α phase of pristine PVDF and β phase of PVDF in PVDF/6A nanocomposites	87
Figure 3.2.3: FTIR of PVDF and one of the nanocomposites containing 3% of 6A showing α and β phases respectively	88
Figure 3.2.4: Optical Micrograph of PVDF crystallized at 148 °C. Magnification 32X	89
Figure 3.2.5: Optical Micrograph of PNC1.5 crystallized at 152 °C. Magnification 32X	89
Figure 3.2.6: Optical Micrograph of PNC5 crystallized at 152 °C. Magnification 32X	90
Figure 3.2.7: $t_{1/2}$ vs. T_c of PVDF/6A nanocomposites	92
Figure 3.2.8: Temperature dependence of storage modulus (E') for PVDF and PVDF/6A clay nanocomposites	93

Figure 3.2.9: Tan δ vs. temperature curves for PVDF and PVDF/ 6A clay nanocomposites	94
Figure 3.2.10: Variation of Coefficient of Thermal Expansion with percentage of clay for PVDF/6A nanocomposites	96
Figure 3.2.11: Frequency response of storage modulus (G') at 210 °C for PVDF/6A nanocomposites	97
Figure 3.2.12: Frequency response of loss modulus (G'') at 210 °C for PVDF/6A nanocomposites	98
Figure 3.2.13: Frequency response of complex viscosity (η^*) at 210 °C for PVDF/6A nanocomposites	98
Figure 3.2.14: Master curve overlay of G' of PVDF and PVDF/ 6A shifted to 210 °C	100
Figure 3.2.15: XRD of samples annealed at 185 °C	102
Figure 4.2.1: XRD of 20A and PVDF/20A nanocomposites	107
Figure 4.2.2: XRD showing α phase of pristine PVDF and β phase of PVDF in PVDF/20A nanocomposites	109
Figure 4.2.3: Transmission electron micrograph of PN5 nanocomposite at two different magnifications	110
Figure 4.2.4: Optical Micrograph of PVDF crystallized at 148 °C. Magnification 32X	111
Figure 4.2.5: Optical Micrograph of PN1.5 crystallized at 152 °C. Magnification 32X	111
Figure 4.2.6: Optical Micrograph of PN5 crystallized at 152 °C. Magnification 32X	112
Figure 4.2.7: $t_{1/2}$ vs. T_c of PVDF/20A nanocomposites	114
Figure 4.2.8: Temperature dependence of storage modulus (E') for PVDF and PVDF/20A clay nanocomposites	115
Figure 4.2.9: Tan δ vs. temperature curves for PVDF and PVDF/ 20A clay nanocomposites	116
Figure 4.2.10: Variation of Coefficient of Thermal Expansion with percentage of clay for PVDF/20A nanocomposites	117

Figure 4.2.11: Frequency response of storage modulus (G') at 210 °C for PVDF/20A nanocomposites	118
Figure 4.2.12: Frequency response of loss modulus (G'') at 210 °C for PVDF/20A nanocomposites	119
Figure 4.2.13: Frequency response of complex viscosity (η^*) at 210 °C for PVDF/20A nanocomposites	119
Figure 4.2.14: Master curve overlay of storage modulus (G') of PVDF and PVDF/ 20A shifted to 210 °C	121
Figure 4.2.15: Comparison of dielectric constant (ϵ') of PVDF/20A nanocomposites	122
Figure 4.2.16: Comparison of loss factor (ϵ'') of PVDF/20A nanocomposites	123
Figure 4.2.17: XRD of retention of PVDF and PN5 after annealing at 185°C showing α phase for PVDF and β phase for PN5	124
Figure 4.3.1: XRD of Na^+ -clay (a) and PVDF/ Na^+ composite (b)	125
Figure 4.3.2: XRD of PVDF, nanocomposites PNC5, PN% and PVDF/ Na^+ showing α phase in PVDF and PVDF/ Na^+ and β phase in PN5 and PNC5	126
Figure 4.3.3: Optical Micrograph of PVDF crystallized at 148 °C. Magnification 32X	127
Figure 4.3.4: Optical Micrograph of PVDF/ Na^+ crystallized at 148 °C. Magnification 32X	127
Figure 4.3.5: Optical Micrograph of PNC5 crystallized at 152 °C. Magnification 32X	128
Figure 4.3.6: Optical Micrograph of PN5 crystallized at 152 °C. Magnification 32X	128
Figure 4.3.7: Isothermal crystallization of PVDF and PVDF/clay composites	129
Figure 4.3.8: Temperature dependence of storage modulus (E') for PVDF and PVDF composites with Na^+ , 6A, 20A	130
Figure 4.3.9: Frequency response of storage modulus (G') at 210°C for PVDF nanocomposites (PVDF/6A, PVDF/20A and micro composites PVDF/ Na^+)	131

Figure 4.3.10: Comparison of dielectric constant (ϵ') of PVDF, nanocomposites PVDF/6A, PVDF/20A and micro composite PVDF/Na ⁺	133
Figure 4.3.11: Comparison of loss factor (ϵ'') of PVDF, nanocomposites PVDF/6A, PVDF/20A and micro composite PVDF/Na ⁺	134
Figure 4.4.1: Schematic representation of formation of intercalated PLS nanocomposite – polymer chains have infiltrated the silicate layers increasing the effective volume on the layered silicate.	137
Figure 4.5.1: XRD of 20A and PVDF (SOLEF 1008)/20A extruded nanocomposites	139
Figure 4.5.2: XRD showing α phase of pristine PVDF (SOLEF 1008) and β phase of PVDF (SOLEF 1008) in PVDF (SOLEF 1008)/20A extruded nanocomposites	140
Figure 4.5.3: Comparison of d spacing with percentage of clay for samples prepared using batch mixer and twin-screw extruder	141
Figure 4.5.4: Optical Micrograph of PVDF at 148 °C. Magnification 32X	142
Figure 4.5.5: Optical Micrograph of TPN1.5 at 150 °C. Magnification 32X	142
Figure 4.5.6: Optical Micrograph of TPN7 at 157 °C. Magnification 32X	143
Figure 4.5.7: Isothermal crystallization of PVDF (SOLEF 1008)/20A extruded nanocomposites	145
Figure 4.5.8: Temperature dependence of storage modulus (E') for extruded PVDF(SOLEF 1008) and PVDF(SOLEF 1008)/20A clay nanocomposites	147
Figure 4.5.9: Tan δ vs. temperature curves for extruded PVDF (SOLEF 1008) and PVDF (SOLEF 1008)/20A clay nanocomposites	148
Figure 4.5.10: Master curve overlay of storage modulus (G') of extruded PVDF (SOLEF 1008) and PVDF (SOLEF 1008)/20A shifted to 210 °C	149
Figure 5.2.1: XRD of 20A and PVDF (HYLAR 460)/20A extruded Nanocomposites	155

Figure 5.2.2: XRD showing α phase of pristine PVDF (HYLAR 460) and β phase of PVDF in extruded PVDF (HYLAR 460)/20A nanocomposites	156
Figure 5.2.3: Transmission electron micrograph of P7 nanocomposite	157
Figure 5.2.4: Optical Micrograph of P0 crystallized at 141 °C. Magnification 32X	158
Figure 5.2.5: Optical Micrograph of P1.5 crystallized at 144 °C. Magnification 32X	158
Figure 5.2.6: Temperature dependence of storage modulus (E') for PVDF (HYLAR 460) and PVDF (HYLAR 460)/20A nanocomposites	161
Figure 5.2.7: Tan δ vs. temperature curves for PVDF (HYLAR 460) and PVDF (HYLAR 460)/20A clay nanocomposites	162
Figure 5.2.8: Creep curve of PVDF at 15% yield stress	164
Figure 5.2.9: Strain vs. time graph for PVDF and one nanocomposite (P7) at room temperature for 15% of yield stress	166
Figure 5.2.10: Strain vs. time graph for PVDF and one nanocomposite (P7) at 100 °C for 15% of yield stress	166
Figure 5.2.11: Time vs. compliance at 100 °C at 15% yield stress for PVDF and one nanocomposite (P7)	168
Figure 5.2.12: Comparison of short-term compliance constant (D_0) as function of percentage of clay and temperature	169

List of Tables

Table 1.7.1: XRD peaks of the different phases of PVDF	28
Table 1.7.2: IR vibration modes and their assignments	29
Table 2.1.1: Physical properties of the commercial clays used	62
Table 2.2.1: Extrusion conditions used	64
Table 2.3.1: Temperature settings of the different zones in Injection molding machine	65
Table 3.1.1: Sample codes and compositions of PVDF/6A nanocomposites	84
Table 3.2.1: Non-isothermal melting and crystallization parameters of PVDF and PVDF/6A clay nanocomposites	90
Table 3.2.2: E_c'/E_p' values of PVDF/6A at different temperatures	94
Table 3.2.3: Rheology- Low Frequency behaviour of PVDF/6A nanocomposites at 210 °C	99
Table 3.2.4: Melting parameters for annealed PVDF and PVDF/6A nanocomposites samples	103
Table 4.2.1: Sample code and compositions of PVDF/20A nanocomposites	106
Table 4.2.2: Non-isothermal melting and crystallization parameters of PVDF and PVDF/20A nanocomposites	113
Table 4.2.3: E_c'/E_p' values of PVDF/20A at different temperatures	116
Table 4.2.4: Rheology- Low Frequency behaviour of PVDF/20A nanocomposites at 210 °C	120
Table 4.3.1: E_c'/E_p' values of PVDF/clays (Na ⁺ , 6A, 20A) at different temperatures	131
Table 4.3.2: Rheology- Low frequency behaviour of PVDF/clays (Na ⁺ , 6A, 20A) composites at 210 °C	132
Table 4.4.1: Comparison of intercalation yield of 20A and 6A nanocomposites	135
Table 4.4.2: E_c'/E_p' with respect percentage at room temperature	136
Table 4.4.3: Aspect ratio (f_g) and calculated volume concentration of PVDF/6A and PVDF/20A nanocomposites	138
Table 4.5.1: Non-isothermal melting and crystallization parameters of extruded PVDF and PVDF (SOLEF 1008)/20A nanocomposites	144

Table 4.5.2: Static Mechanical properties of extruded PVDF (SOLEF 1008)/20A Clay Nanocomposites	146
Table 4.5.3: E_c/E_p' values of extruded PVDF (SOLEF 1008)/20A at different temperatures	148
Table 5.1.1: Sample code and compositions of extruded PVDF (HYLAR 460)/20A nanocomposites	154
Table 5.2.1: Non-isothermal melting and crystallization parameters of extruded PVDF (HYLAR 460) and PVDF (HYLAR 460)/20A clay nanocomposites	159
Table 5.2.2: Static Mechanical properties of extruded PVDF (HYLAR 460)/20A Clay Nanocomposites	160
Table 5.2.3: E_c/E_p' values of extruded PVDF (HYLAR 460)/20A at different temperatures	162

List of Abbreviations

CTE	- Coefficient of Thermal Expansion
DMA	- Dynamic Mechanical Analysis
DSC	- Differential Scanning Calorimeter
FTIR	- Fourier Transform Infrared
HDT	- Heat Distortion Temperature
IR	- Infrared
NMR	- Nuclear Magnetic Resonance
OM	- Optical Microscopy
TEM	- Transmission Electron Microscopy
TGA	- Thermo Gravimetric Analysis
SAXS	- Small Angle X-ray Scattering
WAXD	- Wide Angle X-ray Diffraction
WAXS	- Wide Angle X-ray Scattering
XRD	- X-ray diffraction
PVDF	- Polyvinylidene fluoride

List of Symbols

χ	- Interaction parameter
T_c	- Crystallization temperature
T_m	- Melt temperature
E'	- Elastic storage modulus
E''	- Elastic loss modulus
T_g	- Glass transition temperature
G^*	- Shear complex modulus
G'	- Shear storage modulus
G''	- Shear loss modulus
ω	- Frequency
η^*	- Complex Viscosity
a_T	- Horizontal shift factor
b_T	- Vertical shift factor
ϵ'	- Relative permittivity or dielectric constant
ϵ''	- Loss factor of dielectric constant
T_g'	- Secondary glass transition
ΔH_f	- Heat of fusion
ΔH_c	- Heat of crystallization
$t_{1/2}$	- Crystallization half time

Abstract

Polymer nanocomposites is an emerging area in polymer science where the property improvements are obtained by incorporation of nano fillers in the polymer matrix. There are three types of nano fillers, viz., nano particles (three dimensions in nano scale), two-dimensional fillers like, nano tubes and cellulose whiskers and nano clays with single dimension in the nano scale. Nanocomposites consisting of polymer and clay are studied in this thesis. The Clay mineral based nanocomposites are widely investigated because of the natural abundance and lesser cost of clay.

Layered silicate materials consist of natural clays like montmorillonite, hectorite, and saponite as well as synthetic clays such as magadite, mica, laponite, flourohectorite etc. Montmorillonite is the most important clay and is widely used. The layered structure of Montmorillonite consists of a dioctahedral 2:1 layer with charge balancing and exchangeable cations located between the layers. The layer thickness is around 1 nm and the lateral dimension of these layers may vary from 30 nm to several microns. These layers organize themselves to form stacks with a regular Van der Waal gap in between them called interlayer or gallery. Clays are made organophilic to improve compatibility between the polymer and the hydrophilic clay surface.

In contrast to the traditional fillers, the nano clays are found to be effective even at low filler loadings such as 5%. This is due to (1) the high surface area of the nano clays and (2) the possibility of organic modification clays facilitating the dispersion of the clay layers in polymer matrix. The nano size of the clay layers in the polymer matrix, results in markedly improved mechanical, thermal, optical and physico-chemical properties as compared to pristine polymer.

The different techniques such as *solution blending*, *insitu polymerization* and *melt blending* are used for preparation of nanocomposites. Among these methods melt blending is the most commercially viable method for preparation of nanocomposites. Depending on the dispersion level of the clay layers, nanocomposites can be classified as *intercalated nanocomposites* and *exfoliated nanocomposites*. In *intercalated nanocomposites* one or more than one extended chains of the polymer is intercalated between the silicate layers resulting in a well-

ordered morphology with alternating layers of polymer and clay. Here the repetitive multilayer structure is preserved. In *exfoliated nanocomposites* silicate layers are completely delaminated and uniformly dispersed in a continuous polymer matrix.

Polyvinylidene fluoride (PVDF) is a crystalline polymer with a variety of properties. PVDF has been one of the most studied polymers because of its potential application as piezoelectric and pyroelectric materials. It is also being used in non-linear optics, microwave transducers and biomedical applications. These properties combined with high elasticity and processing ability provides a variety of technological applications for this polymer. From the scientific point of view it is an interesting polymer as it exhibits polymorphism with four crystal forms (α , β , γ , δ).

PVDF - layered silicate nanocomposites were prepared by melt compounding of PVDF and organically modified Montmorillonite for the first time. The work presented in this thesis deals with preparation and properties of PVDF/Clay nanocomposites using two organophilic clays and two grades of PVDF. The effect of organic treatment and its contents on the structure and properties of PVDF/Clay nanocomposites was evaluated. The work involves study of crystallization behavior, static and dynamic mechanical properties and dielectric properties.

The entire work is presented in six chapters and the outline of each chapter is given in the foregoing.

Chapter 1: Introduction

The introductory chapter describes the background and the overview of Clay especially Montmorillonite, Clay nanocomposites, Polyvinylidene fluoride (PVDF). This chapter also includes the recent literature on different polymer/clay nanocomposites, the property improvements achieved and different PVDF composites. The scope and objectives of the present work are also discussed.

Chapter 2: Experimental Details, Characterization Techniques and Analysis

This chapter presents the details of the preparation of the nanocomposites and experimental techniques used for characterization. The materials (grade and physical properties) used, the compounding techniques (batch mixer, twin screw extruder),

sample preparation techniques (compression molding, injection molding), etc., are discussed in detail. The nanocomposites prepared are characterized for structure using Wide Angle X-ray Diffraction (WAXD) and Transmission Electron Microscope (TEM). The crystalline morphology is studied by Optical Microscope. Thermal characterization is carried out using Differential Scanning Calorimetry. The static mechanical properties are determined using a Universal Testing Machine (UTM) in tensile mode and an impact Tester. The dynamic properties of the nanocomposites are studied in solid state using a Dynamic Mechanical Analyzer (DMA) and a Dielectric Spectrometer, where as, the rheological behaviour is investigated using a strain-controlled rheometer.

Chapter 3: Melt intercalated PVDF (SOLEF 1008)/Clay Nanocomposites

This chapter presents the results of preparation and characterization of nanocomposites of PVDF (SOLEF 1008) with clay (Cloisite 6A) modified with ditallow dimethyl ammonium salt. The clay has higher Cation Exchange Capacity (CEC) and accordingly higher organic content. The non-isothermal and the isothermal crystallization studies of the nanocomposites show enhanced rate of crystallization of PVDF. The dynamic mechanical analysis indicates improved storage modulus over the entire temperature range studied and the extent of increase is dependent on clay %. The glass transition temperature is found to increase by approximately 6-8 °C indicating restricted chain mobility of the polymer chains in the nanocomposites. The $\tan \delta$ curves exhibit two peaks corresponding to T_g of the polymer and release of constrained amorphous phase. The pseudo solid like behavior observed from the melt frequency sweeps establish the formation of the nanocomposites. The crystallization of PVDF in the β phase with a corresponding increase in the melting point is one of the notable observations. The thermal stability of the observed β form is ascertained from the thermal annealing experiments carried out at 125°C and 185 °C.

Chapter 4: PVDF (SOLEF 1008)/Clay Nanocomposites: Effect of modifier and concentration

This chapter presents results of PVDF (SOLEF 1008)/Clay nanocomposites prepared using organophilic clay (Cloisite 20A), which is modified with ditallow dimethyl ammonium salt. However, the organic content is less as compared to 6A. The nanocomposites are prepared using two different melt processing techniques as well as solution blending. The results of this study indicated that PVDF crystallizes in β form in the presence of organophilic clay irrespective of the method of preparation. The observed improvements in properties as compared to PVDF/6A nanocomposites are explained on the basis of intercalation yield. Dielectric studies indicate decrease in storage dielectric permittivity (ϵ') in the whole range of frequencies studied.

Chapter 5: PVDF (HYLAR 460)/Clay nanocomposites: Properties and Creep Studies

This chapter presents the results of the nanocomposites of a different grade of PVDF i.e., HYLAR 460. The nanocomposites showed increased modulus and formation of β phase similar to earlier results in SOLEF 1008 grade. These nanocomposites are also studied for the creep behavior since this grade is used in offshore pipes and platforms, where long term stability and strength are required. Creep studies at Room Temperature and 100°C shows that the resistance to creep in polymer/clay nanocomposites greatly improves due to the presence of nano-clay layers. The dispersion of nano-clay in the polymer matrix affects both elastic as well as inelastic regions.

Chapter 6: Conclusions and Scope for Future Work

The important conclusions of this work are summarized in this chapter. PVDF/Clay nanocomposites were prepared using two grades of PVDF. The nanocomposites exhibit improved mechanical properties. The formation of β phase in both grades of PVDF in presence of organic clay is one of the important observations. The formation of β phase is observed irrespective of the grade of the PVDF and the organic content of the clay. The annealing studies confirm the thermal

stability of β phase. Creep studies of PVDF grade HYLAR 460 nanocomposites exhibits inhibition in the creep mechanism.

This chapter also explains the future scope of the work.

Chapter 1
Introduction

Chapter 1

1 Introduction

The properties of polymers are often modified with the use of fillers. The property modifications sought include improved stiffness, toughness, barrier properties, fire resistance, and cost reduction. However, the addition of fillers imparts brittleness, opacity, etc., to the polymer and increases density of the polymer.

1.1 Polymer Nanocomposites

Polymer nanocomposites are two-phase materials in which one of the components (filler) at least is in the nanometer scale. There are three types of nano fillers. First one is the nanoparticles in which all three dimensions are in nano scale e.g., semiconductor, metal nanoparticles, colloidal dispersion of polymers etc ^(1, 2). Second one is the two dimensional nanomaterials where in two dimensions of the filler are in nanoscale. Examples are nano tubes and cellulose whiskers that have the third dimension larger, forming elongated structures ^(3, 4). The third variety comprises of the nano clays, which are platelet shaped, with one dimension in nanoscale. This family of nanocomposites can be called as the polymer/clay nanocomposites. The clay mineral based nanocomposites are widely investigated because of the natural abundance, lesser cost and high mechanical strength and chemical resistance. The intercalation chemistry between clay and polymer has been widely studied ^(5, 6). The dispersion of the nanosized particles in the polymer matrix results in markedly improved mechanical, thermal, optical and physico-chemical properties as compared to pristine polymer as first shown by Kojima and coworkers for nylon ⁽⁷⁾.

1.2 Layered Silicates

Layered silicate materials consist of natural clays like montmorillonite, hectorite, and saponite as well as synthetic clays such as magadite, mica, laponite, fluorohectorite etc.

The structural variations among the clay minerals can be understood by considering various physical combinations of tetrahedral and octahedral sheets and the effects of chemical substitution on structural units. The layered silicates contain two-dimensional tetrahedral sheets of composition T_2O_5 (T-tetrahedral cation, normally Si, Al or Fe^{3+}) in which individual tetrahedra is linked with neighboring

tetrahedra by sharing 3 corners each (the basal oxygens) to form a hexagonal mesh pattern. The fourth tetrahedral corner (the apical oxygen) points to a direction normal to the sheet and at the same time forms part of an immediately adjacent octahedral sheet in which individual octahedra are linked laterally by sharing octahedral edges. The common plane of junction between tetrahedral and octahedral sheets consists of shared apical oxygens plus unshared OH⁻ groups that lie at the center of each tetrahedral six fold ring at the same 3-level as the apical oxygens. The octahedral cations are Mg, Al, Fe²⁺ and Fe³⁺, but other medium-sized cations such as Li, Ti, V, Cr, Mn, Co, Ni, Cu, and Zn also occur in some species. The smallest structural unit contains 3 octahedra. If all 3 octahedra are occupied i.e., have octahedral cations at their centers, the sheet is classified as trioctahedral. If only 2 octahedra are occupied and third octahedron is vacant, the sheet is called dioctahedral.

The assemblage formed by linking one tetrahedral sheet with one octahedral sheet is known as **1:1 layer**. **2:1 layer** links 2 tetrahedral sheets with an octahedral sheet. Here the upper tetrahedral sheet must be inverted so that apical oxygen point down and can be shared with octahedral sheet below. Both octahedral anions have some O²⁻, OH⁻ compositions. If the 1:1 or 2:1 layers are not electrostatically neutral, various interlayer materials including individual cations, hydrated cations and hydroxide octahedral groups and sheets neutralize the excess layer charge. The total assemblage of a layer plus interlayer is referred to as a **structure unit**.

In the great majority of layered silicates, the ideal lateral dimensions of the tetrahedral sheets are larger than those of the octahedral sheets, because of the tetrahedral substitutions of Al or Fe³⁺ for Si.

The layered silicate minerals are classified based on layer type, layer charge, and type of interlayer into 8 major groups. The 8 major groups are serpentine-kaolin (1:1 type), talc-pyrophyllite, smectite, vermiculite, mica, brittle mica, chlorite, and sepiolite-palygorskite, which are 2:1 type. Further subdivision into sub-groups and species is made based on octahedral sheet type (dioctahedral and trioctahedral), chemical composition and the geometry of composition of individual layers and interlayers. Montmorillonite, hectorite and saponite are the most commonly used layered silicates belonging to the smectite group.

The smectite minerals, where the charge deficit is balanced by loosely held hydrated cations in the interlayer space between 2:1 layers, have the smallest charge deficit, $x=0.2 - 0.6$. Smectite minerals may be dioctahedral or trioctahedral depending on the predominant cation in the octahedral layer. The amount of water in the interlayer space varies with cation content and the basal spacing may vary between 1.0 -1.8 nm.

1.3 Montmorillonite

1.3.1 Structure and Morphology

Montmorillonite is the most important member of the smectite group. Montmorillonite has a general formula $(M^+_{y.n} H_2O)(Al_{2-y} Mg_y) Si_4 O_{10} (OH)_2$. M^+ is the exchangeable cation (monovalent ion) and nH_2O includes the interlayer water not specifically associated with ions. The layered structure of Montmorillonite consists of a dioctahedral 2:1 layer with charge balancing and exchangeable cations located between the layers.

The structure of the Montmorillonite is shown in the figure 1.3.1 ⁽⁹⁾.

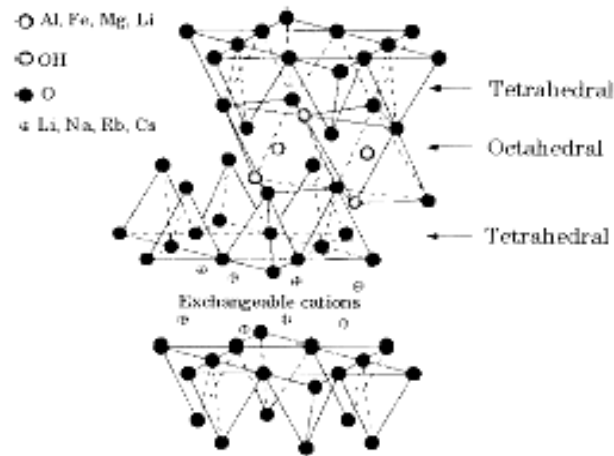


Figure 1.3.1: Structure of Montmorillonite

The layer thickness is around 1 nm and the lateral dimension of these layers may vary from 30 nm to several microns and even larger depending on the particular silicate. These layers organize themselves to form stacks with a regular Van der

Waals gap in between them called interlayer or gallery. Isomorphic substitutions within the layers (for e.g., Al^{3+} replaced by Mg^{2+} or Fe^{2+} replaced by Li^+) generate negative charges that are counterbalanced by alkali or alkaline earth cations situated in the interlayer.

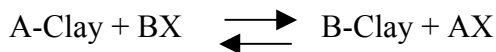
Interlamellar complexes of clay minerals are formed by the introduction of inorganic and organic materials between the structural layers. The relatively weak bondings between the layers as compared with the strong ionic-covalent bonding within the layers facilitate complex formation.

X-ray powder patterns of smectites show mainly basal $00l$ diffractions and two dimensional hk diffraction bands. The 2 dimensional hk bands arise from the random stacking of layers in most smectites. Many of the hk bands do not provide sharp features. The hk diffraction bands of Montmorillonite are not well suited for structure analysis. X-ray structure factors cannot be evaluated directly because of the nature of the diffraction process and because each observed band is a summation of several hk index planes. Precise confirmation of the structure from usual methods of diffraction analysis is difficult because of the variable basal spacings usually found ⁽⁸⁾.

Electron optical studies give additional information. Montmorillonite is seen as finely divided platy forms usually with poorly defined outlines and very crumpled layers. Primary particle comprises of five to ten lamellae.

1.3.2 Cation Exchange

Saturating clay with a particular cation is usually achieved by treating it with an excess of 1N solution of chloride or acetate of the chosen cation. It is generally preferred that the pH of the solution is near 7. H^+ is a cation, which will participate in cation exchange reaction. The exchange reaction can be expressed as follows.



With an excess of B^+ ions in the solution, the reaction is displaced to the right hand side.

1.3.3 Cation Exchange Capacity

For a given layered silicate, the maximum amount of cations that can be exchanged is a constant and is known as cation-exchange capacity (CEC). CEC is generally expressed in milliequivalent (meq)/g or meq/100g. It is also expressed as charge per unit mass. In SI units it is expressed as Coulombs per unit mass. The charge of the layer is not locally constant as it varies from layer to layer and must rather be considered as an average value over the whole crystal. Proportionally, even if a small part of the charge balancing cations is located on the external crystallite surface, the majority of these exchangeable cations are located inside the galleries. When hydrated cations are ion exchanged with organic cations such as more bulky alkylammoniums, it usually results in a larger interlayer spacing.

1.4 Methods of Preparation of Nanocomposites

The different techniques that are used for polymer nanocomposite preparation are solution blending, insitu polymerization and melt blending.

In *solution intercalation/adsorption technique*, the layered silicate is exfoliated into single layers using a solvent in which the polymer is soluble. Due to weak interaction between the layers, it can be easily dispersed in an adequate solvent. The polymer then adsorbs onto the delaminated sheets and when the solvent is evaporated, the sheets reassemble, sandwiching the polymer to form an ordered multilayer structure.

In *in situ intercalative polymerization*, the layered silicate is swollen within the liquid monomer (or a monomer solution). The polymer formation can occur between the interlayer sheets.

In *melt intercalation* the layered silicate is mixed with the polymer in the molten state. If the polymer and layered surfaces are sufficiently compatible, the polymer can enter into the interlayer surfaces and form either an intercalated or an exfoliated nanocomposite.

1.5 Types of Nanocomposite

Depending on the nature of the components used (layered silicate, organic cation and polymer matrix) and the method of preparation, three main types of composites can be formed.

Phase-separated composite: When the interaction between the polymer and the layered silicate is very less, the polymer will not be able to intercalate between the silicate layers, a phase-separated composite is obtained, which is similar to a micro composite.

Intercalated nanocomposite: Here one or more than one extended chains of the polymer is intercalated between the silicate layers resulting in a well ordered morphology with alternating layers of polymer and clay. Here the repetitive multilayer structure is preserved.

Exfoliated nanocomposite: When the silicate layers are completely and uniformly dispersed in a continuous polymer matrix, exfoliated or delaminated structure is obtained. When the distributed clay layer has a definite orientation it is called as *ordered exfoliated structure*, whereas randomly distributed structure is called as *disordered exfoliated structure*.

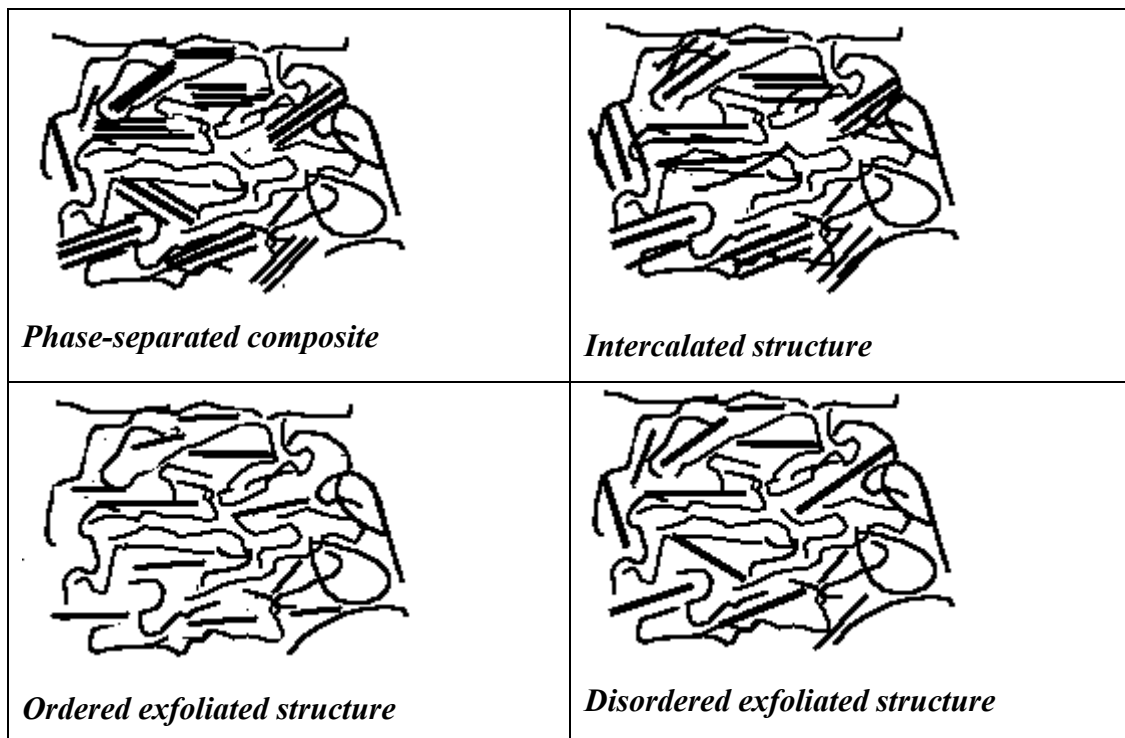


Figure 1.5.1: Types of Nanocomposites

1.6 Literature Search

1.6.1 Types of Polymers used in Preparation of Nanocomposite

Various polymers are used to synthesize polymer layered silicate nanocomposites. An overview of the different methods of preparation and properties of various polymer nanocomposites will be given in this section.

Vinyl addition polymers derived from common monomers such as methacrylate⁽¹⁰⁻²⁰⁾, ethyl methacrylate⁽²¹⁾, acrylic acid⁽²²⁾, acrylonitrile⁽²³⁾, styrene⁽²⁴⁻⁶⁵⁾, acrylamide⁽⁶⁶⁾, isopropyl acrylamide^(67, 68) are generally used for preparation of nanocomposites.

Selective polymers like Poly vinyl acetate (PVA)^(69, 70), Poly vinyl Pyrrolidone (PVP)⁽⁷¹⁻⁷³⁾, Poly ethylene glycol (PEG)⁽⁷⁴⁾, Polyvinyl Carbazole⁽⁷⁵⁾, Poly vinyl Chloride (PVC)⁽⁷⁶⁾, Polybenzoxazole⁽⁷⁷⁾, Polystyrene-isoprene diblock copolymer^(78, 79) have also been studied.

Technologically important step condensation polymer nanocomposites such as Nylon 6 and other polyamides⁽⁸⁰⁻¹¹⁶⁾, Poly (ϵ -caprolactone)⁽¹¹⁷⁻¹²¹⁾, Polyethylene terephthalate (PET)⁽¹²²⁻¹²⁴⁾, Poly (trimethylene terephthalate)⁽¹²⁵⁾, Polybutylene terephthalate (PBT)⁽¹²⁶⁻¹²⁸⁾, other polyesters⁽¹²⁹⁻¹³⁴⁾, Poly carbonate (PC)⁽¹³⁵⁻¹³⁷⁾, Poly ethylene oxide (PEO)⁽¹³⁸⁻¹⁴⁷⁾, Polyethyleneimine⁽¹⁴⁸⁾, Poly Dimethyl Siloxane⁽¹⁴⁹⁾, Polybutadiene, Epoxy polymer resins⁽¹⁵⁰⁻¹⁶⁵⁾, Polyurethanes (PU)⁽¹⁶⁶⁻¹⁷²⁾, Poly urethane urea⁽¹⁷³⁾, Polyimides (PI)⁽¹⁷⁴⁻¹⁹⁴⁾, Polyetherimide⁽¹⁹⁵⁾ and Polysulfone⁽¹⁹⁶⁾, Polyolefins such as Polypropylene (PP)⁽¹⁹⁷⁻²⁴³⁾, Polyethylene (PE)⁽²⁴⁴⁻²⁵¹⁾, Poly(1-butene) (PB)^(252,253), Poly (4-methyl 1-pentene) (PMP)⁽²⁵⁴⁾, Polyethylene co vinyl acetate⁽²⁵⁵⁻²⁵⁸⁾ and EPDM rubber⁽²⁵⁹⁾ are also widely used in the preparation of the nanocomposites.

Nanocomposites of specialty polymers like Poly (n-vinyl carbazole)⁽²⁶⁰⁾, Polypyrrole, Poly aniline⁽²⁶¹⁻²⁷⁰⁾ and biodegradable polymers like Poly (L-Lactide)⁽²⁷¹⁾, Poly (butylene succinate) (PBS)⁽²⁷²⁾, Polycaprolactone, and Poly lactic acid⁽²⁷³⁾ have also been widely reported.

Recently there are some reports on liquid crystalline polymers^(274, 275), other polymers such as Polyisoprene⁽²⁷⁶⁾, Epoxidised Natural rubber⁽²⁷⁷⁾, Rubber⁽²⁷⁸⁻²⁸⁰⁾,

Poly (biphenyl ether triphenyl phosphate)⁽²⁸¹⁾, Poly oxymethylene⁽²⁸²⁾, Polysiloxane⁽²⁸³⁾ and polymer blends based nanocomposites⁽²⁸⁴⁻²⁸⁶⁾.

Out of these, nanocomposites of most of the commercially important polymers like PS, Nylon, PE, PP, PCL, PBT, PC etc can be prepared by melt blending as well as other methods such as in-situ and solution polymerization. However, non-polar polymers such as PP, PE etc require additional compatibilization. The backbone of the compatibilizer is typically miscible with the polymer matrix and the polar group of the compatibilizer interacts with silicates. Polyethylene grafted with maleic anhydride (PE-g-MA) and polypropylene grafted with maleic anhydride (PP-g-MA) respectively, are widely used for making PE and PP nanocomposites by melt intercalation.

1.6.2 Thermodynamics of Intercalation Process

The physical mixture of polymer and clay may not form a nanocomposite. It is similar to a normal composite which might form a phase-separated system. Such phase separated or immiscible system leads to poor interaction between the organic and inorganic components, namely, the polymer and clay. Strong interaction between the polymer and the layered clay leads to the dispersion of the polymer and the clay to the nanometer layer. Hence, they exhibit unique properties not exhibited by conventional composites.

Pristine layered silicates usually contain hydrated Na^+ and K^+ ions. These layered silicates are miscible with only hydrophilic polymers such Polyvinyl Alcohol (PVA) or Polyethylene oxide (PEO). Intercalation of the polymer into the clay layers is governed by the thermodynamics^(287, 288).

In order to render layered silicates miscible with other polymer matrices the normally hydrophilic silicate is converted to an organophilic one. This is done by ion-exchange reactions with cationic surfactants including primary, secondary, tertiary, and quaternary alkyl ammonium or alkyl phosphonium cations. Alkyl ammonium or alkyl phosphonium cations in the organosilicates lower the surface energy of the inorganic host and improve the wetting characteristics of the polymer matrix, and result in a larger interlayer spacing. Additionally, the alkyl ammonium or alkyl phosphonium cations can provide functional groups that can react with the

polymer matrix, or in some cases initiate the polymerization of monomers to improve the strength of the interface between the inorganic and the polymer matrix (289-292).

Depending on the packing density, temperature and alkyl chain length, the chains were thought to lay either parallel to the silicate layers forming mono or bilayers, or radiate away from the silicate layers forming mono or bimolecular arrangements. However, these idealized structures have been shown to be unrealistic by Vaia et al (293) using FTIR experiments. They showed that structure of alkyl chains could vary from liquid-like to solid-like, with the liquid like structure dominating, as the interlayer density or chain length decreases, or as the temperature increases. In addition, for longer chain length surfactants, the surfactants in the layered silicate can show thermal transition similar to melting or liquid-crystalline to liquid-like transitions upon heating (293).

1.6.3 Theoretical Models

Vaia et al, have used mean field, lattice based model for polymer melt intercalation in organic layered silicate. In general, interplay of entropic and energetic factors determines the outcome of polymer intercalation. The model indicates that the entropic penalty of polymer confinement may be compensated by the increased conformational freedom of the tethered chains as the layer separate. When total entropy change is small, changes in the internal energy of system will determine whether the intercalation is thermodynamically stable or not. Complete layer separation depends on establishment of favorable interaction between polymers-organic layered silicate interactions to overcome penalty of polymer confinement (294,295).

The interlayer structure of organic layered silicate should be optimized to maximize configurational freedom of chains upon layer separation and to maximize potential interaction sites at interlayer surface.

Balazs and coworkers (296) have investigated the thermodynamic factors affecting the hybrid formation. They have suggested that the interaction between the polymer and the treated clay surface decides the type of composite formed. If the interaction parameter (χ), between the polymers and surface of the treated clay, is

less than zero and length of polymer chains is large, then the probability of forming an intercalated hybrid is maximum. From thermodynamic point of view, increasing the attractive interaction between the polymer and surfactants promotes formation of exfoliated structures. But the kinetic behaviour of interpenetrating of interpenetrating polymers can hinder formation of exfoliated structures. They have provided design criteria for synthesizing exfoliating agents. The polymer must contain a fragment that is highly attracted to surface and thus promotes the miscibility. In addition it should contain a longer segment that is not attracted to the sheets and will attempt to push layers apart. Once separated, these blocks will sterically hinder the surfaces from coming into closer contact. They have suggested that use of a mixture of functionalized and non-functionalized polymers for the melt can also lead to exfoliated morphologies⁽²⁹⁷⁾. Miscibility can also be enhanced between organically modified clay and polymers with higher number of branches, due to the compactness of the macromolecules⁽²⁹⁸⁾. They have also shown a bare surface and a surface with too many tethered surfactants are both unfavourable for forming hybrids. This also suggests that there is an optimal grafting density, which depends on the specific value of χ between the polymer and surfactant⁽²⁹⁹⁾.

1.6.4 Characterization Techniques

1.6.4.1 X-ray Diffraction

The structure of a polymer layered silicate nanocomposites has been traditionally investigated using X-ray diffraction (XRD) and transmission electron microscopy (TEM).

Wide angle X-ray Diffraction (WAXD) is a powerful technique to monitor the formation and evolution of intercalated hybrids, because of the lamellar structure of the ordered intercalates with a periodicity of 1-4 nm. The finite layer expansion in the case of intercalated nanocomposites leads to the emergence of a new set of basal planes, which can be identified. Study of the relative position, shape and intensity of the basal reflections can identify the nanocomposite structure. The exfoliated nanocomposites as well as disordered nanocomposites are XRD silent due to the absence of ordered structure, which can diffract the X-rays. The extensive

delamination of clay, results in the absence of coherent scattering, in the case of exfoliated nanocomposites. XRD cannot provide definitive information in such type of nanocomposites⁽³⁰⁰⁾.

Vaia and Lu⁽³⁰¹⁾ have shown that XRD can also be used as a tool to find the layer correlation such as crystallite size and disorder. It is also reported that kinetics of intercalation can be studied using in-situ XRD⁽³⁰²⁾.

Small angle X-ray scattering is also used as a technique to analyze Polymer Layered Silicate nanocomposites. Bafna et al have used 2 dimensional simultaneous SAXS and WAXS measurements to determine the 3 dimensional orientations of the polymer and clay in the polymer nanocomposites.⁽³⁰³⁾

1.6.4.2 Transmission Electron Microscopy (TEM)

TEM is an extremely useful technique, especially in the *XRD silent* nanocomposites. It gives a direct evidence of the structure and a definitive description of the spatial correlation such as distribution and inhomogenities of the nanocomposites. XRD and TEM are complementary techniques in the evaluation of nanocomposites⁽³⁰⁴⁾.

1.6.4.3 Nuclear Magnetic Resonance (NMR)

Vandelhardt et al. studied the application of ¹³C NMR in order to study the dispersion of clay platelets. In naturally occurring montmorillonite, surfaces of the layers are mainly made of silica tetrahedral while the central plane of the layers contains octahedrally coordinated Al³⁺ with frequent nonstoichiometric substitutions where an Al³⁺ is replaced by Mg²⁺ and somewhat frequently by Fe³⁺. The concentration of the former produces embedded negative charge in the clay layers and is neutralized by Na⁺ or an organic modifier. Fe³⁺ is strongly paramagnetic. Typical concentrations of Fe³⁺ in naturally occurring Montmorillonite clays produce nearest-neighbor Fe-Fe distance of about 1.0-1.4 nm and at such distances, the spin exchange interaction between the unpaired electrons on different Fe atoms is expected to produce magnetic fluctuations in the vicinity of the Larmor frequencies for protons or ¹³C nuclei⁽³⁰⁵⁾. The spectral density of these fluctuations is important because the longitudinal relaxation, T₁^H, of protons (and ¹³C nuclei) within about 1nm of the clay surface can be directly shortened. For protons⁽³⁰⁶⁾, if that mechanism

is efficient, relaxation will also propagate into the bulk of the polymer by spin diffusion⁽³⁰⁷⁾. Thus, this paramagnetically induced relaxation will influence the overall longitudinal relaxation measured to T_1^H to an extent that will depend both on Fe^{3+} concentration in the clay layer and, more importantly, on the average distance between the clay layers. The layer dependence suggests a potential relationship between measured T_1^H values and the quality of the clay dispersion. The poorer the clay dispersion, the greater is the average distance between polymer/clay interfaces and the weaker is the paramagnetic contribution to T_1^H . Hence, the measurement of T_1^H can be used to calculate the clay dispersion^(308, 309).

1.6.4.4 Morphology

1.6.4.4.1 Crystallinity, Crystallization, and Polymorphism

The process of crystallization can control the intercalation and morphology and hence control the mechanical properties, barrier properties etc., of the nanocomposites.

Maiti et al⁽²²⁸⁾ has studied the effect of crystallization on the structure and properties of the nanocomposites. It was observed that the extent of intercalation of maleic anhydride modified PP in the space between silicate galleries increased with crystallization temperature (T_c) and decreased as clay content increased. The clay particles act as nucleating agent, and lower the spherulitic dimension with increasing clay content as was observed by optical microscopy. Extensive intercalation occurred during crystallization, especially at high T_c due to long time for full solidification of melt. The degree of intercalation was governed by the time in the molten state. Zhang et al⁽²⁰³⁾ observed that the clay inhibits the formation of β -phase crystallites, speed up the crystallization rate of α phase, and slightly promotes the formation of γ phase crystallites in the nanocomposites. Similar enhancement in crystallization of α phase PP was observed and PP crystallized at much higher temperature in fibrillar form, which increased in diameter as time increases⁽²²⁹⁾.

Murase et al,⁽⁹⁸⁾ showed that the Nylon 6 changes from α phase in pristine polymer to γ phase in the nanocomposite with mica, whereas, it forms a mixture of α and γ phases in the nanocomposite with natural montmorillonite. Ke et al⁽¹²³⁾ have

shown that PET/clay nanocomposites have a higher crystallization rate due to exfoliated clay acting as nucleating agent. In the case of PEO/Na⁺ Montmorillonite clay nanocomposite, reduction in spherulite size and an increase in the rate of crystallization are observed⁽¹⁴⁷⁾.

1.6.4.4.2 Optical Properties

Polymer nanoclay composites can potentially form optically clear films under certain conditions. This is possible in the case of exfoliated composites where the clay platelets are oriented with their surface normal, parallel to the direction of incident light. Under this condition, the nanocomposites will not scatter light, because the thickness of the platelets is less than the wavelength of the visible radiation. The translucent nature of the nanocomposites in in-situ polymerized methyl methacrylate (MMA)/*n*-dodecylmethacrylate (LMA) copolymers nanocomposites, were observed by Dietsche et al⁽³¹⁰⁾.

1.6.5 Properties of Nanocomposites

Generally polymer nanocomposites exhibit significantly higher modulus, thermal stability and barrier properties without much change in the density. These property improvements are effective even at 5-wt% loading, which is very less as compared to micro composites.

1.6.5.1 Thermal Properties

1.6.5.1.1 Melting Point

Chang and coworkers have observed an increase in the melting point of thermotropic liquid crystalline polyester (TLCP) nanocomposites. This has been ascribed to the heat insulation effect of the clay layered structure, as well as strong interaction between organoclay and TLCP molecular chains⁽²⁷⁴⁾. In the case of polyester nanocomposite annealed at high temperature, Phang et al⁽³¹¹⁾ observed an unusually high temperature melting point peak. The origin of this peak was supposed to be due to the constrained polymer chains.

1.6.5.1.2 Thermal Stability and Degradation

The thermal stability of polymers is studied by thermo gravimetric analysis (TGA). The weight loss due to formation of volatile products is studied as a function

of time. In the presence of inert gas, a non-oxidative degradation occurs, whereas, in presence of oxygen or air, oxidative degradation occurs. Zhang et al ⁽¹⁹⁸⁾, in the case of PP nanocomposite have observed a 130 °C increase in the onset of degradation as compared to pure PP. This enhancement is explained by them as caused due to decreased oxygen permeability and barrier labyrinth effect of the intercalated or exfoliated clay in the composites on the diffusion of degradation products from bulk of the polymer to the gas phase. Blumstein ⁽³¹²⁾ has also reported the improved thermal stability of PMMA/Clay nanocomposites. Gilman ⁽³¹³⁾ has written a detailed review on the thermal stability of polymer/clay nanocomposites.

1.6.5.1.3 Coefficient of Thermal Expansion (CTE)

Agag et al ⁽¹⁸²⁾, while studying the polyimide nanocomposites observed that the CTE decreased from 7.35 $\mu\text{m}/\text{m } ^\circ\text{C}$ to 6.39 $\mu\text{m}/\text{m } ^\circ\text{C}$ (1% clay) and 5.40 $\mu\text{m}/\text{m } ^\circ\text{C}$ (2% clay). The CTE was observed to increase with increase of clay above 4%. Yoon et al ⁽¹⁰⁶⁾, have studied the Thermal expansion coefficients of Nylon 6 nanocomposites. They have also observed a reduction in the coefficient of thermal expansion in all the three directions namely, flow direction, transverse direction and normal direction.

1.6.5.1.4 Heat Distortion Temperature (HDT)

Heat distortion temperature, as measured by ASTM D 648 (ISO 75) test procedures, is defined as temperature at which an applied load causes a test bar to deflect by 0.25 mm. Kojima et al ⁽⁸²⁾ demonstrated that in the case of Nylon 6 the HDT increases from 87 °C to 152 °C. The HDT was found to increase with clay percentage up to 4.5% and further it levels off. Shelley et al have calculated the HDT of Nylon 6 nanocomposites from the dynamic mechanical analysis as the temperature at which the storage modulus reduces to 1/4th its value at room temperature ⁽⁹⁰⁾. This increase in HDT is a result of better reinforcement of the clay particles, intercalation, and crystallinity.

1.6.5.2 Mechanical Properties

1.6.5.2.1 Modulus and Strength

Toyota researchers reported dramatic improvement in modulus of exfoliated polyamide 6-nanocomposites. The modulus increased by 90 % with addition of 4 % of exfoliated clay. They also showed that the extent of improvement in modulus was related to the length of silicate layers, ionic bonding strength of clay with polymer and the orientation of the polymer and clay ⁽⁸²⁾. Shelley and coworkers ⁽⁹⁰⁾ have attributed the increase in the modulus to constrained volume of polymer in the clay. Fornes et al ⁽⁹⁵⁾ have analyzed effect of molecular weights on the mechanical properties. It was observed that the high molecular weight based nanocomposites have the highest moduli, yield strength and elongation at break. Moreover, the Izod impact strength was also found to increase. Lan and Pinnavia ⁽¹⁵³⁾ have reported a 10-fold increase in the modulus in a rubbery epoxy matrix on addition of 15-weight % (7.5 volume %) clay. In the study of Polyurethane by Wang and Pinnavia, the modulus, strength, and strain at break all increased by more than 100%. The enhancement in strength and modulus were attributed to the reinforcement provided by the dispersed silicate nanolayers. They attributed the improved elasticity to the plasticizing effect of gallery onium ions, which contribute to dangling chain formation in the matrix ⁽¹⁶⁶⁾. Zhang and coworkers have observed that the mechanical strength of PP does not improve much after the formation of nanocomposite but impact strength increases at lower clay content ⁽¹⁹³⁾. Manias and coworkers ⁽²¹⁷⁾ observed a sharp increase in the modulus for lower content of clay followed by a much slower increase beyond 5%. With increasing clay content, the yield stress remained constant as compared to pristine polymer and there is only a small decrease in the strain at break for PP nanocomposites.

1.6.5.2.2 Creep Studies

The creep behaviour of polymer-layered silicate nanocomposites has not been extensively reported. Lee et al, have studied the viscoelastic properties of epoxy-clay and hybrid inorganic-organic epoxy nanocomposites using small-strain stress relaxation experiments. Main conclusion of these experiments was that both types of

reinforcement provided some enhancement in creep resistance because characteristic relaxation time increased with the addition of reinforcement ⁽³¹⁴⁾. It has been observed in epoxy nanocomposites that creep resistance of nanocomposite increased with true silicate content. As applied stress is sufficiently close to yield point of epoxy, the creep data collapses to single curve, at this stress, matrix yielding becomes dominant mechanism and the nanocomposite structure does not influence creep mechanism ⁽³¹⁵⁾.

1.6.5.3 Dynamic Mechanical Properties - Storage Modulus and $\tan \delta$

Dynamic mechanical analysis (DMA) measures the response of a given material to a cyclic deformation as function of temperature and frequency. DMA results are expressed by three parameters, the storage modulus (E'), loss modulus (E''), and $\tan \delta$. E' corresponds to energy stored elastically and reversibly; the E'' corresponds to the energy transformed into heat and irreversibly lost and the $\tan \delta$ is the ratio of E'' to E' . $\tan \delta$ is useful in determining the occurrence of molecular mobility transitions such as the glass transition.

It is generally observed that the addition of organic layered silicates increases the storage modulus of the nanocomposites. In insitu polymerized PMMA nanocomposites rubbery modulus was observed to be 30 times that of the pristine polymer for 5% of clay ⁽¹⁷⁾. In most of the cases, it is also observed that the storage modulus increases monotonically with the clay content. However, in the case of PMMA nanocomposite prepared by solution intercalation, Zilg et al have observed a reduction in the modulus after 4-weight % synthetic fluorohectorite loading ⁽³¹⁶⁾.

In the case of PU nanocomposites ⁽¹⁷¹⁾ studied by Yao et al, increase in G' below T_g is about 350% where as not much improvement is observed above T_g .

Tyan et al ⁽¹⁸⁵⁾ first observed an increase in T_g in the case of Polyimides. Giannelis and coworkers observed an increase in T_g as well as broadening of peak as measured by DMA in epoxy nanocomposites, which they have attributed to the hindered relaxational mobility in polymer segments near the surface ⁽¹⁵⁰⁾. Similar increase in T_g is observed in nanocomposites of PCL ⁽¹¹⁹⁾, PU ⁽¹⁷¹⁾, PI ^(178, 182, 184, 185), PMMA ^(13, 16, 17), PS ⁽⁵⁴⁾, PP ^(198, 205, 208, 210, 229, 232) and PVC ⁽⁷⁶⁾. This increase in T_g

has been ascribed by most of them to the restriction in segmental motion^(171, 198, 205). Zhang et al⁽¹⁹⁸⁾ has ascribed the T_g increase in PP nanocomposites to the plasticizing effect of MAH grafted PP due to the decrease in geometric constraints altering chain conformation. In the case of solution polymerized PMMA⁽¹³⁾, a 20 °C increase in T_g is observed. The rate of increase in T_g decreases with the clay content. This effect was supposed to be due to branching. In the case of Nylon 6⁽⁹⁰⁾ nanocomposites a decrease in the T_g which has been observed and was ascribed to the restriction of carbonyl segmental mobility with increasing clay content. This restriction in motion was expected due to the constraint in the mid-chain amide groups by the clay surfaces as well as the amine end groups.

1.6.5.4 Melt Rheology

Rheology provides information about the processibility of the material and relates to the microstructure. Rheology can be used as a characteristic technique to complement TEM and XRD as it relates to the microstructure. There is a lot of work being done on rheology of nanocomposites of polymers like polystyrene-isoprene diblock copolymer, Polycaprolactone, Polyamide, Polystyrene, Polydimethylsiloxane, and Polypropylene. There are two regions of study: (i) linear region where stress is proportional to strain and (ii) non-linear region where stress and strain relations are not in the linear regime.

1.6.5.4.1 Linear rheological properties

The important observations in most of the reports are the pseudo-solid like behaviour at low frequencies. Ren et al have attributed the pseudo-solid like behaviour observed in the nanocomposites to the physical jamming of the dispersed clay layered silicates formed due to the highly anisotropic nature⁽¹⁵⁸⁾. The pseudo-solid like behaviour corresponds to a change in viscoelastic behaviour from liquid like for unfilled polymer (i.e., $G' \propto \omega^2$ and $G'' \propto \omega^1$) to solid-like for nanocomposites (i.e., G' and $G'' \propto \omega^0$).

Time temperature superposition used to prepare viscoelastic master curve and frequency shift factors is comparable to that for the unfilled polymer. The shift factors and consequently the flow activation energy being unaffected by the amount

of added layered silicate have been understood in terms of the lack of temperature dependant relaxation associated with the layered silicate or aggregate of layered silicates⁽³¹⁷⁾. In addition to this Krishnamoorthy and Giannelis⁽³¹⁸⁾ observed that at low shear rates viscosity increases monotonically with clay content for Polydimethyl siloxane (PDMS)⁽³¹⁹⁾. The nanocomposites of PDMS in show a shear thinning behaviour and low frequency plateau in the modulus⁽³¹⁹⁾.

Creep measurements were carried out by Galgali et al⁽³²⁰⁾, to confirm the origin of solid-like behaviour. A dramatic increase in the creep compliance of the nanocomposites prepared with compatibilized PP and 6% Montmorillonite was observed. Furthermore, for nanocomposite of compatibilized PP and 9 % by weight of montmorillonite, they have shown a three-order of magnitude drop in the zero-shear viscosity beyond the apparent yield stress, suggesting that the solid-like character in the quiescent state is a result of the percolated structure of the layered silicates.

Lee and Han⁽³²¹⁾ have studied the effect of hydrogen bonding between the layered silicate and polymer using Polystyrene block hydroxylated polyisoprene (SIOH) and Polystyrene block polyisoprene (SI). The hydrogen bonding between the layered silicate and SIOH was confirmed using FTIR. It was shown that the hydrogen bonding has dramatic effects on the rheology of polymer-layered silicates. In SIOH, it was observed that the G^* and η^* increases with temperature and in SI G^* and η^* decreases with increasing temperature.

Hoffmann and coworkers⁽³²²⁾ have studied the effect of types of modifiers used for fluoromica on the rheological property of PS/fluoromica nanocomposites. Intercalated structure was observed when 2-phenylethylamine (PEA) ($M_n=121$ g/mol) was used as modifier while for amine terminated polystyrene (AT-PS8) ($\overline{M}_n = 5800$ g/mol) an exfoliated structure was observed. It is reported that the time temperature superposition holds for pristine PS as well as for both nanocomposites. The plots of G' vs. the reduced frequency (ωa_T) showed slightly higher values of G' for intercalated nanocomposites prepared using PEA treated fluoromica, while G' for exfoliated nanocomposite prepared using amine terminated Polystyrene showed

significant increase in G' . This increase in G' at low frequencies was attributed to the network formation involving assembly of platelets.

1.6.5.4.2 Nonlinear Rheological Properties

The strain amplitude sensitivity of PP and Polystyrene-isoprene diblock co polymers were studied. It was observed that G' and G'' begin to decrease at strain amplitudes significantly smaller than those of pristine polymers. Strain amplitude defining the onset of softening decreased with increasing silicate loading. At large amplitude oscillatory shears, the layered silicate get oriented to the applied field and results in the preferential orientation of the silicate layers and liquid like linear viscoelastic response is observed ^(58,242, 317, 321, 323). Krishnamoorti et al ⁽³²⁴⁾ observed that the viscosity of hybrids is comparable to that of the matrix viscosity in Polystyrene isoprene nanocomposites, suggesting that the shear flow aligns the clay tactoids.

1.6.5.5 Electrical Properties

Dielectric spectroscopy can provide information about the segmental mobility of a polymer by probing its dielectric properties. The complex dielectric properties namely, the relative permittivity (ϵ') and the loss factor (ϵ'') can be obtained as function of frequency at fixed temperature or can be obtained as a function of temperature at fixed frequency. An alternating current external electric field is applied across the sample in a capacitor plate configuration. The polarization is related to applied electric field and it consists of four different dielectric mechanisms (electronic, atomic, orientation or dipolar and ionic polarization). Kanapitsas and coworkers ⁽³²⁵⁾ have studied the Epoxy resin-smectite clay exfoliated nanocomposites and observed that in the whole range of measured frequency ϵ' decreases. This was attributed to the mobility decrease in the nanocomposite as compared to the pristine polymer matrix. Two loss peaks are observed in the nanocomposite at about 10 Hz and $10^3 - 10^4$ Hz at 30 °C both of them shifting to higher frequencies with increasing temperature. As peaks were absent in the pure matrix, they were ascribed to the effects related with the presence of clay, probably

to interfacial polarization effects. Chang and Wang have also found a similar effect in Polystyrene/clay nanocomposites⁽³²⁶⁾.

Williams and coworkers⁽³²⁷⁾ have shown that in phenolic resin/organic treated clay nanocomposite the ionic conductivity of the nanocomposite increases with both temperature and frequency and is higher than that of the pristine polymer by two to three orders of magnitude. The nano-sized inclusion governs the transport phenomenon, facilitating ion transfer through the inter-regions and intra-regions of the silicate galleries.

1.6.5.6 Flammability and fire retardant property

Cone calorimetry (ASTM E1354) is one of the most effective bench scale method for studying the flammability property of the materials. The cone calorimeter measures fire-relevant properties such as heat release rate (HRR), carbon monoxide production and smoke production among others. HRR has been found to be the most important parameter to evaluate fire safety.

Gilman and coworkers^(328, 329, 330) have studied the fire retardation properties of polymer nanocomposites of Nylon 6, Nylon 12, Polystyrene, PP etc. They have observed that the type of layered silicate, level of dispersion, and processing have an influence on the magnitude of flammability reduction. They have observed that the Montmorillonite must be nanodispersed for it to affect the flammability. They have suggested that the general nanocomposite flame retardant mechanism is that high performance carbonaceous silicate char builds up on the surface during burning and this insulates the underlying material and slows down the mass loss rate of decomposition products.

However, Dietsche and Mulhaupt⁽³³¹⁾ and Zanetti et al⁽⁴³⁾ have observed a maximum heat release rate in acrylic and PS based nanocomposites, respectively.

1.6.5.7 Barrier Properties

The incorporation of clay in the polymer like polyimide has been observed to increase the barrier properties by creating a maze or tortuous path that retards the progress of gas molecules through the matrix resin⁽¹⁹⁰⁾. Small fractions of clay, exhibited reduction in the permeability of small gases like O₂, H₂O, He, CO₂, and ethylacetate vapours.

1.7 Polyvinylidene Fluoride

Polyvinylidene fluoride, abbreviated as PVDF or PVF₂, is a semi-crystalline polymer with outstanding electrical properties, chemical and weather resistance, durability and biocompatibility. It has many applications in the field of transducers and actuators because of its high elasticity, processability, and electrical properties. It has four known polymorphs, called as α , β , γ and δ .

1.7.1 Chemistry

PVDF is made by radical polymerization in emulsion or suspension of the gaseous monomer 1,1-difluoroethylene ($\text{CH}_2 = \text{CF}_2$). The reaction is preferentially performed in water at elevated temperature (up to 150 °C) and pressure [(1-100) MPa] with organic peroxides (e.g., benzoyl peroxide or diisopropyl peroxydicarbonate) as catalysts. Isopropyl alcohol can serve as chain transfer agent. The monomer, for this part, is synthesized by pyrolysis of CF_3CH_3 , CF_2ClCH_3 , or similar compounds. The degree of polymerization of industrial products usually amounts to 1500, resulting in $\overline{M}_w = 100000$ and $\overline{M}_n = 500000$. NMR measurements reveal that polymerization processes yield between 2 % and 7 % of head-to-head and tail-to-tail links ($-\text{CF}_2-\text{CF}_2-$, $-\text{CH}_2-\text{CH}_2-$), respectively⁽³³²⁾.

1.7.2 Phases, Preparation routes, Crystallization and Crystal Structure

PVDF exhibits four crystalline polymorphs, namely, α , β , γ and δ phases (or II, I, III, and IV, respectively).

α phase is the most commonly obtained phase and is generally obtained from melt. The chain conformation of this phase is trans-gauche-trans-minus gauche (tgtg') with $t=179^\circ$ and $g=45^\circ$ and anti parallel dipole moment. The unit cell consists of two monomeric units, forming an orthorhombic unit cell with lattice parameters, $a=0.496$ nm, $b=0.964$ nm and $c=0.462$ nm^(333, 334, 335, 338).

The α phase can be obtained by solution crystallization of xylene/acetone mixture, monochloro benzene (MCB) and Dimethyl Formamide (DMF)⁽³³⁷⁾.

β phase PVDF is widely used in pyro and piezoelectric applications. This is generally obtained by drawing PVDF α phase films at temperature 70-87 °C⁽³³⁸⁾.

The α to β conversion varies as a function of temperature and maximum conversion is obtained at 87 °C⁽³³⁹⁾. This phase is also obtained by solution casting from Dimethyl Formamide (DMF) and Dimethyl Acetamide (DMAc) below 70 °C⁽³⁴⁰⁾. Heat treatment and application of high pressure also leads to the formation of this phase⁽³⁴¹⁾.

The unit cell of β phase of PVDF is orthorhombic and consists of two polymer chains with cell constants, $a=0.858$ nm, $b=0.491$ nm and $c=0.256$ nm^(333, 347). The polymer chains possess a slightly deflected all trans conformation and parallel dipole moment.

Recently there are several reports on formation/increment of β phase, by addition of fillers such as $MgCl_2$ ⁽³⁴²⁾, $AgNO_3$ ⁽³⁴³⁾ and milling of originally α phase powder⁽³⁴⁴⁾.

γ phase is obtained by high temperature melt crystallization ($T>160$ °C). This phase is also obtained by solution crystallization in DMF, DMA, and Dimethyl Sulphoxide (DMSO).

Lovinger suggested a monoclinic structure for this phase with cell constants, $a=0.496$ nm, $b=0.967$ nm and $c=0.920$ nm and $\beta=93$ °^(339, 348). γ phase has a chain conformation of $t_3g^+ t_3g^-$ with parallel dipole moments^(345, 346, 347, 348).

Prest and Luca⁽³⁵⁰⁾ have observed annealing induced phase transformation from α to γ at 158 °C. They have also reported that β to γ phase transformation can be obtained by slow melting and recrystallization. Certain surfactants were also used to modify the melting of α and β phases and to promote γ phase⁽³⁴⁹⁾. The γ phase is also obtained by annealing α phase films at 185.8 °C and atmospheric pressure⁽³⁵⁰⁾. It has been observed that the application of electric field favored the formation of γ phase and reduced the minimum temperature required for γ formation⁽³⁵²⁾. The crystallization of γ phase was observed at 100 °C, 120 °C and even at 145 °C in presence of an electric field of 0.07 MV/cm^(351, 352). Lovinger obtained α to γ transition by melt crystallizing under high or rapid extension at low temperatures⁽³⁵³⁾.

δ phase is obtained by polarization of α phase under high electric field, approximately 1.25 MV/cm at room temperature. The unit cell and molecular conformation are similar to that of the α phase. Dipole moment is parallel ^(354, 355, 356).

ϵ phase is obtained by annealing of δ phase. This phase is an anti polar analogue of γ phase ⁽³⁵⁶⁾.

1.7.3 XRD peaks for various phases of PVDF

The XRD peaks of the various crystalline phases of PVDF ⁽³⁴⁵⁾ are summarized in the table 1.7.1.

Table 1.7.1: XRD peaks of the different phases of PVDF

Crystalline Phase	Crystal planes	Peak position in $2\theta^\circ$ with Cu K_α
α	(100)	17.7
	(020)	18.4
	(021)	19.9
	(111)	27.8
	(200)	35.7
	(002)	39
	(022)	57.4
β	(110)	20.8
	(200)	20.7
	(020)	36.6
	(101)	36.6
	(221)	56.1
γ	(020)	18.5
	(002)	19.
	(110)	20.1
	(101)	20.3
	(022)	26.8
	(200)	36.2
	(211)	38.7

1.7.4 IR Vibration modes

The IR absorption bands of the different crystalline phases, their assignments, and their corresponding references are summarized in the table 1.7.2.

Table 1.7.2: IR vibration modes and their assignments

Crystalline Phase	IR Absorption band wave number (cm ⁻¹)	Assignment	References
α	490	CF ₂ bending and waging	356
	530	CF ₂ bending	
	618	CF ₂ bending and skeletal bending of C(F)-C (H)-C(F)	
	765	CF ₂ bending and skeletal bending of C(F)-C(H)-C(F)	
	796	CH ₂ rocking	
	976	CH ₂ bending mode	
β	445	CF ₂ bending	357
	510	Bending and wagging modes of CF ₂	
	600	CF ₂ bending and C(F)-C (H)-C(F) skeletal vibration	
	745	In plane bending or rocking of CH ₂ , CF ₂	
	840	CH ₂ , CF ₂ rocking and asymmetric stretching	
γ	510	C(F)-C (H)-C(F) skeletal bending	342, 358
	778	H out of plane bending	
	815	C-C stretching	
	950	Twisting of CH ₂	

1.7.5 Morphology

PVDF crystallizes on cooling from the melt in spherulitic morphology. The spherulites have a diameter of the order of few micrometers and have twisted lamellae; the actual size of the spherulites depends on the crystallization condition. The β modification produces lamellar morphology with lamellae perpendicular and chains parallel to the drawing direction⁽³³¹⁾. The α PVDF shows tightly banded ringed spherulites, where as γ phase shows non-ringed spherulites. The reason why the α spherulites are ringed and γ spherulites are non-ringed is still unknown^(359, 360). However, the spherulites are not ringed in case of α PVDF, when the crystallization occurs at temperatures of 130 °C and lesser⁽³³³⁾.

1.7.6 Thermal Properties

PVDF retains its thermal stability up to 470 °C beyond which it degrades with pronounced loss of mass, nearly 60 %. The degradation is due to the emission of hydrogen fluoride along with a small amount of $C_4H_3F_3$. Above 600 °C a residual mass closer to 20 % is observed corresponding to the cross-linked material^(361, 362).

The glass transition temperature is found to be about -60 °C from DSC experiments⁽³³²⁾.

Prest and Luca observed the melting points of α , β and γ crystals as 172, 178 and 186 °C using polarized optical microscopy⁽³⁶³⁾. The crystallization of α , β and γ crystals depends exclusively on the time and temperature at which the process occurs⁽³⁴⁰⁾.

1.7.7 Crystallinity

The commercial grade PVDF is about 40-50 % crystalline. The heat of fusion of 100 % crystalline PVDF is 25 Cal/g⁽³⁶⁴⁾.

1.7.8 Viscoelastic Properties

Many authors have studied the dynamic mechanical behaviour of α PVDF^(365, 366, 367).

There are four different relaxations observed in PVDF⁽³⁶⁸⁾. The lowest relaxation is around -60 °C (at 1 Hz), called as the γ relaxation, and, is due to restricted chain mobility in amorphous fraction or rotational chain movements in amorphous fraction. β relaxation is observed at around -40 °C and is associated with glass transition temperature (T_g) and hence to the micro Brownian motion in the amorphous zones^(369, 370, 371). β' relaxation is observed at 40 °C and is attributed to motion of the folded chains in the crystalline region (T_g')⁽³⁶⁹⁾. The α peak observed at approximately 80 °C is due to liberation of chains in the crystalline phase. This process involves 180° flip motions of the chain stems in the crystalline lamellae. This screw motion process involves both rotational and translational mobility within the chains^(372, 373). A similar higher- T_g relaxation is observed in many semi crystalline polymers including Polyethylene (PE), Poly (methylene oxide), Poly (ethylene oxide) and isotactic polypropylene⁽³⁷⁴⁾. It is reported that the γ relaxation in these polymers merges with the β relaxation.

The relaxation mechanisms are reported to be similar for α and β phases of PVDF⁽³⁷⁴⁾.

1.7.9 Mechanical Properties

The presence of T_g (at approximately -60 °C) and T_g' (at approximately 40 °C) presents, three behavior domains for PVDF. Below T_g , the material is brittle and breaks without whitening. Between T_g and T_g' , PVDF is semi ductile. In this region, the specimen homogeneously whitens; necking occurs at about 40 % elongation and cannot propagate. Ductile fracture occurs within the neck. Above T_g' the behaviour is ductile and necking propagates all along the sample. This is attributed to the nucleation and growth of micro cavities. This is related to the sufficient mobility in the rubbery state of the free amorphous phase⁽³⁷⁵⁾.

Improved mechanical properties of PVDF such as higher modulus are based on the presence of β and γ crystalline phases of PVDF⁽³⁷⁶⁾.

1.7.10 Electrical Properties

The electrical properties of PVDF are due to the strong dipole moment of the chain repeat units and the crystallizability of the polymer. The volume resistivity of PVDF is approximately of the order of $10^{15} \Omega \text{ cm}$.

1.7.11 Dielectric Behavior

The reported value of dielectric constant for α PVDF comes closer to 9 and that of β PVDF is higher of the order of 10-12 at 1 KHz (depending on conditions of preparation). The dielectric relaxations of PVDF are shown in figure 1.7.1.

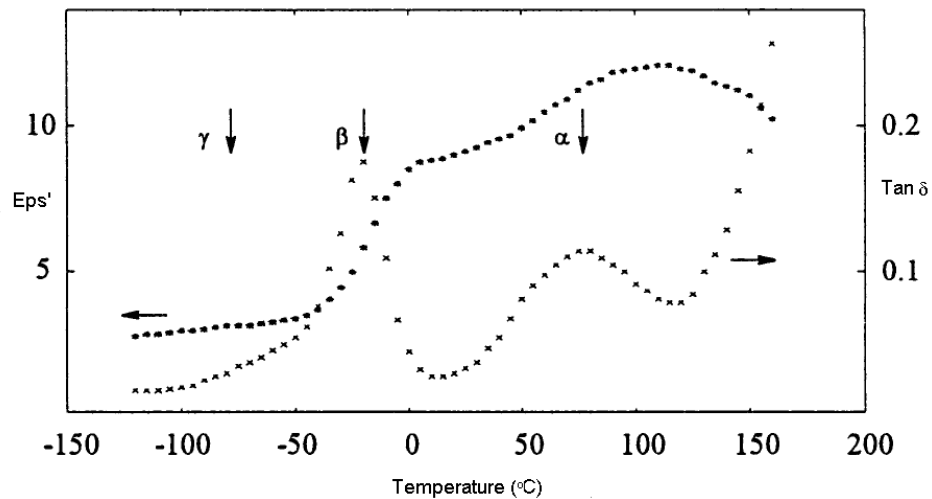


Figure 1.7.1: Dielectric relaxations in PVDF

The β -transition, observed at approximately -40°C , is due to the segmental motions in the liquid like amorphous phase of semi crystalline PVDF and is related to the glass transition dynamics⁽³⁷⁷⁾. PVDF chains contain head-to-head and tail-to-tail defects. Typical PVDF sample contains 4-5 mol % of head-to-head and tail-to-tail defects. The inter phase has crystalline molecular order but no rigid lattice constraints. These chain defects resulting in the significant inter phase region cause the β transition. The higher dielectric constant is also a result of this inter phase. The α -transition observed at approximately 80°C of PVDF is due to the molecular motions within α phase of PVDF.

The β relaxation is because of the segmental motion within the amorphous phase in PVDF. This peak decreases with temperature and shifts towards lower frequency along with a broadening. Near melting point of PVDF, this peak appears at high mega- and low giga hertz region. The molecular origin of this peak is entirely in the amorphous region, which comprises of liquid like amorphous region and the inter phase. The dipolar polarization is a result of cooperative movement of the dipoles in the amorphous phase and amorphous crystalline phase⁽³⁷⁹⁾.

The α peak is associated with relaxation within the crystalline phase. The molecular origin is associated with the imperfections such as the chain loops at lamellar surface, chain rotations and twisting within interior of the crystal, discontinuities etc. As temperature increases the magnitude of the loss peak increases and shifts to higher frequencies. The α peak shifts to higher temperature with increase in frequency^(380, 381). Such relaxations are also observed in polyethylene⁽³⁸²⁾. β -PVDF film shows the low temperature β relaxation due to the glass transition mechanism, but the α transition associated with the molecular motions within the crystalline fraction is not observed. This α relaxation is observed only in the case of α phase PVDF⁽³⁸³⁾.

In the low frequency range ($<10^3$ Hz), the increase in ϵ' and ϵ'' is due to ionic dc conductivity, which results in the interfacial or spatial charge polarization.

β phase is generally obtained by drawing the α phase films. Chain packing and dipole density increases with drawing. However, drawing also restrains the chain mobility, and hence hampers the orientation of dipoles. This process is also related to the decrease in dc conductivity⁽³⁸⁴⁾.

The high dielectric constant and low dielectric loss enables PVDF to act as good insulating materials.

1.7.12 Ferroelectric Properties

α phase PVDF is non-polar in nature. Polar PVDF (β , γ , δ phases) exhibits ferro-electric properties⁽³⁸⁵⁾. The long-range order interaction of dipoles in the ferroelectric phase is extremely strong. Therefore, the Curies temperature (T_C) of 220 °C is higher than the melting point (T_m)⁽³⁸⁶⁾. Action of a sufficiently strong electric

field (poling) causes all electric moments in the polarized crystals to rotate into the field direction, creating a macroscopic, thermodynamically stable polarization below 60 °C⁽³⁸⁶⁾.

1.7.13 Piezoelectricity and pyroelectricity

PVDF is also piezoelectric and pyroelectric in nature. Changes in permanent polarization depend on the application of mechanical pressure and variation in temperature. These properties exist only in polarized phases of PVDF and their strengths are proportional to its remnant polarization. Since it is piezoelectric, it can be used as audio transducers. PVDF is used as electrets in transducer technology^(387, 388, 389).

1.7.14 Other Properties

PVDF is tough, hard, and heat resistant and thermally stable engineering polymer. It is highly weather resistant, and is resistant to most of the chemicals. It is resistant to ultraviolet, β and γ radiation. Under these radiation, it cross-links, accompanied by creation of vinyl bonds and carbonyl groups⁽³⁹⁰⁾. As most of the halogenated polymers, PVDF is non-flammable and self-extinguishing in fire.

1.8 PVDF Composites

PVDF is mixed with various fillers in order to achieve specific property improvements.

The addition of lithium perchlorate salt affects the gelation phase behavior of PVDF in water/DMF solutions. Addition of salt increases the pore size. PVDF crystallized in the β phase in salt containing dopes⁽³⁹¹⁾.

The mechanical properties of PVDF/sized silica hybrid prepared by using sol-gel process are found to be better as compared to the hybrids prepared by mechanical blending of PVDF and fumed silica⁽³⁹²⁾. Crystalline structure of PVDF was not changed much by the addition of SiO₂, indicating that there was no interaction between PVDF and SiO₂. A PVDF/SiO₂ hybrid micro composite film with 5-wt % SiO₂ (approximate particle size 0.5 μ m) exhibited balanced mechanical properties without a severe change in the crystalline structure of PVDF, whereas for the hybrid composites with higher SiO₂ contents (>10 wt %, approximate particle

size 1 μm), the mechanical properties were reduced, and the spherulite texture of PVDF was significantly disrupted⁽³⁹³⁾.

PZT and BaTiO₃ are used in making composite with PVDF in order to get piezo and pyro electric transducers^(394, 395, 396, 397). Composites of electroactive ceramics such as PZT, BaTiO₃ and ferroelectric polymers like PVDF are important for applications since they combine the most important features of both the phases and their properties can be easily tailored to various requirements.

MgCl₂ and AgNO₃ were used as fillers in order to increase α and β phase contents and to increase the one-dimensional electrical conduction. The polarons and bipolarons detected by IR studies were thought to act as hopping sites for a one-dimensional electrical conduction mechanism^(389, 390). In another publication it is reported that addition of MnCl₂ and AgNO₃ in PVDF results in decreases crystallinity of PVDF⁽⁴⁰⁰⁾. The CuCl₂ filled PVDF is found to induce β phase. This system was found to work as an effective microwave modulator due to the induced energy bands created due to the CuCl₂ and the free spin due to electron delocalization⁽⁴⁰¹⁾.

PVDF/Ni micro composites prepared by Dang and coworkers, showed a dielectric constant approximately 400 near the percolation threshold (volume fraction of filler~0.16) and dielectric constant was very weakly dependant on the frequency⁽⁴⁰²⁾.

Del Río et al prepared Carbon black (CB) filled polyvinylidene fluoride (PVDF) composites with electrical conductivity of about 2.4 S/cm⁽⁴⁰²⁾. CB concentration slightly affects the microstructural parameters of the composites like melting temperature, glass-transition temperature, Avrami kinetic parameters, etc.⁽⁴⁰⁴⁾. Wu and coworkers studied the effect of fluorinated carbon black on the dispersion and electrical conductivity. It was observed that the percolation becomes gradual and percolation concentration increases towards high fluorine content⁽⁴⁰⁵⁾.

Levi et al., have shown that α to β conversion of PVDF occurs in solution blended PVDF/Carbon nanotube composites and the ratio between these two crystalline phases varies depending on the weight %age of Carbon nanotubes. All the four phases were obtained in the blends depending on the weight percentage. They

also obtained significant changes in the piezo- and pyro- electric properties⁽⁴⁰⁶⁾. A three-phase composite with multi-walled carbon nanotubes (MWNTs) and BaTiO₃ particles embedded into Polyvinylidene fluoride was prepared by using a simple blending and hot-molding technique by Dang et al. The dielectric measurement results show that the effective dielectric constant of the composite is slightly dependant on the frequency below 1 MHz but increases rapidly with the MWNTs concentration when the concentration is very close to the percolation threshold⁽⁴⁰⁷⁾. PVDF/DMF electro-spun with Carbon nanotubes (CNT) show a percolation threshold for insulator to conductor transition depending on the concentration of CNT in the PVDF/DMF/CNT solution⁽⁴⁰⁸⁾.

1.9 Scope of Present Investigation

The work presented in this thesis deals with preparation and properties of PVDF/Clay nanocomposites using organophilic clays and two grades of PVDF. The effect of the type of organic treatment and its contents on the structure and properties of PVDF/Clay nanocomposites is evaluated. The work involves the study of crystallization behavior, static and dynamic mechanical properties and dielectric properties.

1.10 Objectives

The objectives of this study are to prepare the nanocomposites of PVDF using commercially available organically treated clays and to evaluate the effect of clay on the crystal structure, crystallization, static and dynamic properties and dielectric properties of PVDF.

The main objectives of this study are as follows,

1. To prepare nanocomposites of PVDF and organically treated montmorillonite clay by melt intercalation.
2. To study the effect of clay and intercalation on the crystal structure, crystallization and morphology, stability of the crystal structure of PVDF in the nanocomposites.
3. To study the effect of addition of clay on the mechanical (static as well as dynamic) and dielectric properties of PVDF.

4. To study the effect of two grades of PVDF having high and low viscosity on the formation and properties of nanocomposites.

The following techniques have been used to characterize the nanocomposites,

1. Structure of nanocomposite and crystal structure of PVDF by X-ray diffraction (XRD)
2. Characteristic vibration bands of different crystalline phases using Fourier Transform Infrared Spectroscopy (FTIR)
3. Dispersion of clay in PVDF by Transmission Electron Microscopy (TEM)
4. Crystalline morphology by Optical Microscope (OM)
5. Melting and crystallization behaviour by Differential Scanning Calorimeter (DSC)
6. Mechanical performance- tensile and impact properties by Universal Testing Machine (UTM) and Ceast Impact Tester
7. Dynamic mechanical properties in solid state by Dynamic Mechanical Analyzer (DMA)
8. Dynamic properties in melt state using Strain controlled rheometer
9. Frequency dependant Dielectric constant by Dielectric Analyzer

References

1. N.Herron, D. L. Thorn, *Advanced Materials*, **10**, 1173(1998)
2. E. Ruckenstein, Y. N. Yuan, *Polymer*, **38**, 3855 (1997)
3. W.Helbert, J.Y. Cavaille, A.Dufresne, *Polymer Composites*, **17**,604 (1996)
4. P. Hajji, J. Y. Cavaille, V.favier, C. Gauthier, G. Vigier, *Polymer Composites*, **17**, 612 (1996)
5. BKG Theng, *The chemistry of clay-organic reactions*. Wiley, New York (1974)
6. B. K. G. Theng, *formation and properties of clay polymer complexes*. Elsevier, NewYork (1979)
7. Y. Kojima, A. Usuki, M. Kawaasumi, A. Okada, Y. Fukushima, T. Kuruanchi, O. Kamigaito, *Journal of Materials Research*, **1**, 1185 (1993)
8. G. W. Brindley, G. Brown, *Crystal structures of clay minerals and their X-ray identification*, Mineralogical Society Monograph number 5 (1984)
9. U. Hoffmann, K. Endell, and D. Wilm, *Z. Krist.*, **86**, 340 (1933)
10. J. Battacharya, S. Talapatra, S. K. Saha, *Journal of Applied Polymer Science*, **39**, 2237 (1990)
11. M. Okamoto, S. Morita, T. Kokata, *Polymer*, **42**, 2685 (2001)
12. D. C. Lee, L. W. Jang, *Journal of Applied Polymer Science*, **61**, 1117 (1996)
13. Z. Gao, W. Xie, J. M. Hwu, L Wells, W. P. Pan, *Journal of thermal Analysis and Calorimetry*, **64**, 467 (2001)
14. W. Zhang, Y. Li, L. Wei, Y. Fang, *Materials letters*, **57**, 3366 (2003)
15. J. H. Park, S. C. Jana, *Polymer*, **44**, 2091 (2003)
16. Y. Li, B. Zhao, S. Xi, S. Zhang, *Polymer international*, **52**, 892-898 (2003)
17. P. Meneghetti, S. Qutubuddin, *Langmuir*, **20**, 3424 (2004)
18. Y. Xu, W. J. Brittain, C. Xue, R.K. Eby, *Polymer*, **45**, 3735 (2004)
19. S. Kumar, J. P. Jog, U. Natarajan, *Journal of Applied Polymer Science*, **89**, 1186 (2003)
20. F. Dietsche, Yi Thomann, R. Mulhaupt, *Journal Of Applied Polymer Science*, **75**, 396 (2000)

21. Z. Chen, C. Huang, S. Liu, Y. Zhang, K. Gong, *Journal Of Applied Polymer Science*, **75**, 796 (2000)
22. J. Lin, Z. Yang, M. Pu, *Macromolecular rapid communication*, **22**, 422 (2001)
23. Y.S. Choi, Wang KH, Xu M, Chung IJ. *Chemistry of Materials*, **14**, 2936 (2002)
24. R. Krishnamoorthy, J. Ren, A. Siva, *Journal of Chemical Physics*, **114**, 4968 (2001)
25. Y. Wei, D. Yang, L. Tang, *Journal of Materials Research*, **8**, 1143 (1993)
26. Y. T. Lim, O. O. Park, *Macromolecules Rapid communication*, **21**, 231 (2000)
27. B. Hoffmann, C. Dietrich, R. Thomann, C. Friedrich, R. Mulhaupt, *Macromolecules Rapid communication*, **21**, 57 (2000)
28. J. Zhu, C. A. Wilkie, *Polymer International*, **49**, 1158 (2000)
29. M. W. Noh, D. C. Lee, *Polymer Bulletin*, **42**, 619 (1999)
30. S. S. Lee, C. S. Lee, M. H. Kim, S. Y. Kwak, M. Park, S. Lim, C. R. Choi, J. Kim, *Journal of Polymer Science Part B; Polymer Physics*, **39**, 2430 (2001)
31. M. B. Koo, *Polymer Bulletin*, **45**, 183 (2000)
32. X. Fu, S. Qutubuddin, *Materials Letters*, **42**, 12 (2000)
33. M. Laus, M. Camerani, M. Lelli, K. Sparnacci, F. Sandrolini, *Journal Of Materials Science*, **33**, 2883 (1998)
34. A. S. Moet, A. Akelah, *Materials Letters*, **18**, 97 (1993)
35. W. M. R. Divigalpittya, R. F. Frindt, S. R. Morrison, *Journal of Materials Research*, **6**, 1103 (1991)
36. P. Pramanik, *Popular Plastics and Packaging*, 63 (1997)
37. R. A. Vaia, K. D. Jandt, E. J. Kramer, E. P. Giannelis, *Chemistry of Materials*, **8**, 2628 (1996)
38. G. Chen, S. Liu, S. Zhang, Z. Qi, *Macromolecules Rapid communications*, **21**, 746 (2000)
39. R. Krishnamoorti, R. A. Vaia, E. P. Giannelis, *Chemistry of Materials*, **8**, 1728 (1996)

40. R. A. Vaia, K. D. Jandt, E. J. Kramer, E. P. Giannelis, *Macromolecules*, **28**, 8080 (1995)
41. C. R. Tseng, H. Y. Lee, F. C. Chang, *Journal Of Polymer Science Part B: Polymer Physics*, **39**, 2097 (2001)
42. D. Lopez, I. Cendoya, F. Torres, J. Tejada, C. Mijangos, *Polymer Engineering Science*, **41**, 1845 (2001)
43. M. Zaneti, S. Lomakin, G. Camino, *Macromolecular Materials and Engineering*, **279**, 1 (2000)
44. M. Xiao, L. Sun, J. Liu, Y. Li, K. Gong, *Polymer*, **43**, 2245 (2002)
45. F. Gao, S. Chen, B. Hull, *Journal of Materials Science Letters*, **20**, 1807 (2001)
46. S. I. Ohta, H. Nakazawa, *Applied Clay Science*, **9**, 425 (1995)
47. G. Chen, Y. Ma, Z. Qi, *Scripta Materialia*, **44**, 125 (2001)
48. C. I. Park, O. O. Park, J. G. Lim, H. J. Kim, *Polymer*, **42**, 7465 (2001)
49. D. Voulgaris, D. Petridis, *Polymer*, **45**, 2213 (2002)
50. C. Zilg, P. Dietsche, B. Hoffmann, C. Dietrich, R. Mulhaupt, *Macromolecular Symposia*, **169**, 65 (2001)
51. J. Fan, S. Liu, G. Chen, Z. Qi, *Journal Of Applied Polymer science*, **83**, 66 (2002)
52. G. Chen, S. Liu, Z. Qi, *Macromolecular Chemistry and Physics*, **202**, 1189 (2001)
53. S. W. Kim, W. H. Jo, M. S. Lee, M. B. Ko, J. Y. Jho, *Polymer*, **42**, 9837 (2001)
54. M. Okomoto, S. Morita, H. Taguchi, Y. H. Kim, T. Kokata, H. Tateyama, *Polymer*, **41**, 3887 (2000)
55. X. Fu, S. Qutubuddin, *Polymer*, **42**, 807 (2001)
56. R. A. Vaia, K. D. Jandt, E. J. Kramer, E. P. Giannelis, *Chemistry of Materials*, **8**, 2628 (1996)
57. Y. T. Lim, O. O. Park, *Korean Journal Chemical Engineering*, **18**, 21 (2001)
58. J. Ren, A. S. Silva, R. Krishnamoorti, *Macromolecules*, **33**, 3739 (2000)

59. C. A. Mitchell, R. Krishnamoorti, *Journal Of Polymer Science Part B; Polymer Physics*, **40**, 1434 (2002)
60. Y. Li, H. Ishida, *Polymer*, **44**, 6571 (2003)
61. S. SU, C. A. Wilkie, *Journal Of Polymer Science Part A; Polymer Chemistry*, **41**, 1124 (2003)
62. J. T. Yoon, W. H. Jo, m. S. Lee, M. B. Ko, *Polymer*, **42**, 329 (2001)
63. T. H. Kim, S. T. Lim, C. H. Lee, H. J. Choi, M. S. Jhon, *Journal of applied Polymer Science*, **87**, 2106 (2003)
64. F. L. Beyer, N. C. Bek Tan, A. Dasgupta, M. E. Galvin, *Chemistry of Materials*, **14**, 2983 (2002)
65. C. R. Tseng, J. Y. Wu, H. Y. Lee, F. C. Chang, *Polymer*, **42**, 10063 (2001)
66. N. Gungor, S. Karaglan, *Materials Letters*, **48**, 168 (2001)
67. K. Haraguchi, T. Takeishi, S. Fan, *Macromolecules*, **35**, 10162 (2002)
68. Y. Komori, Y. Sugahara, K. Kuroda, *Journal of Materials Chemistry*, **9**, 3081 (1999)
69. K. E. Strawhecker, E. Manias, *Chemistry of Materials*, **12**, 2943 (2000)
70. I. Cendoya, D. Lopez, A. Algeria, C. Mijangos, *Journal of Polymer science Part B: Polymer Physics*, **39**, 1968 (2001)
71. Y. Komori, Y. Sugahara, K. Kuroda, *Chemistry of Materials*, **11**, 3 (1999)
72. T. W. Lee, O. O. Park, J. Yoon, J. J. Kim, *Advanced Materials*, **13**, 211 (2001)
73. T. W. Lee, O. O. Park, J. J. Kim, J. M. Hong, Y. C. Kim, *Chemistry of materials*, **13**, 2217 (2001)
74. J. J. Tunney, C. Detellier, *Chemistry of Materials*, **8**, 927 (1996)
75. D. J. Suh, O. O. Park, *Journal of Applied Polymer Science* , **83**, 2143 (2002)
76. C. Wan, X. Qiao, Y. Zhang, *Polymer Testing*, **22**, 453 (2003)
77. Hsu SLC, Chang KC., *Polymer*, **43**, 4097 (2002)
78. J. Ren, A. S. Silva, R. Krishnamoorti, *Macromolecules*, **33**, 3739 (2000)
79. C. A. Mitchell, R. Krishnamoorti, *Journal Of Polymer Science Part B; Polymer Physics*, **40**, 1434 (2002)

80. A. Usuki, Y. Kojima, M. Kawasumi, A. Okada, Y. Fukushima, T. Kurauchi, O. Kamigaito, *Journal of Materials Research*, **8**, 1174 (1993)
81. A. Usuki, Y. Kojima, M. Kawasumi, A. Okada, Y. Fukushima, T. Kurauchi, O. Kamigaito, *Journal of Materials Research*, **8**, 1179 (1993).
82. Y. Kojima, A. Usuki, M. Kawasumi, A. Okada, Y. Fukushima, T. Kuranchi, O. Kamigaito, *Journal of Materials Research*, **8**, 1185 (1993)
83. Y. Kojima, A. Usuki, M. Kawasumi, A. Okada, T. Kuranchi, O. Kamigaito, *Journal Of Polymer Science Part A: Polymer Chemistry*, **31**, 1755 (1993)
84. A. Usuki, A. Koiwai, Y. Kojima, M. Kawasumi, A. Okada, T. Kuranchi, O. Kamigaito, *Journal Of Applied Polymer Science*, **55**, 119 (1995)
85. Y. Kojima, A. Usuki, M. Kawasumi, A. Okada, T. Kuranchi, O. Kamigaito, K. Kaji, *Journal Of Polymer Science Part B: Polymer Physics*, **33**, 1039 (1995)
86. Y. Kojima, A. Usuki, M. Kawasumi, A. Okada, T. Kuranchi, O. Kamigaito, *Journal Of Applied Polymer Science*, **49**, 1259 (1993)
87. L. Liu, Z. Qi, X. Zhu, *Journal of Applied Polymer Science*, **71**, 1133 (1999)
88. M. A. Akkepadi, *Antec*, **Vol II**, 1619 (1999)
89. J. W. Cho, D. R. Paul, *Polymer*, **42**, 1083 (2001)
90. J. S. Shelley, P. T. Mather, K. L. DeVries, *Polymer*, **42**, 5849 (2001)
91. S. H. Wu, F. Y. Wang, C. C. M. Ma, W. C. Chang, C. T. Kuo, H. C. Kuan, W. J. Chen, *Materials Letters*, **49**, 327 (2001)
92. X. Liu, Q. Wu, L. A. Berglund, J. Fan, Z. Qi, *Polymer*, **42**, 8235 (2001)
93. G. M. Kim, D. H. Lee, B. Hoffmann, J. Kressler, G. Stoppelmann, *Polymer*, **42**, 1095 (2001)
94. T. D. Fornes, P. J. Yoon, H. Keskkula, D. R. Paul, *Polymer*, **42**, 9929 (2001)
95. F. Yang, Y. Ou, Z. Yu, *Journal Of Applied Polymer Science*, **69**, 355 (1998)
96. A. Usuki, N. Hasegawa, H. Kadoura, T. Okamoto, *Nanoletters*, **1**, 271 (2001)
97. A. Okada, A. Usuki, T. Kuranchi, O. Kamigaito, *Chapter 6, ACS Symposium series*, **585**, 55 (1995)
98. S. Murase, A. Inoue, Y. Miyashita, N. Kimura, Y. Nishiio, *Journal of Polymer Science Part B; Polymer Physics*, **40**, 479 (2002)

99. N. Hasegawa, H. Okamoto, M. Kato, A. Usuki, N. Sato, *Polymer*, **44**, 2933 (2003)
100. L. Loo, K. Gleason, *Polymer*, **45**, 5933 (2004)
101. F. J. Medellin-Rodriguez, B. S. Hsiao, B. Chu, B. X. Fu, *Journal Of Macromolecular Science Part B : Physics*, **B42**, 201 (2003)
102. N. Hasegawa, H. Okamoto, M. Kato, A. Usuki, N. Sato, *Polymer*, **44**, 2933 (2003)
103. X. Liu, Q. Wu, L. A. Burglund, H. Linderg, J. Fan, Z. Qi, *Journal of Applied Polymer Science*, **88**, 953 (2003)
104. R. D. Davis, J. W. Gilman, D. L. VanderHart, *Polymer Degradation and stability*, **79**, 111 (2003)
105. Q. Wu, X. Liu, L. A. Berglund, *Polymer*, **43**, 2445 (2002)
106. P. J. Yoon, T. D. Fornes, D. R. Paul, *Polymer*, **43**, 6727 (2002)
107. G. Zhan, D. Yan, *Journal Of Applied Polymer Science*, **88**, 2181 (2003)
108. C.C. Ma, C. T. Kuo, H. C. Kuan, C. L. Chiang, , *Journal Of Applied Polymer Science*, **88**, 1686 (2003)
109. T. X. Liu, Z. H. Liu, K. X. Ma, L. Shen, K. Y. Zeng, C. B. He, *Composites Science and Technology*, **63**, 331 (2003)
110. X. Liu, Q. Wu, *Polymer*, **43**, 1933 (2002)
111. Y. Kojima, T. Matsouka, H. Takahashi, T. Kuruanchi, *Journal Of Applied Polymer Science*, **51**, 683 (1994)
112. T. Wu, C. Liao, *Macromolecular Chemistry and Physics*, **201**, 2820 (2000)
113. Z. Wu, C. Zhou, N. Zhu, *Polymer Testing*, **21**, 479 (2002)
114. T. Liu, K. P. Lim, W. C. Tiju, K. P. Pramoda, Z. K. Chen, *Polymer*, **44**, 3529 (2003)
115. T. D. Fornes, P. J. Yoon, H. Keskkula, D. R. Paul, *Polymer*, **42**, 9929 (2001)
116. G.M. Kim, D.H. Lee, B. Hoffmann, J. Kressler, G. Stoppelmann, *Polymer*, **42**, 1095 (2001)
117. G. Jimenez, N. Ogata, H. Kawai, T. Ogihara, *Journal of Applied Polymer Science*, **64**, 2211 (1997)

118. P. B. Messersmith, E. P. Giannelis, *Journal of Polymer Science Part B: Polymer Physics*, **33**, 1047 (1995)
119. B. Lepoittevin, M. Devalckenaere, N. Pantoustier, , M. Alexxandre, D. Kubies, C. Calberg, R. Jerome, P. Dubois, *Polymer*, **43**, 4017 (2002)
120. Y. Di, S. Iannace, E. D. Maio, L. Nicolais, *Journal Of Polymer Science Part B: Polymer Physics*, **41**, 670 (2003)
121. P. B. Messersmith, E. P. Giannelis, *Chemistry of Materials*, **5**, 1064, (1993)
122. C. H. Davis, L. J. Mathias, J. W. Gilman, D. A. Schiraldi, J. Randy Shields, P. Trulove, T. E. Sutto, H. C. Delong, *Journal of Polymer Science Part B: Polymer Physics*, **40**, 2661 (2002)
123. Y. Ke, C. Long, Z. Qi, *Journal Of Applied Polymer Science*, **71**, 1139 (1999)
124. Y. Imai, S. Nishimura, E. Abe, H. Tateyama, A. Abiko, A. Yamaguchi, T. Aoyama, H. Taguchi, *Chemistry of Materials*, **14**, 477 (2002)
125. C. F. Ou, *Journal Of Applied Polymer Science*, **89**, 3315 (2003)
126. A. R. Tripathy, E. Burgaz, S. N. Kukureka, J. Macknight, *Macromolecules*, **36**, 8593 (2003)
127. B. J. Crisholm, R. B. Moore, G. Barber, F. Khouri, A. Hampstead, M. Larsen, E. Olson, J. Kelley, G. Balch, J. Caraher, *Macromolecules*, **35**, 5508 (2002)
128. X. Li, T. Kang, W. J. Cho, J. K. Lee, C. S. Ha, *Macromolecules Rapid Communication*, **22**, 1306 (2001)
129. Y. C. Ke, Z. B. Yang, C. F. Zhu, *Journal Of Applied Polymer Science*, **85**, 2677 (2002)
130. X. Kornmann, L. Berglund, J. Sterte, *Polymer Engineering and Science*, **38**, 1351-1358, 1998
131. R. K. Bharadhwaj, A. R. Mehrabi, C. Hamilton, C. Trujillo, M. Murga, R. Fan, A. Chavira, A.K. Thompson, *Polymer*, **43**, 3699 (2002)
132. J. H. Chang, D. K. Park, *Polymer Bulletin*, **47**, 191 (2001)
133. J. H. Chang, D. K. Park, *Journal Of Polymer Science Part B: Polymer Physics*, **39**, 2581 (2001)
134. R. A. Kalgaonkar, J. P. Jog, *Journal Of Polymer Science Part B; Polymer Physics*, **41**, 3102 (2003)

135. X. Huang, S. Lewis, W. J. Brittain, *Macromolecules*, **33**, 2000 (2000)
136. P. J. Yoon, D. L. Hunter, D. R. Paul, *Polymer*, **44**, 5341 (2003)
137. K. M. Lee, C. D. Han, *Polymer*, **44**, 4573 (2003)
138. R. A. Via, B. B. Sauer, O. K. Tse, E. P. Giannelis, *Journal of Polymer Science Part B: Polymer Physics*, **35**, 59 (1997)
139. J. E. Mark, C. Y-C Lee, P. A. Bianconi, *ACS symposium Series*, **Chapter 5** (1994)
140. R. A. Vaia, B. B. Sauer, O. K. Tse, E. P. Giannelis, *Journal of polymer science Part B: Polymer Physics*, **35**, 59 (1997)
141. N. Ogata, S. Kawakage, T. Ogihara, *Journal of Applied Polymer science*, **66**, 573 (1997)
142. H. R. Fischer, L. H. Gielgens, T. P. M. Kosier, *Acta Polymerica*, **50**, 122 (1999)
143. J. Bujdak, E. Hackett, E. P. Giannelis, *Chemistry of Materials*, **12**, 2168 (2000)
144. E. Hackett, E. Manias, E. P. Giannelis, *Chemistry of Materials*, **12**, 2161 (2000)
145. B. Liao, M. Song, H. Liang, Y. Pang, *Polymer*, **42**, 10007 (2001)
146. P. Aranda, E. R. Hitzky, *Applied Clay Science*, **15**, 119 (1999)
147. K. E. Strawhecker, E. Manias, *Chemistry of Materials*, **15**, 844 (2003)
148. N. Oztekin, A. Alemdar, N. Gungor, F. B. Erim, *Materials Letters*, **55**, 73 (2002)
149. S. D. Burnside, E. P. Giannelis, *Chemistry of Materials*, **7**, 1597 (1995)
150. P. B. Messersmith, E. P. Giannelis, *Chemistry of Materials*, **6**, 1719 (1994)
151. C. Zilg, R. Mulhopt, J. Finter, *Macromolecular Chemistry and Physics*, **200**, 661 (1999)
152. X. Kornmann, H. Lindberg, L. A. Berglund, *Polymer*, **42**, 1303 (2001)
153. T. Lan, T. J. Pinnavia, *Chemistry of Materials*, **6**, 2216 (1994)
154. Z. Wang, T. J. Pinnavia, *Chemistry of materials*, **10**, 1820 (1998)
155. T. J. Pinnavia, T. Lan, Z. Wang, H. Shi, P. D. Kairatna, *Chapter 17, ACS Symposium series*, **622**, 250 (1996)

156. D. C. Lee, L. W. Jang, *Journal of Applied Polymer Science*, **68**, 1997 (1998)
157. H. Shi, T. Lan, T. J. Pinnavia, *Chemistry of Materials*, 1584, **8** (1996)
158. T. Lan, P. D. Kaviratna, T. J. Pinnavia, *Chemistry of Materials*, **7**, 2144 (1995)
159. M. S. Wang, T. J. Pinnavia, *Chemistry of Materials*, **6**, 468 (1994)
160. Z. Wang, T. Lan, T. J. Pinnavia, *Chemistry of Materials*, **8**, 2200 (1996)
161. T. Lan, P. D. Kaviratna, T. J. Pinnavia, *Journal Physics and Chemistry of Solids*, **57**, 1005 (1996)
162. T. Lan, Z. Wang, H. Shi, T. J. Pinnavia, *Proceedings of the ACS Division of Polymeric materials: Science and Engineering*, **73**, 296 (1995)
163. A. Lee, J. D. Lichtenhan, *Journal of Applied Polymer Science*, **73**, 1993 (1999)
164. P. Kelly, A. Akelah, S. Qutubuddin, A. Moet, *Journal of Materials Science*, **29**, 2274 (1994)
165. W. B. Xu, S. P. Bao, P. S. He, *Journal of Applied Polymer Science*, **84**, 842 (2002)
166. Z. Wang, T. J. Pinnavia, *Chemistry of Materials*, **10**, 3769 (1998)
167. T. K. Chen, T. I. Tien, K. H. Wei, *Polymer*, **41**, 1345 (2000)
168. C. Zilg, R. Thomann, R. Mulhaupt, J. Finter, *Advanced Materials*, **11**, 49 (1999)
169. T. K. Chen, Y. I. Tien, K. H. Wei, *Journal Of Polymer Science Part A: Polymer Chemistry*, **37**, 2225 (1999)
170. R. Xu, E. Manias, A. J. Snyder, J. Runt, *Macromolecules*, **34**, 337 (2001)
171. K. J. Yao, M. Song, D. J. Hourston, D. Z. Luo, *Polymer*, **43**, 1017 (2002)
172. J. H. Chang, Y. U. An, *Journal Of Polymer Science Part B: Polymer Physics*, **40**, 670 (2002)
173. R. Xu, E. manias, A. J. Snyder, J. Runt, R. A. Vaia, *Macromolecules*, **34**, 337 (2001)
174. Y. H. Yu, J. M. Yeh, S. J. Liou, Y. P. Chang, *Acta Materialia*, **52**, 475 (2004)
175. C. Nah, S. H. Han, J. H. Lee, M. H. Lee, S. D. Lim, J. M. Rhee, *Composites: Part B*, **35**, 125 (2004)

176. J. M. Yeh, C. L. Chen, T. H. Kuo, W. F. Su, H. Y. Huang, D. J. Liaw, H. Y. Lu, C. F. Liu, Y. H. Yu, *Journal Of Applied Polymer Science*, **92**, 1072 (2004)
177. Changwoon Nah, S. H. Han, J. H. Lee, M. H. Lee, K. H. Chung, *Polymer International*, **53**, 891 (2004)
178. H. B. Hsueh, C. Y. Chen, *Polymer*, **44**, 1151 (2003)
179. D. M. Delozier, R. A. Orwoll, J. F. Cahoon, N. J. Johnston, J. G. Smith Jr., J. W. Connell, *Polymer*, **43**, 813 (2002)
180. L. Y. Jiang, K. W. Wei, *Journal of applied Physics*, **92**, 6219 (2002)
181. R. Magaraphan, W. Lillayuthalert, A. Sirivat, J. W. Schwank, *Composites Science and Technology*, **61**, 1253 (2001)
182. T. Agag, T. Koga, T. Takeichi, *Polymer*, **42**, 3399 (2001)
183. J. H. Chang, K. M. Park, D. Cho, H. S. Yang, K. J. Ihn, *Polymer Engineering and Science*, **41**, 1514 (2001)
184. H. L. Tyan, K. H. Wei, T. E. Hsieh, *Journal Polymer Science Part B: Polymer Physics*, **38**, 2873 (2000)
185. H. L. Tyan, Y. C. Liu, K. H. Wei, *Chemistry of Materials*, **11**, 1942 (1999)
186. H. L. Tyan, Y. C. Liu, K. H. Wei, *Polymer*, **40**, 4877 (1999)
187. Y. Yang, Z. K. Zhu, J. Yin, X. Y. Wang, Z. E. Qi, *Polymer*, **40**, 4407 (1999)
188. T. Lan, P. D. Kaviratna, T. J. Pinnavia, *Chemistry of Materials*, **6**, 573 (1994)
189. T. J. Pinnavia, T. Lan, P. D. Kairatna, M. S. Wang, *Materials Research Society Proceedings*, **346**, 81 (1994)
190. K. Yano, A. Usuki, A. Okada, T. Kuruanchi, O. Kamigaito, *Journal Polymer Science Part A: Polymer Chemistry*, **31**, 2493 (1993)
191. K. Yano, A. Usuki, A. Okada, *Journal Polymer Science Part B: Polymer Physics*, **35**, 2289 (2002)
192. H. L. Tyan, K. H. Wei, T. E. Hsieh, *Journal Polymer Science Part B: Polymer Physics*, **38**, 2873 (2000)
193. J. H. Chang, D. K. Park, K. J. Ihn, *Journal of Applied Polymer Science*, **84**, 2294 (2002)
194. C. M. Leu, Z. W. Wu, K. H. Wei, *Chemistry of Materials*, **14**, 3016 (2002)

195. A.B. Morgan, J. W. Gilman, C. L. Jackson, *Macromolecules*, **34**, 2735 (2001)
196. G. S. Sur, H. L. Sun, S. G. Lyu, J. E. Mark, *Polymer*, **42**, 9783 (2001)
197. S. H. Gu, J. Ren, Q. F. Wang, *Journal of Applied Polymer Science*, **91**, 2427 (2004)
198. Y.Q. Zhang, J. H. Lee, J. M. Rhee, K. Y. Rhee, *Composites Science and Technology*, **64**,1383 (2004)
199. Z. M. Wang, H. Nakajima, E. Manias, T. C. Chung, *Macromolecules*, **36**, 8919 (2003)
200. W. Zheng, X. Lu, C. L. Toh, T. H. Zheng, C. He, *Journal of Polymer Science Part B: Polymer Physics*, **42**, 1810 (2004)
201. Y. Weng, F. B. Chen, Y. C. Li, K. C. Wu, *Composites Part B: Engineering*, **35**, 111 (2004)
202. D. G. Lopez, O. Picazo, J. C. Merino, J. M. Pastor, *European Polymer Journal*, **39**, 945 (2003)
203. Y. Q. Zhang, J. H. Lee, H. J. Jang, C. W. Nah, *Composites Part: Engineering*, **35**, 133 (2004)
204. J. Li, C. Zhou, G. Wang, D. Zhao, *Journal of Applied Polymer Science*, **89**, 318 (2003)
205. A. B. Morgan, J. D. Harris, *Polymer*, **44**, 2313 (2003)
206. Y. Tang, Y. Hu, L. Song, R. Zong, Z. Gui, Z. Chen, W. Fan, *Polymer Degradation and Stability*, **82**, 127 (2003)
207. X. Liu, Q. Wu, *Polymer*, **42**, 10013 (2001)
208. X. Zhang, M. Yang, Y. Zhao, S. Zhang, X. Dang, x. Liu, D. Wang, D. Xu, *Journal of Applied Polymer Science*, **92**, 552 (2004)
209. C. M. Koo, M. J. Kim, M. H. Choi, S. O. Kim, I. J. Chung, *Journal of Applied Polymer Science*, **88**, 1526 (2003)
210. W. Xu, G. Liang, W. Wang, S. Tang, P. He, W. Pan, *Journal of Applied Polymer Science*, **88**, 3225 (2003)
211. S. Boucard, J. Duchet, J. F. Jerard, P. Prele, S. Gonzales, *Macromolecular Symposium*, **194**, 241 (2003)

212. S. Morlat, B. Mailhot, D. Gonzales, J. L. Gardette, *Chemistry of Materials*, **16**, 377 (2004)
213. Q Zhang, Q. Fu, L. Jiang, Y. Lei, *Polymer International*, **49**, 1561 (2000)
214. N. Hasegawa, H. Okamoto, M. Kato, A. Usuki, *Journal of Applied Polymer Science*, **78**, 1918 (2000)
215. W. Xu, M. Ge, P. He, *Journal of Polymer Science Part B: Polymer Physics*, **40**, 408 (2002)
216. U. Wagenknecht, B. Kretschmar, G. Reinhardt, *Macromolecular Symposium*, **194**, 207 (2003)
217. E. Manias, A. Touny, L. Wu, K. Strawhecker, B. Lu, T. C. Chung, *Chemistry of Materials*, **13**, 3516 (2001)
218. E. Manias, A. Touny, L. Wu, B. Lu, K. Strawhecker, J. W. Gilman, T. C. Chung, *Polymeric materials: Science and Engineering*, **82**, 282 (2000)
219. J. W. Gilman, C. L. Jackson, A. B. Morgan, R. Harris Jr., E. Manias, E. P. Giannelis, M. Wuthenow, D. Hilton, S. H. Philips, *Chemistry of Materials*, **12**, 1866 (2000)
220. J. Lee, Y. T. Lim, O. O. Park, *Polymer Bulletin*, **45**, 191 (2000)
221. M. Okamoto, P. H. Nam, P. Maiti, T. Kotaka, N. Hasegawa, *Nano Letters*, **1**, 295 (2001)
222. M. Kato, A. Usuki, A. Okada, *Journal of Applied Polymer Science*, **66**, 1781 (1997)
223. J. M. Gloaguen, J. M. Lefebvre, *Polymer*, **42**, 5841 (2001)
224. S. Hambir, N. Bulakh, P. Kodgire, R. Kalgaonkar, J. P. Jog, *Journal of Polymer Science Part B: Polymer Physics*, **39**, 446 (2001)
225. M. Kawasumi, N. Hasegawa, M. Kato, A. Usuki, A. Okada, *Macromolecules*, **30**, 6333 (1997)
226. N. Hasegawa, M. Kawasumi, M. Kato, A. Usuki, A. Okada, *Journal of Applied Polymer Science*, **67**, 87 (1998)
227. P. H. Nam, P. Maiti, M. Okamoto, T. Kotaka, N. Hasegawa, A. Usuki, *Polymer*, **42**, 9633 (2001)

228. P. Maiti, P. H. Nam, M. Okamoto, N. Hasegawa, A. Usuki, *Macromolecules*, **35**, 2042 (2002)
229. M. Zanetti, G. Camino, P. Reichert, R. Mulhaupt, *Macromolecular Rapid Communication*, **22**, 176 (2001)
230. P. Reichert, B. Hoffmann, T. Bock, T. Thomann, R. Mulhaupt, C. Friedrich, *Macromolecular Rapid Communication*, **22**, 519 (2001)
231. P. Kodgire, R. Kalgaonkar, S. Hambir, N. Bulakh, J. P. Jog, *Journal of Applied Polymer Science*, **81**, 1786 (2001)
232. M. Okamoto, P. H. Nam, P. Maiti, T. Kotaka, T. Nakayama, M. Takada, M. Ohshima, A. Usuki, N. Hasegawa, H. Okamoto, *NanoLetters*, **1**, 503 (2001)
233. J. Ma, S. Zhang, Z. Qi, G. li, Y. Hu, *Journal of Applied Polymer Science*, **83**, 1978 (2002)
234. T. Sun, J. M. Garces, *Advanced Materials*, **14**, 128 (2002)
235. M. Zanetti, G. Camino, D. Canace, A. B. Morgan, F. J. Lamelas, C. A. Wilkie, *Chemistry of Materials*, **14**, 189 (2002)
236. S. C. Tjong, Y. Z. Meng and A. S. Hay, *Chemistry of Materials*, **14**, 44 (2002)
237. G. Galgali, C. Ramesh, A. Lele, *Macromolecules*, **34**, 852 (2003)
238. K. N. Kim, H. Kim, J. W. Lee, *Polymer Engineering and Science*, **14**, 1963 (2001)
239. N. Hasegawa, A. Usuki, *Journal of Applied Polymer Science*, **93**, 464 (2004)
240. S. Y. Gu, J. Ren, Q. F. Wang, *Journal of Applied Polymer Science*, **91**, 2427 (2004)
241. D. Wang, C. A. Wilkie, *Polymer Degradation and stability*, **80**, 171 (2003)
242. M. J. Solomon, A. S. Almusallam, K. F. Seefeldt, A. Somwangthanoraj, P. Varadhan, *Macromolecules*, **34**, 1864 (2001)
243. W. Xu, G. Liang, W. Wang, S. Tang, P. He, W. Pan, *Journal Of Applied Polymer Science*, **88**, 3093 (2003)
244. C. M. Koo, H. T. Ham, S. O. Kim, K. H. wang, I. J. Chung, D. C. Kim, W. C. Zin, *Macromolecules*, **35**, 5116 (2002)

245. M. Alexandre, P. Dubois, T. Sun, J. M. Garces, R. Jerome, *Polymer*, **43**, 2123 (2002)
246. T. G. Gopakumar, J. A. Lee, M. Kontopoulou, J. S. Parent, *Polymer*, **43**, 5483 (2002)
247. H. G. Jeon, H. T. Jung, S. W. Lee, S. D. Hudson, *Polymer Bulletin*, **41**, 107 (1998)
248. J. Heinemann, P. Reichert, R. Thomann, R. Mulhaupt, *Macromolecular Rapid Communication*, **20**, 423 (1999)
249. K. H. Wang, M. H. Choi, C. M. Koo, Y. S. Choi, I. J. Chung, *Polymer*, **42**, 9819 (2001)
250. M. X. Ramirez, D. E. Hirt, L. L. Wright, *Nano Letters*, **2**, 9 (2002)
251. J. X. Li, J. Wu, C. M. Chan, *Polymer*, **41**, 6935 (2000)
252. S. D. Wanjale, J. P. Jog, *Journal of Polymer Science Part B: Polymer Physics*, **41**, 1014 (2003)
253. S. D. Wanjale, J. P. Jog, *Journal of Macromolecular Science Part B: Physics*, **B42**, 1141 (2003)
254. S. D. Wanjale, J. P. Jog, *Journal of Applied Polymer Science*, **90**, 3233 (2003)
255. A. W. Zhang, D. Chen, Q. Zhao, Y. Fang, *Polymer*, **44**, 7953 (2003)
256. C. H. Jeon, S. H. Ryu, Y. W. Chang, *Polymer International*, **52**, 153 (2003)
257. M. Alexandre, G. Bayer, C. Henrist, R. Cloots, A. Rulmont, R. Jerome, P. Dubois, *Macromolecular rapid communication*, **22**, 643 (2001)
258. A. Riva, M. Zanetti, M. Bragilia, G. Camino, L. Faqi, *Polymer Degradation and stability*, **77**, 299 (2002)
259. H. Zheng, Y. Zhang, Z. Peng, Y. Zhang, *Journal of applied polymer Science*, **92**, 638 (2004)
260. Mukul Biswas, Suprakash Sinha Ray, *Polymer*, **39**, 6423 (1998)
261. D. Lee, S. H. Lee, K. Char, J. Kim, *Macromolecules Rapid Communication*, **21**, 1136 (2000)
262. K. A. Karrado, L. Xu, *Chemistry of Materials*, **10**, 1440 (1998)

263. J. H. Park, Y. T. Lim, O. O. Park, *Macromolecular Rapid Communication*, **22**, 616 (2001)
264. Q. Wu, Z. Xue, Z. Qi, F. Wang, *Polymer*, **41**, 2029 (2000)
265. B. H. Kim, J. H. Jung, J. W. Kim, H. J. Choi, J. Joo, *Synthetic metals*, **121**, 1311 (2001)
266. B. H. Kim, J. H. Jung, S. H. Hong, J. W. Kim, H. J. Choi, J. Joo, *Current Applied Physics*, **1**, 112 (2001)
267. H. L. Frisch, Bangwei Xi, Y. Qin, M. Rafailovich, *High Performance Polymers*, **83**, 543 (2000)
268. D. Orata, F. Segor, *Reactive and Functional Polymers*, **43**, 305 (2000)
269. H. J. Choi, J. W. Kim, J. Joo, B. H. Kim, *Synthetic Metals*, **121**, 1325 (2001)
270. Y. T. Lim, J. H. Park, O. O. Park, *Journal of Colloidal and Interface Science*, **245**, 198 (2002)
271. M. A. Paul, M. Alexandre, P. Degee, C. Henrist, A. Rulmont, P. Dubois, *Polymer*, **44**, 443 (2003)
272. K. Okamoto, S. S. Ray, M. Okamoto, *Journal of Polymer Science Part B: Polymer Physics*, **41**, 3160 (2003)
273. P. Maiti, K. Yamada, M. Okamoto, K. Ueda, K. Okamoto, *Chemistry of Materials*, **14**, 4654 (2002)
274. J. H. Chang, B. S. Soe, D. H. Hwang, *Polymer*, **43**, 2969 (2002)
275. R. A. Vaia, E. P. Giannelis, *Polymer*, **42**, 1281 (2001)
276. Y. T. Vu, J. E. Mark, L. H. Pham, M. Engelhardt, *Journal Of Applied Polymer Science*, **82**, 1391 (2001)
277. W. B. Liao, *Polymer*, **40**, 599 (1999)
278. Y. Wang, L. Zhang, C. Tang, D. Yu, *Journal of Applied Polymer Science*, **78**, 1879 (2000)
279. F. Schon, R. Thomann, W. Gronski, *Macromolecular symposia*, **189**, 105 (2002)
280. S. Joly, G. Garnaud, R. Ollitrault, L. Bokobza, J. E. mark, *Chemistry of Materials*, **14**, 4202 (2002)

281. W. Zhou, J. E. Mark, M. R. Unroe, F. E. Arnold, *Journal of Macromolecular Science: Pure and applied chemistry*, **A38**, 1 (2001)
282. W. Xu, M. Ge, P. He, *Journal Of Applied Polymer Science*, **82**, 2281 (2001)
283. S. D. Burnside, E. P. Giannelis, *Journal Polymer Science Part B: Polymer Physics*, **38**, 1595 (2000)
284. B. Lepoittevin,, N. Pantoustier, Myriam Devalckenaere, M. Alexxandre, C. Calberg, C. Henrist, A. Rulmont, P. Dubois, *Polymer*, **44**, 2033 (2003)
285. J. H. Park, S. C. Jana, *Polymer*, **44**, 2091 (2003)
286. S. K. Lim, K. I. Chin, Y. K. Kwon, H. J. Choi, *Chemistry of Materials*, **14**, 1989 (2002)
287. P. Aranda, E. Ruiz-Hitzky, *Chemistry of Materials*, **4**, 1395 (1992)
288. D. J. Greenland, *Journal of Colloid Science*, **18**, 647 (1963).
289. P. B. Messersmith, E. P Giannelis, *Chemistry of Materials*, **6**, 1719 (1994)
290. P. B. Messersmith, E. P. Giannelis, *Journal of Polymer Science Part A: Polymer Chemistry*, **33**, 1047 (1995)
291. A. Usuki, M. Kawasumi, Y. Kojima, A. Okada, T. Kurauchi, O. Kamigaito, *Journal of Materials Research*, **8**, 1174 (1993)
292. A. Usuki, Y. Kojima, M. Kawasumi, A.Okada, Y. Fukushima, T. Kurauchi, O.Kamigaito, *Journal of Materials Research*, **8**, 1179 (1993)
293. R. A. Vaia, R. K. Teukolsky, E. P. Giannelis, *Chemistry of Materials*, **6**, 1017 (1994)
294. R. A. Vaia, E. P. Giannelis, *Macromolecules*, **30**, 7990 (1997)
295. R. A. Vaia, E. P. Giannelis, *Macromolecules*, **30**, 8000 (1997)
296. A. C. Balazs, C. Singh, E. Zhulina, Y. Lyatskaya, *Accounts of Chemical Research*, **32**, 651 (1999)
297. V. V. Ginzburg, A. C. Balazs, *Advanced Materials*, **12**, 1805 (2000)
298. C.Singh, A. C. Balazs, *Polymer international*, **49**, 469 (2000)
299. A. C. Balazs, C. Singh, E. Zhulina, *Macromolecules*, **31**, 8370 (1998)
300. D. Janeba, P. Capkova, Z. Weiss, H. Schenk, *Clays and Clay Minerals*, **46**, 63 (1998)

301. R. A. Vaia, W. Lu, *Journal Polymer Science Part B: Polymer Physics*, **40**, 1590 (2002)
302. R. A. Vaia, K. D. Jandt, E. J. Kramer, E. P. Giannelis, *Macromolecules*, **28**, 8080 (1995)
303. A. Bafna, Beaucage, F. Mirabella, S. Mehta, *Polymer*, **44**, 1103 (2003)
304. A. B. Morgan, J. W. Gilman, *Journal of Applied Polymer Science*, **87**, 1329 (2003)
305. D. K. Yang, D. B. Zax, *Journal Chemical Physics*, **110**, 5253 (1991)
306. W. E. Blumberg, *Physical Review*, **119**, 79 (1960)
307. Abragam A, (editor), Chapter V, The principles of nuclear magnetism, New York: Oxford University Press; 1961.
308. D. L. Vandelhardt, A. Asano, J. W. Gilman, *Macromolecules*, **34**, 3819 (2001)
309. D. L. Vandelhardt, A. Asano, J. W. Gilman, *Chemistry of materials*, **13**, 3796 (2001)
310. F. Dietsche, Y. Thomann, R. Thomann, R. Mulhaupt, *Journal of Applied Polymer Science*, **75**, 396 (2000)
311. I. Y. Phang, K. P. Pramoda, T. Liu, C. He, *Polymer international*, **53**, 1282 (2004)
312. A. Blumstein, *Journal of Polymer Science*, **A3**, 2665 (1965)
313. J. W. Gilman, *Applied Clay Science*, **15**, 31 (1999)
314. A. Lee, J. D. Lichtenhan, *Journal of Applied Polymer Science*, **73**, 1993 (1999)
315. X. Kornmann, Ph. D. Thesis, Lulea University of Technology, Sweden, 2001
316. C. Zilg, R. Thomann, M. Baumert, J. Finter, R. Mulhaupt, *Macromolecular rapid communication*, **21**, 1214 (2000)
317. R. Krishnamoorti, K. Yurekli, *Current opinion in colloid and Interface Science*, **6**, 464 (2001)
318. R. Krishnamoorti, E. P. Giannelis, *Macromolecules*, **30**, 4097 (1997)
319. R. Krishnamoorti, R. A. Vaia, E. P. Giannelis, *Macromolecules*, **29**, 1728 (1996)

320. G. Galgali, C. Ramesh, A. Lele, *Macromolecules*, **34**, 852 (2001)
321. K. M. Lee, C. D. Han, *Macromolecules*, **36**, 804 (2003)
322. B. Hoffmann, C. Dietrich, R. Thomann, C. Friedrich, R. Mulhaupt, *Macromolecular rapid communication*, **21**, 57 (2000)
323. P. Reichert, B. Hoffmann, T. Bock, R. Thomann, R. Mulhaupt, C. Friedrich, *Macromolecular Rapid Communication*, **22**, 519 (2001)
324. R. Krishnamoorti, J. Ren, A. S. Silva, *Journal of Chemical Physics*, **114**, 4968 (2001)
325. A. Kanapitsas, P. Pissis, R. Kotsilkova, *Journal of non-crystalline solids*, **305**, 204 (2002)
326. K.C. Chang, H. W. Wang, 140.135.56.78/teachersweb/Yermlab.htm
327. E. P. M. Williams, J. C. Seferis, C. L. Whittman, G. A. Parker, J. H. Lee, J. D. Nam, *Journal of Polymer Science: Part B: Polymer Physics*, **42**, 1 (2004)
328. J. W. Gilman, *Applied Clay Science*, **15**, 31 (1999)
329. J. W. Gilman, C. L. Jackson, A. B. Morgan, R. Harris Jr., E. Manias, E. P. Giannelis, M. Wuthenow, D. Hilton, S. H. Phillips, *Chemistry of Materials*, **12**, 1866 (2000)
330. T. Kashiwagi, R. H. Harris Jr., X. Zhang, R. M. Briber, B. H. Cipriano, S. R. Raghavan, W. H. Awad, J. R. Shields, *Polymer*, **45**, 881 (2004)
331. F. Dietsche, R. Mulhaupt, *Polymer Bulletin*, **43**, 395 (1999)
332. B. J. Jungnickel, *Polyvinylidene fluoride (overview)*, *The Polymeric materials Encyclopedia*, CRC Press, 1996
333. R. Gregorio Jr., M. Cestari, N. Chaves, P. S. Nociti, J. A. Mendonca, A. A. Lucas, Poly(vinylidene fluoride) phases and morphology (Effect of crystallization conditions), *The polymeric materials encyclopedia*, 1996, CRC Press
334. M. A. Bachman, J.B. Lando, *Macromolecules*, **14**, 40 (1981)
335. L. Kutschabsk, E. Hohne and R. G. Kretschmer, *Acta polymerica*, **43**, 357 (1991)
336. R. Gregorio Jr., M. Cestari, *Journal of Polymer Science Part B: Polymer Physics*, **32**, 859 (1994)

337. R. Hasegawa, Y. Takahashi, Y. Chatani, H. Tadokoro, *Polymer Journal*, **3**, 600 (1972)
338. C. C. Hsu, P. H. Geil, *Journal of Material Science*, **24**,1219 (1989)
339. P.Sajkiewicz, A. Wasiak, Z. Goclowski, *European polymer journal*, **35**, 423 (1999)
340. R Gregorio Jr. and Marcelo Cestari, *Journal of Polymer Science Part B: Polymer Physics*, **32**, 859 (1994)
341. R. Hasegawa, M. Kobayashi, H. Tadokoro, *Polymer Journal*, **3**, 591 (1972)
342. A. Tawansi, A. H. Oraby, E. M. Abdelrazek, M. Abdelaziz, *Polymer Testing*, **18**, 569 (1999)
343. A. Tawansi, A H Oraby, S I Badr and I S Elashmawi, *Polymer International*, **53**, 370 (2004)
344. D. M. Esterly, B. J. Love, *Journal of Polymer Science Part B: Polymer Physics*, **42**, 91 (2004)
345. Y. Takahashi, A. Tadokoro, *Macromolecules*, **13**, 1318 (1980)
346. A.J.Lovinger, *Macromolecules*, **14**, 322 (1981)
347. J. H. Wendroff, *Journal of Polymer Science: Polymer Letters*, **18**, 439 (1980)
348. A. J. Lovinger, *Journal of Polymer Science: Polymer Physics*, **18**, 793 (1980)
349. W. M. Prest Jr., D. J. Luca, *Journal of Applied Physics*, **49**, **5042** (1976)
350. S. Osaki, Y. Ishida, *Journal of Applied Physics*, **13**,1071 (1975)
351. F. J. Lu, S. L. Hsu, *Macromolecules*, **19**, 32 (1986)
352. H. L. Marand, R. S. Stein, *Journal of Polymer Science Part B: Polymer Physics*, **26**,1361 (1988)
353. A. J. Lovinger, *Macromolecules*, **15**, 40 (1982)
354. G. T. Davis, J. E. Mc Kinney, M. G.Broad hurst, S. C. Roth, *Journal of Applied Physics*, **49**, 4998 (1978)
355. M. A. Bachman, W. L. Gordon, S. Weinhold, J. B. Lando, *Journal of Applied Physics*, **51**, 1980 (1980)

356. A. Tawansi, A. H Oraby, S. I. Badr, I. S. Elshmawi, *Polymer International*, **53**, 570 (2004)
357. S. L. Mendez, J. F. Mano, A. M. Costa, V. H. Schmidt, *Journal of Macromolecular Science Part B: Physics*, **B40**, 517 (2001)
358. K. M. Tashiro, H. Tadokoro, *Macromolecules*, **8**,158 (1975)
359. R. Gregorio Jr., R. C. Capitaio, *Journal Of Material Science*, **335**, 299 (2000)
360. A. J. Lovinger, *Journal of Polymer Science Part B: Polymer Physics*, **18**, 793 (1980)
361. S. Zulfiqar, M. Zulfiqar, M. Rizvi, A. Munir, I. C. McNeill, *Polymer Degradation and Stability*, **43**, 423 (1994)
362. T. C. Wen, C. Sivakumar, A. Gopalan, *Materials Letters*, **54**, 430 (2002)
363. W. M. Prest, D. J. Luca, *Journal of Applied Physics*, **49**, 5042 (1978)
364. H. Nagawada, Y. Ishida, *Journal of Polymer Physics*, **11**, 2153 (1973)
365. A. J. Lovinger, *Macromolecules*, **15**, 40 (1982)
366. A. J. Lovinger, *Developments in crystalline polymers-1*, Editor- D. C. Basset, Applied Science Publishers, London, 1982
367. A. Linares, J. L. Costa, *European Polymer Journal*, **33**, 467 (1997)
368. A. J. Lovinger, T. T. Wang, *Polymer*, **20**, 725 (1979)
369. V. J. McBrierty, D. C. Douglaas, T. A. Weber, *Journal of Polymer Science Part B: Polymer Physics*, **14**,1271 (1976)
370. Y. Ishida, M. Wattanabe, K. Yamafugi, *Kolloid. Z.*, **58**, 200, (1964)
371. Z. Liu, P. Marechal, R. Jerome, *Polymer*, **38**, 4925 (1997)
372. W. G. Hu, C. Boeffel, K. Schmidt-Rohr, *Macromolecules*, **32**, 11611 (1999)
373. J. F. Mano, J. L. Lopes, R. A. Silva, W. Brostow, *Polymer*, **44**, 4293 (2003)
374. R. H. Boyd, *Polymer*, **26**, 323 (1985) and R. H. Boyd, *Polymer*, **26**,1123 (1985)
375. S. Castagnet, J. L. Gacougnolle, P. Dang, *Materials Science and Engineering*, **A276**, 152 (2000)
376. G. Laroche, C. P. Lafrance R. E. Prud'homme, R. Guidoin, *Journal of Biomedical Materials Research*, **39**, 184 (1998)

377. N. G. McCrum, B. E. Read, G. Williams, Anelastic and dielectric effects in Polymeric solids, pp no 449, John Wiley and sons, 1967.
378. B. Hahn, J. Wendroff, D. Y. Yoon, *Macromolecules*, **18**,718 (1985)
379. R. Gregorio, F. Malmonge, G. F. Leal Ferreira, W. N. Santos, L. H. C. Mattoso, *Journal Of applied Polymer Science*, **87**,752 (2003)
380. J. Mijovic, J. W. Sy, T. K. Kwei, *Macromolecules*, **30**,3042 (1997)
381. J. W. Sy, J. Mijovic, *Macromolecules*, **33**, 933 (2000)
382. J. F. Mano, *Macromolecules*, **34**, 8825 (2001)
383. S. L. Mendez, M. V. Moriera, J. F. Mano, V. H. Schmidt, G. Bohannan, *Ferroelectrics*, **15**, 273, (2002)
384. R. Gregorio Jr., E. M. Ueno, *Journal Of Material Science*, **34**, 4489 (1999)
385. M.G. Broadhurst G. T. Davis, *Ferroelectrics*, **32**, 177 (1981)
386. A. J. Lovinger, *Ferroelectrics*, **40**, 227 (1983)
387. J. Strathdee, W. H. Robinson, *Journal Applied Physics*, **53**, 605(1982)
388. M. A. Marcus, *Ferroelectrics*, **40**, 29 (1982)
389. W. T. Chen, E. Sacher, D. H. Strope, J. J. Woods, *Journal of Macromolecular Science Part B: Physics*, **B21**, 397 (1982)
390. R. Timmermen, W. J. Greyson, *Journal of American Physical Society*, **6**, 456 (1962)
391. D. J. Lin, C. L. Chang, F. M. Huang, L. P. Cheng, *Polymer*, **44**, 413 (2003)
392. S. Yano, N. Okuba, K. Takashi, *Macromolecular Symposia*, **108**, 279 (1996)
393. J. W. Kim, W. J. Cho, C. S. Ha, *Journal of Polymer Science: Part B: Polymer Physics*, **40**, 19 (2002)
394. A. K. Tripathi, R. Sekar, P. K. C. Pillai, *Materials Letters*, **9**, 24, (1989)
395. C. Muralidharan, P. K. C. Pillai, *Journal of Materials Science*, **23**, 410 (1988)
396. R. Gregorio Jr., M. Cestari, F. E. Bernardino, *Journal of Materials Science*, **31**, 2925-2930 (1996)
397. T. Yamada, T. Ueda, T. Kitayama, *Journal Of Applied Physics*, **53**, 4328 (1982)
398. A. Tawansi, A. H. Oraby, E. M. Oraby, E. M. Abdelrazek, M. Abdelaziz, *Polymer Testing*, **18**, 569 (1999)

399. A. Tawansi, A. H. Oraby, S. I. Baadr, I. S. Elahmawi, *Polymer International*, **53**, 370 (2004)
400. A. Tawansi, A. H. Oraby, E. Ahmed, E. M. Abdelrazek, M. Abdelaziz, *Journal Of Applied Polymer Science*, **70**, 1759 (1998)
401. A. Tawansi, M. I. Ayad, E. M. Abdel-razek, *Journal Of Applied Polymer Science*, **72**, 771 (1999)
402. Z. M. Dang, Y. H. Lin, C. W. Nan, *Advanced Material*, **15**, 1625 (2003)
403. B. Wang, L. Gu, *Materials Letters*, **57**, 361 (2002)
404. C. Del Río M. C. Ojeda, J. L. Acosta, M. J. Escudero, E. Hontañón, L. Daza, *Journal of Applied Polymer Science*, **83**, 2817 (2002)
405. G. Wu, C. Zhang, T. Miura, S. Asai, M. Sumita, *Journal of Applied Polymer Science*, **80**, 1063 (2001)
406. N. Levi, R. Czerw, S. Xing, P. Iyer, D. L. Carroll, *Nano Letters*, **4**, 1267 (2004)
407. Z. M. Dang, L. Z. Fan, Y. Shen, C. W. Nan, *Material Science and Engineering: B*, **103**, 140 (2003)
408. C. Seoul, Y. T. Kim, C. K. Baek, *Journal of Polymer Science: Part B: Polymer Physics*, **41**, 1572 (2003)

Chapter 2
Experimental Details,
Characterization
Techniques and Analysis

Chapter 2

2 Experimental Details, Characterization Techniques and Analysis

This chapter presents the details of materials used preparation methods of the composites and techniques used for characterization.

Two grades of PVDF and three types of clays were used for preparation of nanocomposites. The nanocomposites were prepared using melt intercalation technique. The extent of intercalation depends upon the interaction between the polymer (molecular weight and grade) and organophilic clay. Materials

2.1.1 PVDF Grade SOLEF 1008

PVDF grade SOLEF 1008 is low viscosity, all purpose injection-molding grade. It has excellent chemical resistance to most aggressive substances and solvents, excellent mechanical strength and toughness, high abrasion resistance, excellent aging resistance, resistance to UV and nuclear radiation, excellent intrinsic fire resistance, resistance to weathering, low permeability to most gases and liquids, and can easily be melt-processed by standard methods of molding and extrusion.

The properties of SOLEF 1008 as per company data sheet are as follows.

The average molecular weight is reported to be $\overline{M}_w = 119813$, $\overline{M}_n = 53909$.

MFI at 230°C/5Kg is 24g /10 min.

Physical Properties of PVDF Grade SOLEF 1008

Density: 1.78 g/cc,

Water Absorption: Max 0.04%

Melt flow: 24 g/10 min/5Kg at 230 °C

Crystallinity: 48.9%

Coefficient of Thermal expansion (CTE), (linear 20°C): 120-140µm/m-°C

Melting point: 174 °C

Crystallization temperature: 140 °C

2.1.2 PVDF Grade HYLAR 460

PVDF grade HYLAR 460 has characteristic stability of fluoropolymers combined with a unique polarity that influences its solubility and electrical properties. It can be processed using standard molding and extrusion. It is also used

in solution-applied coatings. It has specific application in high-speed monofilament extrusion.

The properties of HYLAR 460 as per company data sheet are as follows.

HYLAR 460 has broad molecular weight distribution, high branching, excellent cross linkability and has 40-60% insoluble gel fraction. MFI at 230 °C/5Kg is 0.35-4.0 g /10 min.

Physical Properties of PVDF Grade HYLAR 460

Density: 1.75-1.77 g/cc,

Water Absorption: Max 0.04%

Crystallinity: 36%

Coefficient of Thermal expansion (CTE) (linear 20°C): 80-140 $\mu\text{m}/\text{m}\cdot^{\circ}\text{C}$

Melting point: 160 °C

2.1.3 Organically Modified Clays

The clays used for this study are organically modified clays Cloisite 6A, and 20A and unmodified clay Na^+ generously supplied by Southern Clay Products (United States). The details of these organic modified clays are summarized in the table 2.1.1.

Table 2.1.1: Physical properties of the commercial clays used

Clay Trade name	Organic Modifier	Modifier Conc. (meq/100g)	d spacing (nm)		% Weight loss		Specific Gravity (g/cc)
			Initial	After annealing at 200°C for 10 min*	At ignition	At 200°C	
Cloisite Na ⁺	None	None	1.17		7	1.8	2.86
Cloisite 6A	$\begin{array}{c} \text{CH}_3 \\ \\ \text{H}_3\text{C}-\text{N}^+-\text{HT} \\ \\ \text{HT} \\ \text{Anion- Cl}^- \end{array}$	140	3.32	3.37	48	1	1.71
Cloisite 20A	$\begin{array}{c} \text{CH}_3 \\ \\ \text{H}_3\text{C}-\text{N}^+-\text{HT} \\ \\ \text{HT} \\ \text{Anion- Cl}^- \end{array}$	95	2.42	2.44	38	1	1.77

* denotes experimental data

HT represents Hydrogenated tallow (~65% C18, ~30% C16, ~5% C14).

The clay samples were used as received with no further purification steps.

Thermal stability of the samples was ascertained by observing the d_{001} spacing after annealing the samples at 200 °C for 5 min and observing percentage weight loss at 200 °C from thermo gravimetric analysis of the clays. This data is shown in the table above. This was essential to ensure that the clay gallery does not collapse during the compounding step due to decomposition of organic content.

The clay samples were dried at 60 °C overnight before compounding.

2.2 Melt Compounding Techniques

2.2.1 Batch Mixer

The nanocomposites of PVDF were prepared using a Brabender Plasticorder batch mixer (PLE 330) (Brabender Measurements and Control, Germany) on a small scale. The device is made up of a heated mixing head (WEH 50) containing a pair of sigma shaped roller blades, which are driven by dynamometer at controlled speed. By using variable potentiometers the speed of the rollers can be adjusted and hence shear rate. The rotors are counter rotating, heated by electric heaters with temperature controller.

Volume of mixing chamber: 60 cc

Maximum Temperature: 350 °C

Sample preparation conditions

PVDF (Solef 1008)/Clay (Na⁺, 20A, 6A) with varying clay percentages (1.5, 3, 5, 7) were prepared using Batch mixer.

Temperature- 200 °C

Time of mixing- 5 minutes

RPM- 60

Initially the nanocomposites were prepared using a batch mixer and scaled up using twin-screw extruder.

2.2.2 Twin Screw Extruder

The twin-screw extruder used was Berstoff ZE 25 with corotating and intermeshing screws, having 25 mm diameter and L/D ratio of 41.5. Maximum RPM that can be obtained is 550. There are eight temperature zones in this extruder. Temperature settings of the zones are shown in the table 2.2.1.

PVDF (Solef 1008 and Hylar 460) and 20A nanocomposites are prepared by extrusion. The compositions prepared contain 1.5, 3, 5, 7, and 10% of modified clay.

Table 2.2.1: Extrusion conditions used

Heating zones	1	2	3	4	5	6	7	8	Die
Temperature (°C)	150	160	170	180	185	190	195	200	210

RPM-100

2.3 Sample Preparation Techniques

2.3.1 Compression Molding

Carver press model F-15181 was used to prepare thin films of polymer and base materials. An appropriate quantity of the material was taken and heated above the melt temperature between metal sheets. Nominal pressure was applied to get films of required thickness. Platens were then cooled to room temperature by water circulation.

XRD and DMA were carried out from the compression-molded films. Solef 1008 based films were compression molded at 200 °C and Hylar 460 based films were formed at 210 °C.

2.3.2 Injection Molding

The specimens for mechanical testing were prepared using injection molding machine. Injection molding was carried out in an Arburg All Rounder 220-90-350 machine. Its specifications are as follows.

Maximum shot capacity: 60 grams

Maximum injection pressure: 1905 bar

Maximum mould clamping force: 350 KN

Maximum screw speed: 200 rpm

Screw diameter: 25 mm

L/D: 33

Temperature zones: feed zone, transition zone, metering zone, and nozzle zone

Temperature and pressure setting of the zones for injection molding are as shown in the table 2.3.1.

Table 2.3.1: Temperature settings of the different zones in Injection molding machine

Heating zones	1	2	3	4
Temperature (°C)	200	210	215	220

Pressures applied to the transition zone, metering zone and nozzle zone are 93, 93, and 90 bars respectively.

2.4 Characterization Techniques

2.4.1 X-ray Diffraction (XRD)

Crystal structure can be studied through diffraction pattern of waves that interact with atoms and that have wavelength comparable with interatomic spacing such as photons, neutrons, and electrons. The diffraction depends on the crystal structure and on the wavelength. When the wavelength of the radiation is comparable with or smaller than the lattice constant, the diffracted beams are observed.

The energy of an X-ray photon is related to its wavelength λ by $\epsilon = hv = hc/\lambda$, where h is Planck's constant ($= 6.62 \times 10^{-34}$ J-s). Crystal studies require photon energies in the 10 to 50 KeV range. X-rays are generated both by the deceleration of electrons in metal targets and by the excitation of the core electrons in the atoms of the target. The first process gives a broad continuous spectrum; the second gives sharp lines. A copper target bombarded by electrons has a strong line $Cu K_{\alpha}$ at 0.15418 nm. Copper makes a good target: it is an excellent heat conductor with a high melting point. Nuclei, because of their heavy mass, do not scatter X-rays effectively.

X-ray diffraction (XRD) is a non-destructive analytical technique for identification and quantitative determination of long-range order in various crystalline compounds.

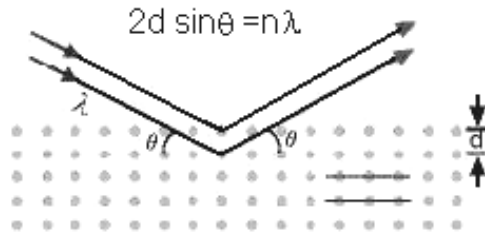


Figure 2.4.1: Bragg's law of X-ray diffraction

Bragg presented a simple explanation of the diffracted beams from a crystal⁽¹⁾. The diffracted beams are found when the reflections from parallel planes of the atoms interfere constructively. Consider parallel lattice planes spaced at a distance d apart. The radiation is incident in the plane of the crystal lattice. The path difference for rays reflected from adjacent planes is $2d \sin \theta$, where θ is measured from the plane. Constructive interference of the irradiation from successive planes occurs when path difference is an integral multiple (n) of wavelength λ . Therefore,

$$2d \sin \theta = n\lambda \quad (2.1)$$

This is the Bragg's law.

Although the reflection from each plane is specular, for only certain value of θ , the reflection from all parallel planes add up in phase to give strong reflected beam. Each plane reflects 10^{-3} to 10^{-5} of incident radiation. The Bragg's law is a consequence of periodicity of the lattice. It requires that θ and λ to be matched. To achieve this it is necessary to scan either wavelength or angle.

X-rays are scattered by contrasting regions of electron density, which originate from voids, grain boundaries, density fluctuations, difference in electron density between crystalline and amorphous regions, etc., in materials. The intensity of X-rays is proportional to the magnitude of contrast and number of scattering centers. The shape of scattering intensity profile is related to the shape of scattering units and their packaging via Fourier transformation.

X-ray powder diffraction in the reflection mode (Bragg Brentano Parafocusing geometry)^(2,3) as shown in the figure 2.4.2, is used to characterize the structure of polymer layered silicate nanocomposites. The powder diffraction

techniques are based on the established procedures developed for identification and structural characterization of layered minerals⁽⁴⁾.

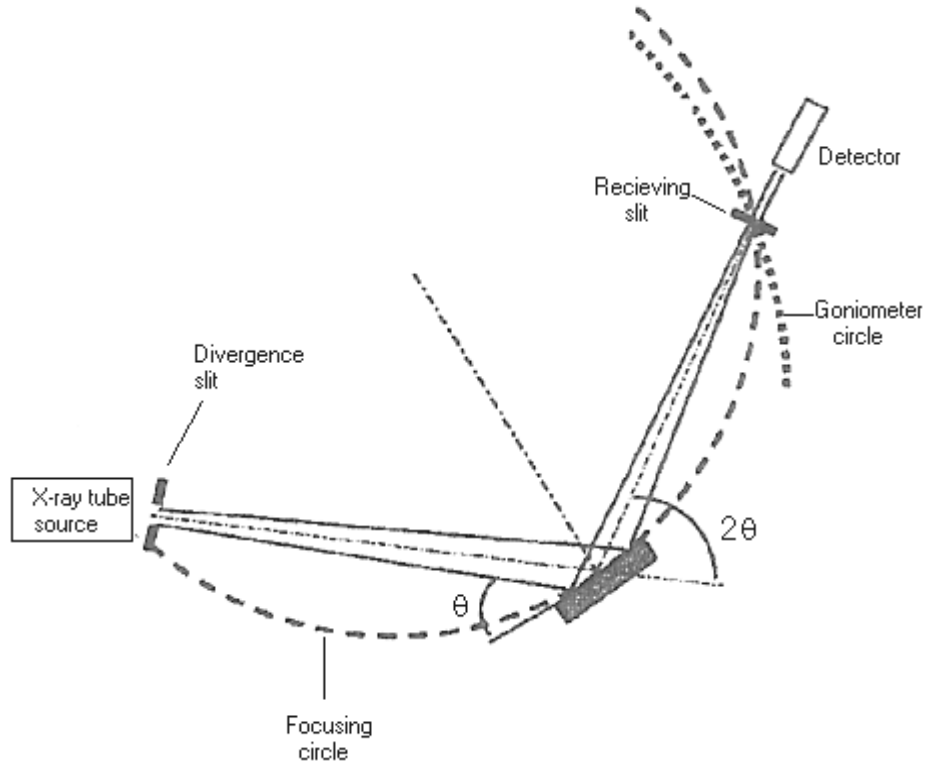


Figure 2.4.2: Bragg Brentano Para focusing geometry of XRD in reflection in mode

The structure of polymer and nanocomposites were evaluated by performing wide-angle X-ray Diffraction (WAXD) experiments using a Rigaku model Dmax 2500 X-ray diffractometer. The system consisted of a rotating anode X-ray generator operated at 40 kV and 150 mA and a wide-angle goniometer.

2.4.2 Transmission Electron Microscope (TEM)

TEM gives a direct evidence of the structure and a definitive description of the spatial correlation. TEM images were observed with a JEOL (JEM 1200 EX) apparatus.

The basic components (figure 2.4.3) of a TEM consist of a stream of electrons produced from a filament anode and accelerated towards the specimen using a positive electrical potential. This stream is confined and focused using two

condenser magnetic lenses (electromagnets) into a thin, monochromatic beam. The beam is focused and impinged on the selected area of the sample by a magnetic lens, alignment coils, and objective magnetic lenses. The energetic electrons then interact with the irradiated sample. This is detected and magnified by the intermediate lenses and transformed into a photographic image.

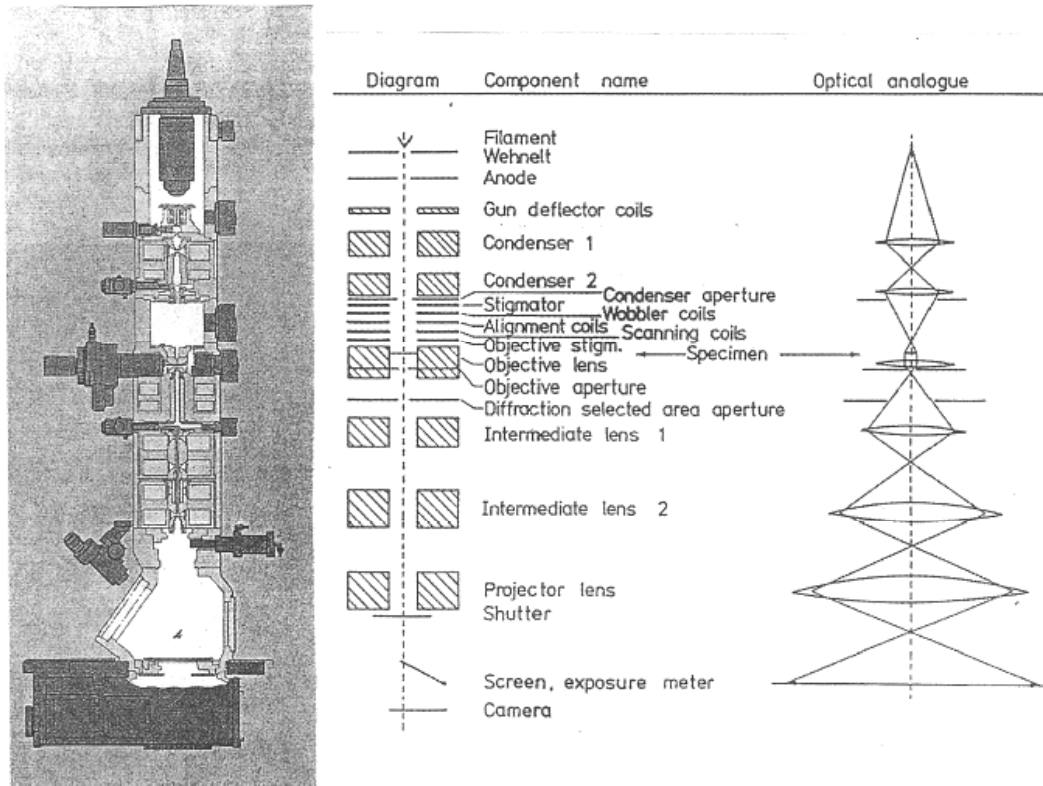


Figure 2.4.3: Basic components of a Transmission Electron Microscope

Sample preparation

TEM specimen needs to be sufficiently thin of the order of 100 nm or less. In this thin area, only a few electrons are scattered and more than 90% of the incident beam is undeviated. Layered silicates have a higher density than the polymer. Therefore, the silicate layer appears darker than the polymer. Regions of the specimen, which are thicker, or of higher density will scatter the electron beam more strongly and will appear darker in the image. If the specimen is too thick, the number of electrons transmitted reduces and this makes the polymer appear darker and hence reduces the contrast. This is the phenomenon of mass thickness contrast. Hence, the specimen should be cut very thin of the order of 100 nm or lesser.

The samples for TEM are prepared using a Leica Ultracut UCT microtome. Properly trimmed samples (of trapezoid shape having its lateral dimensions closer to 1mm) are placed in an arm, which is attached to a motor controlled hand wheel. As the arm moves vertically past the knife (glass or diamond), the sample is cut in the required thickness. These cut sections are collected on water surface, of a boat attached to the knife-edge. The cut sections are directly transferred to the grids and dried properly before being transferred to the TEM experimental setup.

2.4.3 Optical Microscopy

Leitz Laborlux 12 Pol S Polarizing light microscope, equipped with photographic camera having automatic exposure unit is used for studying the spherulitic morphology. Thin samples are prepared by melting polymer samples between a glass slide and a cover slip. The molten polymer film is then transferred to the hot stage held at constant crystallizing temperature. The spherulitic morphology was studied using cross polarizers.

The developing spherulites are highly birefringent. A characteristic feature of spherulitic structure is the presence of fibrous units. Fibrillar development is a fundamental process in spherulitic growth. The fibrils extend radially outwards from the central nuclei. In rapidly grown structures, the fibrils are usually of sub-microscopic dimensions, and so cannot be resolved. During slow growth, spherulitic structure often coarsens. As the spherulite expands, the fibrillar structure branches and fills the space. The angle between the branches is small and is not related to crystallographic axes. The branching fibrils as they develop, often twist and in rapidly growing structures, this twisting takes place co-operatively, to produce periodic variation in refractive index, which gives rise to complicated ring structures. In well-ordered growths, the angle between branches must necessarily be very small. A spherulite probably develops from a single crystal in the early stages of growth and becomes polycrystalline as branching sets in.

Optical determination of the orientation of the chain molecules in the spherulites shows that, the long axis of the chains are oriented at right angles to the radii i.e. across the radiating fibrils. The refractive index along the chain is different from the average value across it. The tangential orientation of chains is responsible

for extinction of light in opposite quadrants, when viewed between crossed polars. This gives rise to characteristic Maltese cross⁽⁵⁾.

2.4.4 Differential Scanning Calorimeter (DSC)

Differential scanning calorimeter is a technique for studying the thermal behaviour of a material as a function temperature as they go through physical or chemical changes with absorption or evolution of heat. This method is used to study thermal processes as a function of temperature (non-isothermal melting and crystallization) and constant temperature (isothermal crystallization). Two different types of DSC instruments are generally used: heat flux and power compensation. In a heat flux type of DSC, the sample, and reference are heated in a common block and the differential temperature (ΔT) between the two cells. In a power compensation type of DSC, the sample and reference cell has individual heaters is measured. ΔW , the difference between the power output of the sample and reference cells in order to maintain the same-programmed temperature in each cell is measured. This difference corresponds to heat capacity of the sample at that temperature.

The instrument used is Perkin Elmer DSC-2 (power compensation type of DSC) equipped with Thermal Analysis Data station software. The sample holder assembly contains two platinum alloy cups, which are the sample holders and have individual heater and sensor. A high gain, closed-loop electronic system provides differential electrical power to the heaters to precisely compensate for temperature fluctuation. The differential power required for maintaining the balance condition is equivalent to the rate of energy absorption or evolution of the sample.

The operating temperature range is 50°C to 725 °C. The heating or cooling rates used are 5, 10, 20, 40, 160 °C/ min. Temperature accuracy is approximately ± 1 °C. The instrument is calibrated for temperature and energy scales using Indium, Tin, Lead, and Zinc as standards. A weighed amount of sample is crimped in an aluminium sample holder with cover and is directly placed in the sample holder⁽⁶⁾.

2.4.4.1 Non-isothermal Experiments

PVDF and PVDF/Clay nanocomposite samples were studied in the temperature range of 50 °C to 200 °C at a heating rate of 10 °C/min. Nitrogen was

used as purging gas in order to maintain an inert atmosphere. The thermal parameters such as melting peak temperature (T_m), heat of fusion (ΔH_f), crystallization peak temperature (T_c) and heat of Crystallization (ΔH_c) are measured as shown in the figure 2.4.4.

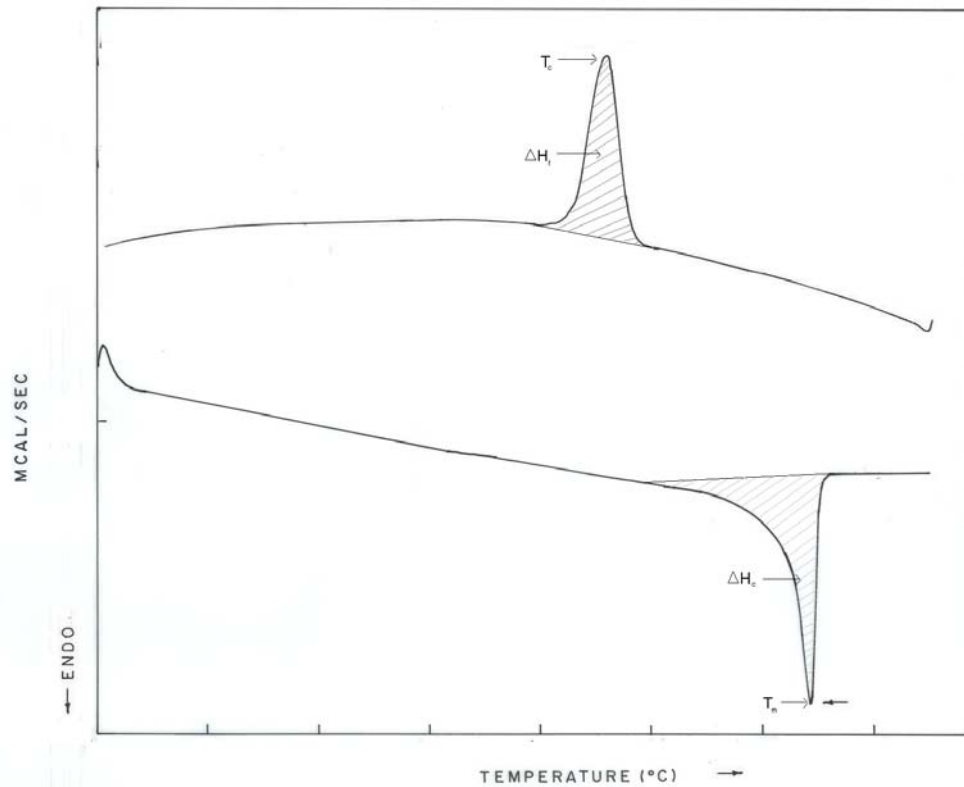


Figure 2.4.4: Melting and Non-isothermal Crystallization

2.4.4.2 Isothermal Crystallization Experiments

In isothermal crystallization, the sample is heated at a heating rate of $40^{\circ}\text{C}/\text{min}$ to the desired melt temperature (T_{melt} , here 200°C) sufficiently above the melting point of the polymer and is held at melt temperature for 2 min, to destroy residual nuclei. Then it is cooled at a rate of $160^{\circ}\text{C}/\text{min}$ to a predetermined crystallization temperature (T_c) and the crystallization exotherm is recorded as a function of time.

A typical isothermal crystallization exotherm is shown in figure. The curve shows induction time (t_i), total crystallization time (t_c). Induction time (t_i) is defined, as the time required initiating the isothermal crystallization process. Total

crystallization time (t_c) is defined as the time required for the completion of the isothermal crystallization process.

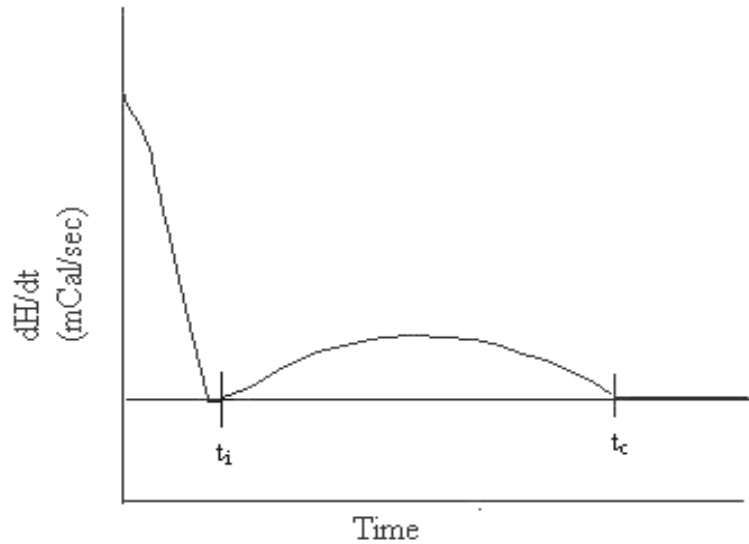


Figure 2.4.5: Isothermal Crystallization

Isothermal crystallization was analyzed using the Avrami equation ⁽⁷⁾

$$X_t = 1 - \exp(-kt^n) \quad (2.2)$$

where ' X_t ' is the volume fraction of crystallized material at time ' t ', ' k ' is the rate constant and ' n ' is the Avrami exponent. From the experimental data the crystallization half time, ' $t_{1/2}$ ', which is the time required for crystallizing 50% of the material and ' k ' can be calculated. The crystallization half time, ' $t_{1/2}$ ' and induction time ' t_i ' are characteristic parameters of the crystallization process and represents the crystallization and nucleation process. Depending on the mechanism of nucleation (homogeneous or heterogeneous) and type of crystal growth different values of ' n ' are obtained. Avrami exponent ' n ' is a combined function of number of dimensions in which growth unit takes place and the order of time dependence of the nucleation process. The value of $n=1$ corresponds to one-dimensional growth (rods). $n=2$ and 3 corresponds to two-dimensional disc and three-dimensional spheres respectively for instantaneous nuclei. When the growth is sporadic, $n=2$, 3 and 4 represents one-dimensional, two-dimensional and three-dimensional growth, respectively. However, integer values of Avrami exponent are seldom obtained due to various

simplifications used in the original derivation. Hence, the precise interpretation of the results is difficult⁽⁷⁾.

2.4.5 Fourier Transform Infrared Analysis (FTIR)

Infra red radiation is absorbed by molecule when its vibrational motion produces a change in dipole moment. The IR spectra of the samples in the present investigation are recorded using Perkin Elmer FTIR model 1605, to identify the characteristic bands in the samples. Compression molded thin films of sample are used for this purpose.

2.4.6 Mechanical Properties

The study of mechanical properties of semicrystalline polymers is one of the important areas in the field of applied polymer science. The measurement of mechanical properties is concerned with load-deformation or stress-strain relationship. Force in different modes may be applied as tension, compression, shear, torsion, or bending. Tensile properties are fundamental to the study of mechanical properties of material. The tensile dog bone shaped specimen for tensile testing is prepared according to the ASTM D638 (Type I) standards. The sample edges are clamped to the two clamps, one fixed and the other movable. The tensile testing of injection molded samples was performed in Instron Universal Testing Machine model 4204 at a crosshead speed of 50 mm/min and using a load cell of 10 KN.

2.4.6.1 Stress-Strain Properties

Stress (σ) is defined as the force applied (F) per unit area (A).

$$\sigma = \frac{F}{A} \quad (2.3)$$

Unit of stress is N/m² or Pa. The applied stress causes deformation measured by strain (ϵ), which is deformation per unit dimension.

For tensile experiment

$$\epsilon = \Delta l / l \quad (2.4)$$

where Δl is the change in length and l is the original length. Strain is dimensionless and is often given in % for convenience. For a perfectly elastic body obeying Hooke's law, elastic modulus is defined as

$$E = \varepsilon / \sigma \quad (2.5)$$

Other types of mechanical moduli are defined depending on the how the specimen is deformed.

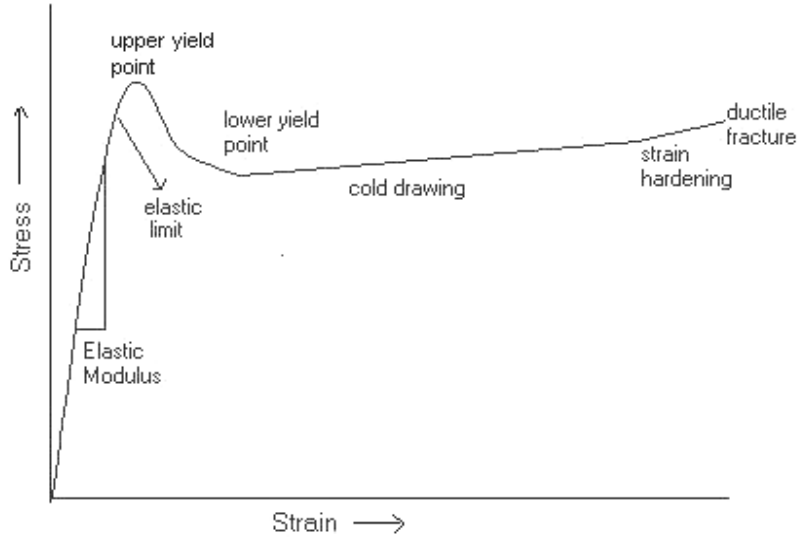


Figure 2.4.6: Stress-strain curve

The typical stress strain curve of semi-crystalline polymer is shown in figure 2.4.6. The semicrystalline material deforms reversibly upto a certain amount, called as the elastic limit, and then yield. At the yield point the material begins to neck. It is other wise called as the upper yield point. The following region of low slope is associated with the process of cold drawing, where the neck propagates along the gauge length because of flow. Finally the material begins to harden and then fails. Upto the elastic limit, the material will return to its former shape and size when the force is removed. Beyond this point deformation is irreversible i.e. creep sets in. A brittle material deforms reversibly to a small amount and then fractures⁽⁸⁾.

2.4.7 Impact Properties

Impact strength is the resistance to break under high velocity impact conditions. The polymeric materials are subjected to an impulse load of very short duration of the order of micro- or milli-seconds. The notch is a stress concentrator and the fracture occurs there. The amount of energy required to initiate a crack is greater than that needed to propagate it. In un-notched specimens, the impact

resistance involves measurement of both the energies required to initiate a crack and that needed to propagate it.

Izod impact testing is extensively used to determine the impact resistance. In this a falling weight pendulum strikes the rectangular bar specimen. The specimen is clamped in a vertical position at the lower end of the base of the test stand.

The impact properties are carried out using Ceast impact testing Machine, Ceast model 6545/000, Torino, Italy as per ASTM D256 at room temperature.

2.4.8 Dynamic Mechanical Analysis (DMA)

The dynamic mechanical properties of the samples were studied using Rheometrics dynamic mechanical analyzer, model DMTA IIIIE. The samples were analyzed in the tensile mode. For the constant frequency, oscillatory test, temperature sweep was carried out from -100 to 150 °C and the sample was heated at a rate of 5 °C/min. The frequency was 10 rad/s and the strain was fixed suitably in the linear region, by carrying out some strain sweep tests and noting that the force lies between the transducer limits.

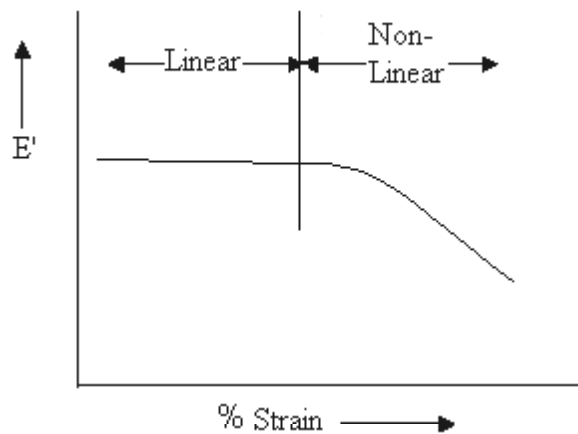


Figure 2.4.7: Linear and Non-linear region of testing

Dynamic testing of materials provides invaluable insight into the structural changes, long-term functional performance for quality, processability and molecular properties of polymers. Application domain of DMA covers a wide range of

materials including elastomers, thermoplastics, thermosets, adhesives, composites, gels, wood, paper, ceramics, metals, alloys, etc. The measurement of dynamic mechanical properties can be used for establishing relationships between the dynamic properties and different physical/chemical structural parameters such as crystallinity, orientation, molecular weight, cross-linking etc. It can also be used to find the effect of external variables such as temperature, deformation, and humidity on the response of the polymer.

The principle of dynamic mechanical test method is to impart a small sinusoidal mechanical strain on to a solid or a viscoelastic liquid and to resolve the stress into real and imaginary components corresponding to elastic and viscous states ^(9, 10). In visco-elastic studies, the applied force and resulting deformation both vary sinusoidally with time. The strain will also be sinusoidal but will be out of phase with stress. This phase lag results from the time necessary for molecular rearrangements and is associated with the relaxation phenomena. The variation of these components as a function of temperature is used to study the molecular motion in the polymers.

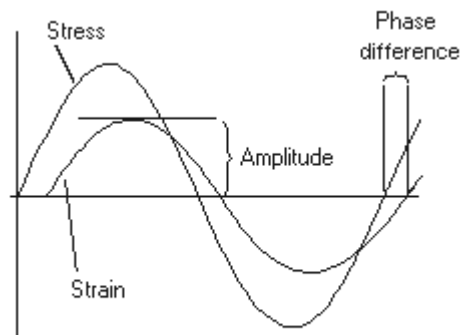


Figure 2.4.8: Principle of dynamic testing

The phase lag (expressed in terms of phase angle δ) results from the time necessary for molecular rearrangement and is associated with relaxation phenomenon.

If the sinusoidal strain is expressed as

$$\varepsilon = \varepsilon_0 \sin(\omega t) \quad (2.6)$$

where ω is the frequency of vibration.

The stress response is given by

$$\sigma = \sigma_0 \sin(\omega t + \delta) = \sigma_0 \sin \omega t \cos \delta + \sigma_0 \cos \omega t \sin \delta \quad (2.7)$$

Thus stress can be considered to consist of two components one in phase with the strain ($\sigma_0 \cos \delta$) and one out of phase with the strain ($\sigma_0 \sin \delta$). The modulus is ratio of the stress and strain, which can be represented by real (in phase) and imaginary (out of phase) component i.e., modulus is a complex quantity.

$$E^* = E' + E'' \quad (2.8)$$

$$E' = \frac{\sigma_0}{\varepsilon_0} \cos \delta \quad (2.9)$$

is the storage modulus as it is related to the storage of energy as potential energy and its release during the cycle. Storage modulus is a measure of stiffness and represents elastic fraction of deformations.

$$E'' = \frac{\sigma_0}{\varepsilon_0} \sin \delta \quad (2.10)$$

is the loss modulus and is associated with the dissipation of energy as heat when the material is deformed. It is associated with the dissipation of energy as heat when material is deformed.

The ratio of loss modulus to storage modulus (E''/E') is equal to the tangent of the phase angle (δ), which is the ratio of energy dissipated per cycle to the maximum potential energy stored during the cycle.

DMA can be used for determination of the glass transition temperature (T_g) of a given material. At T_g , cooperative motions involving long chains segments of molecules occur so that $\tan \delta$ reaches maximum value.

The tests can be conducted by applying oscillations in different ways. The forced oscillation technique is used here.

2.4.9 Coefficient of Thermal Expansion

The coefficient of thermal expansion (linear) is defined as the change in length per unit length of material for a one degree Celsius change in temperature. This can be measured in the tensile mode using DMA.

2.4.10 Creep Studies

Creep test is a powerful tool to study the plastic deformation mechanism from which micro structural processes can be studied. Time dependant degradation in modulus (creep) and strength (creep rupture) is a consequence of viscoelasticity of polymer matrix. In general creep of a polymer is a result of interactions of one or more of the events such as viscoelastic deformation, primary and secondary bond rupture, shear yielding and crazing (which involves chain slippage, void formation and growth). Depending on the polymer and its structure and their interaction with conditions such as temperature, stress, and time, different events will dominate the process.

Static creep experiments were also performed in the DMA in the tensile, stress controlled, transient mode at fixed temperatures and stresses. The sample initial length was kept at 10 mm.

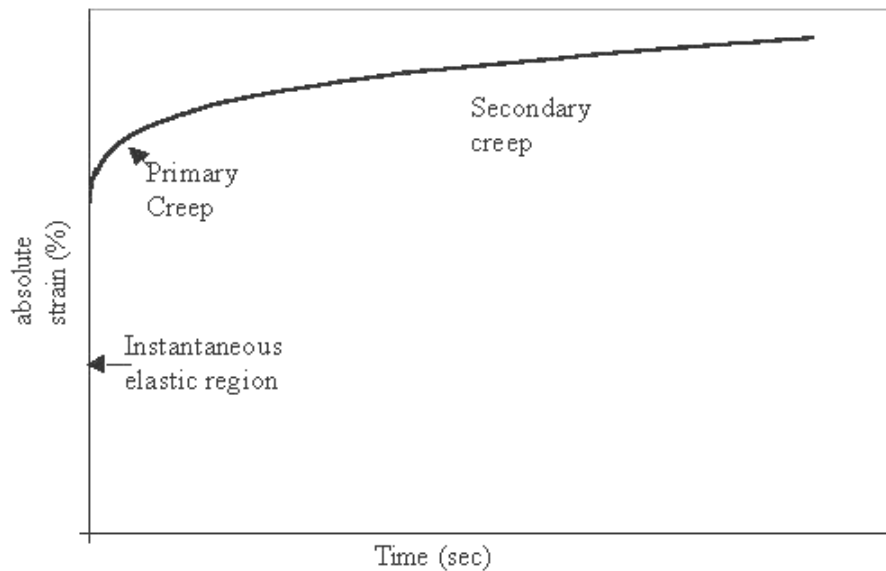


Figure 2.4.9: A Typical Creep Curve

A typical creep curve is shown in the figure 2.4.9. The time versus strain graph shows three specific regions viz., the instantaneous elastic region, primary creep and the secondary creep region. The primary creep region is characterized by

the decreasing strain rate caused by increase in defect density reducing the chain mobility. In the secondary creep region, the strain rate is constant because of chain relaxation and local rearrangements. The tertiary region of the creep not shown in the figure. It occurs at very long periods of testing. Here the creep rate increases very rapidly and finally creep fracture occurs.

2.4.11 Melt Rheology

An oscillatory shear experiment is the most commonly used method for determining the linear viscoelastic properties of polymer melts. In a typical oscillatory shear experiment, a sinusoidally varying small amplitude stress or strain is applied to the sample, and the response, i.e., either sinusoidally varying strain or stress, respectively, is measured as in the case of DMA. A typical frequency response curve is shown in the figure 2.4.10.

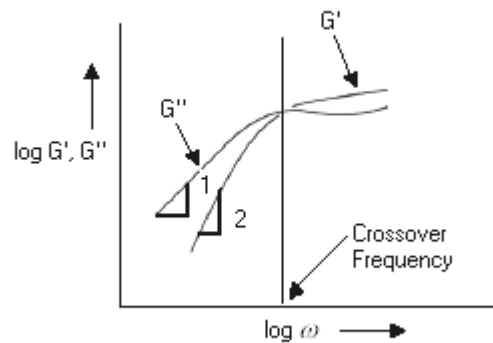


Figure 2.4.10: Frequency response curve of G' and G''

At low frequencies (terminal region), $G'' > G'$ i.e., the behavior is liquid like. The slopes of G' and G'' are 1 and 2 respectively. G' and G'' increase until the crossover frequency is reached. Reciprocal of crossover frequency gives the characteristic relaxation time of the material. After crossover, G' reaches a constant value in the intermediate frequencies called as the plateau modulus. Plateau modulus is independent of the molecular weight and depends only on the chemical nature of the polymer. In this region G'' passes through a minimum. At very high frequencies,

G' and G'' increases. At such higher frequencies or small time scales, response will be only due to the small parts of the polymer chains (not shown in figure).

The viscoelastic material functions are strong functions of temperature, and frequency. No single experiment can cover the entire span of frequencies. Hence the principle of time-temperature superposition is applied such that a change in the temperature shifts the viscoelastic functions along the time scales. For a time dependant process of linear viscoelastic materials, time and temperature have equivalent effects on the rheological properties of a given sample. E.g., lowering the temperature of a polymer may proportionally increase the time over which dynamical responses can occur. Similarly increasing the temperature reduces the time required for the response. Changing the temperature is analogous to rescaling the time or frequency axis. A temperature change has the effect of shifting data along the time or frequency axis, while maintaining the shape of the functions and values. The shift factor can be calculated by WLF or Arrhenius fitting ^(11,12) using RSI Orchestrator software.

Dynamic oscillatory frequency sweeps were carried out in Rheometric Scientific ARES rheometer in the frequency range of 0.05 to 100 rad/sec at temperatures 210- 240 °C. Parallel plate geometry of 25 mm diameter is used for this purpose. The specimen thickness of 1 mm was maintained approximately. The strain sweep experiment was carried out to find the region of linear response. The strain was fixed at 2% ensuring that the measurements are carried out in linear region.

2.4.12 Dielectric Analysis (DEA)

Dielectric relaxation spectroscopy is an extremely effective technique for characterizing in detail the molecular dynamics over large range of time scales ⁽¹⁰⁾. The technique is sensitive to orientation motions of permanent dipoles and to translational contributions of ions. Dielectric property changes with frequency, temperature, orientation, pressure, and molecular structure of the material. A material is said to be dielectric if it has the ability to store energy when an external field is applied. Dielectric spectroscopy can provide information about the segmental mobility of a polymer by probing the dielectric properties. Dielectric spectroscopy

offers the possibility of characterizing the glass, amorphous and crystalline states as well as phase changes of the polymer through continuous quantitative measurements of dielectric properties.

If a dc voltage source is placed across a parallel plate capacitor, more charge is stored when a dielectric material occupies the separation between the plates. The dielectric material increases the storage capacity of the capacitor by neutralizing charges at the electrode, which ordinarily will contribute to the external field. AC voltage source placed across a capacitor will result in charging current and loss current. Permittivity describes the interaction of a material with electric fields.

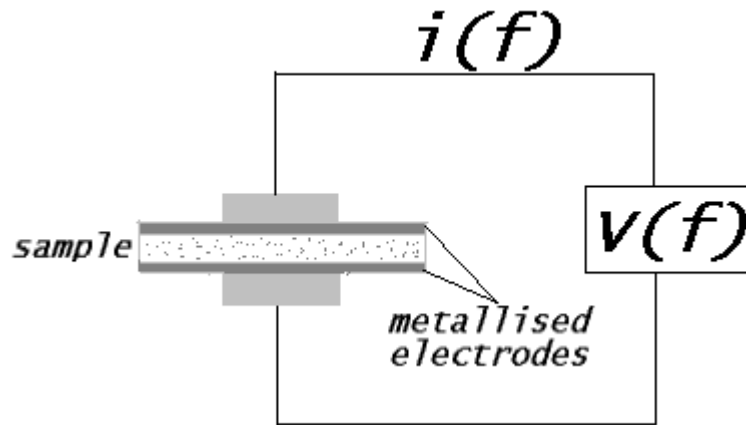


Figure 2.4.11: Sample holder for dielectric Testing

The complex dielectric properties, the loss factor (ϵ''), and the relative permittivity (ϵ'), are determined by performing several isothermal scans as a function of frequency. An alternating current ($V_{\text{rms}}=0.005\text{-}1.1$ volts) external field is applied across the sample in a capacitor plate configuration. The applied electric field interacts with the electric dipole moment of the sample. The polarization of the sample is related to the applied electric field by the equation

$$\vec{P} = \epsilon_0 \chi_e \vec{E} \quad (2.11)$$

where \vec{P} and \vec{E} are the Polarization vector and Electric Field vector and ϵ_0 corresponds to the permittivity of free space. χ_e is defined as the dielectric susceptibility and is given as

$$\chi_e = \varepsilon - 1 \quad (2.12)$$

where ε is the dielectric constant of the material. This total polarization consisted upon by four different mechanisms, viz, electronic, atomic, orientation or dipolar and ionic polarization. Each dielectric mechanism effect has a characteristic relaxation frequency. As the frequency becomes larger, the slower mechanism drops off. This in turn leaves only the faster mechanisms to contribute to the dielectric storage. The dielectric loss factor will correspondingly peak at each critical frequency.

Dielectric properties of the samples in the film phase were measured using the Novo Control Alpha T Analyzer equipped with temperature controller and Win Imp and Win Fit software. The samples were scanned between frequencies 0.01Hz and 10MHz at room temperature. Bias voltage applied across the sample is 0.1V. The electrode diameter was 25 mm and thickness of the sample is measured and used while calculating the dielectric constant.

References

1. C. Kittel, Introduction to solid state Physics, John Wiley and sons, NewYork, 1976
2. D. L. Bish, J. E. Post, Modern Powder Diffraction: Reviews in Mineralogy 20 Edition, Mineralogical Society of America: Washington DC, 1989
3. H. P. Klugg, L. E. Alexander, X-ray diffraction procedures; John Wiley & Sons: U.S.A, 1974.
4. G. W. Brindley, G. Brown, Crystal structures of clay minerals and their X-ray identification; Mineralogical Society Monograph number 5, 1984
5. A. Sharples, Introduction to polymer crystallization, Edward Arnold Publishers Limited, London, 1966
6. Perkin Elmer DSC2- Operating manual
7. M. Avrami, Journal of Chemical Physics, 8, 212 (1940)
8. J. Schultz, Polymer Material Science, Prentice-hall, Inc, New Jersey, 1974
9. G. C. Ives, J. A. Mead, M. M. Riley, Hand Book of Plastics Test Methods, Iliffe Book Limited, London, 1971
10. N.G. Mcrum, Anelastic and Dielectric properties of Solids, John Wiley & Sons: U.S.A, 1967
11. Barnes, H. A.; Hutton, J. F.; Walters, K. *An Introduction to Rheology*; Elsevier Publications, U. K., 1989
12. Macosko, C. W. *Rheology principles Measurements, and Applications*; Wiley-VCH Inc., New York, 1994

Chapter 3
Melt intercalated PVDF
(SOLEF 1008)/Clay
Nanocomposites

Chapter 3

3 Melt intercalated PVDF (SOLEF 1008)/Clay Nanocomposites

3.1 Introduction

This chapter presents the results of melt intercalation of PVDF in organically modified clay. Dimethyl dihydrogenated tallow quaternary ammonium chloride treated clay was used for the purpose. Details of the Cloisite 6A clay and PVDF (SOLEF 1008) used in this study are discussed in chapter 2. Melt compounding of PVDF/6A composites is carried out using Brabender Plasticorder batch mixer at 200 °C and 60 rpm for 5 min. Four compositions containing 1.5, 3, 5 and 7% (wt/wt) of clay are prepared. The sample codes and compositions are presented in table 3.1.1.

Table 3.1.1: Sample codes and compositions of PVDF/6A nanocomposites

Weight Percentage of 6A	Sample code
0	P
1.5	PNC1.5
3	PNC3
5	PNC5
7	PNC7

3.2 Results and Discussion

3.2.1 Structure of Nanocomposites

3.2.1.1 X-ray Diffraction (XRD)

Figure 3.2.1 compares the XRD patterns of the PVDF/6A nanocomposites. The clay exhibits three well-defined peaks at 3.3, 1.8 and 1.1 nm corresponding to d_{001} , d_{002} and d_{003} planes. In the case of composites with 6A, as can be seen, the d_{002} peak observed at 1.8 nm for pristine clay is found to disappear whereas the peak at 1.1 nm is found to shift to 1.4 nm. The new peak positions observed at 2.8 and 1.4 nm corresponding to d_{001} and d_{002} planes can be ascribed to the intercalation of the polymer in the inter gallery space. It is observed that the d_{001} shows reduced intensity for all the composites. The lower intensities of the diffraction peaks for the

composites than pristine clay indicate disordering of the layered clay due to intercalation of the polymer between the interlayer. At lower clay percentage (PNC1.5, PNC3) second order diffraction peak is observed. However, at 7 % clay content, the significant reduction in the peak intensity suggests the presence of partially exfoliated structures^(1,2,3), and no higher order peaks are observed. The results of XRD analysis can be explained on the basis of the intercalation of the polymer in the intergallery space. At low percentage (PNC1.5, PNC3), the intercalation takes place without much disruption of the ordered layer structure thus leading to higher order peaks. However, at higher clay percentage (PNC7), intercalation of polymer leads to disorder in the platelets. This results in a decrease in the XRD peak intensity.

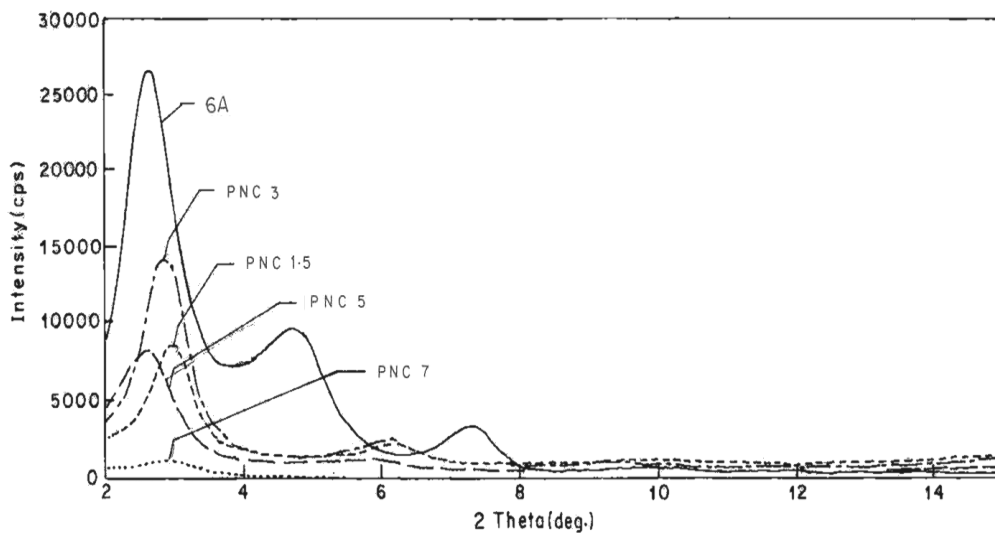


Figure 3.2.1: XRD of 6A and PVDF/6A Nanocomposites

PVDF exhibits polymorphism and is known to crystallize in four different phases namely α , β , γ , and δ . The most readily formed crystal structure is the α phase and can be obtained by cooling from the melt. On orientation it converts to the β phase, which is of very much importance because of its piezo- and pyro- electric effects. The α phase consists of a series of non-polar anti-parallel chains while the β phase consists of a series of polar parallel chains. Another structure, the γ phase is obtained by crystallization from some highly polar solvents, or by high temperature

annealing, or by high-pressure crystallization. This conformation is intermediate between α and β phases. Mechanical orientation of γ phase yields β phase. The δ phase is obtained by polarization of α phase under high electric field (approximately 1.25 MV/cm, at room temperature) ^(4, 5, 6). The transformation of the polymer melt to α phase is kinetically favored where as β phase is favored for energetic reasons ⁽⁶⁾. Some substrates are known to induce β formation when crystallized from melt. ⁽⁶⁾ Figure 3.2.2 compares the XRD pattern of pristine PVDF and PVDF in the composites. It can be clearly seen that the pristine PVDF exhibits α phase as evidenced by the peaks at 2θ values 17.2° , 17.9° , 19.5° corresponding to d spacing of 0.51 nm, 0.49 nm and 0.45 nm. The XRD pattern of PVDF in nanocomposites does not show the characteristic peaks of the α phase. In case of nanocomposites, it is observed that a single peak at $2\theta = 20.5^\circ$ is observed corresponding to (110) and (200) planes of β phase of PVDF ⁽⁷⁾. As can be seen from the figure, the XRD pattern of PVDF is significantly different than that observed for PVDF and the characteristic peaks of α phase are no longer visible. Thus the addition of clay seems to promote formation of β phase in PVDF.

The β phase of PVDF is of great interest as it exhibits various interesting physical properties like piezoelectricity and pyroelectricity. It is obtained when PVDF is crystallized under high pressure or by drawing at low temperature or ultra drawing at high temperature ⁽⁸⁾. In case of PVDF/PMMA blend, Yang et al ⁽⁹⁾ noted that PVDF crystallized in β phase when the blend was crystallized from solution. This was observed only in case of blend composition with low PVDF content (less than 5 %). However, for higher PVDF content, when the domain size of PVDF was larger than 150 nm, PVDF crystallized as bulk. The observed β phase in PVDF/PMMA blends was attributed to the crystallization of PVDF in spatially confined state. In the present study, the presence of β phase in PVDF/6A nanocomposites may also be attributed to the crystallization of PVDF in a confined state.

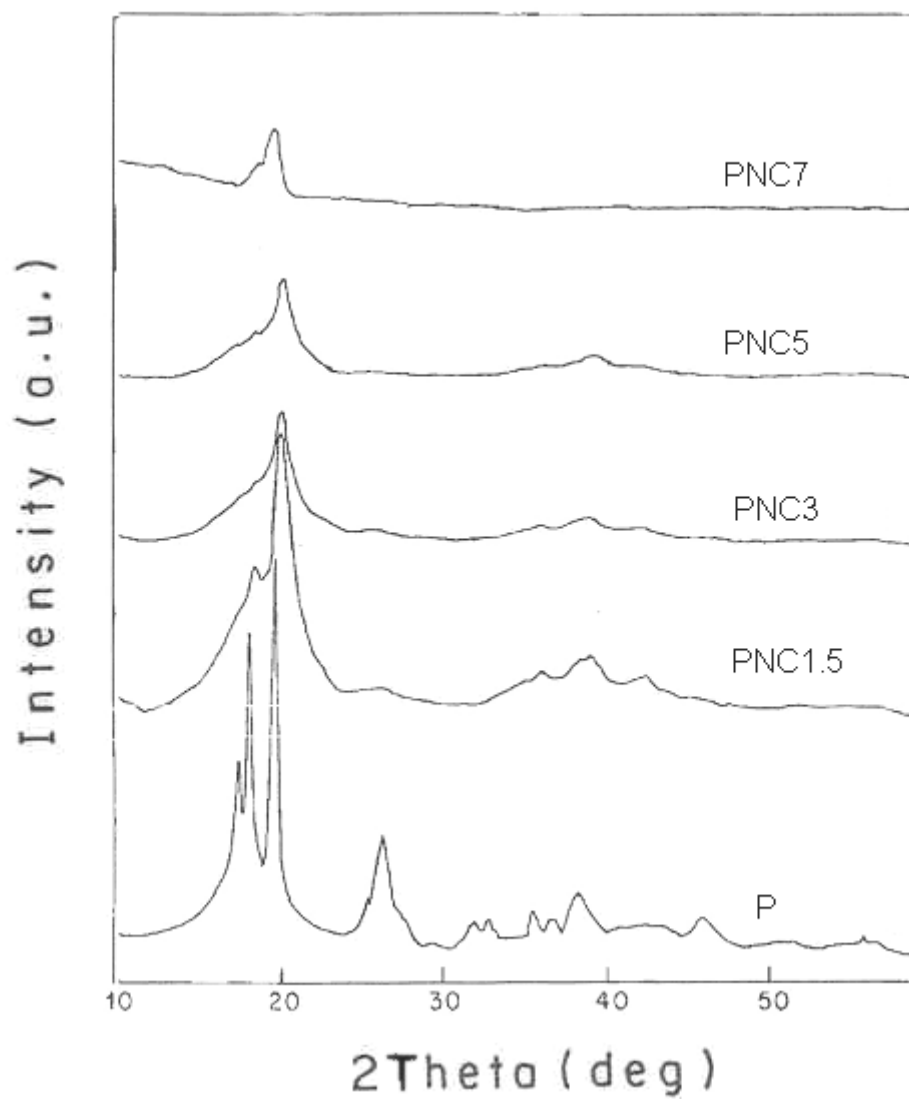


Figure 3.2.2: XRD showing α phase of pristine PVDF and β phase of PVDF in PVDF/6A nanocomposites

3.2.1.2 Fourier Transform Infrared Spectroscopy (FTIR)

The FTIR studies of PVDF and PNC are carried out in order to ascertain the presence of β phase of PVDF. In the pure PVDF films the bands obtained at 495, 538, 769, 798.5, 981.7 cm^{-1} can be assigned to α phase. The bands at 769 cm^{-1} are assigned to CF bending mode and skeletal bending of C (F)-C (H)-C(F). The peaks at 981 cm^{-1} are assigned to the CH_2 twisting mode.

Figure 3.2.3 shows the FTIR spectrum of PVDF and one of the PVDF/Clay Nanocomposites. In the nanocomposites, the bands obtained at 510 cm^{-1} (CF-bending), 846.7 cm^{-1} (CH_2 rocking), 896.8 cm^{-1} can be assigned to the β phase of PVDF. The band at 510 cm^{-1} and 847 cm^{-1} are assigned to CF bending and CH_2 rocking respectively. The absence of γ phase can be confirmed from the absence of CH_2 twisting band at 950 cm^{-1} (10, 11, 12).

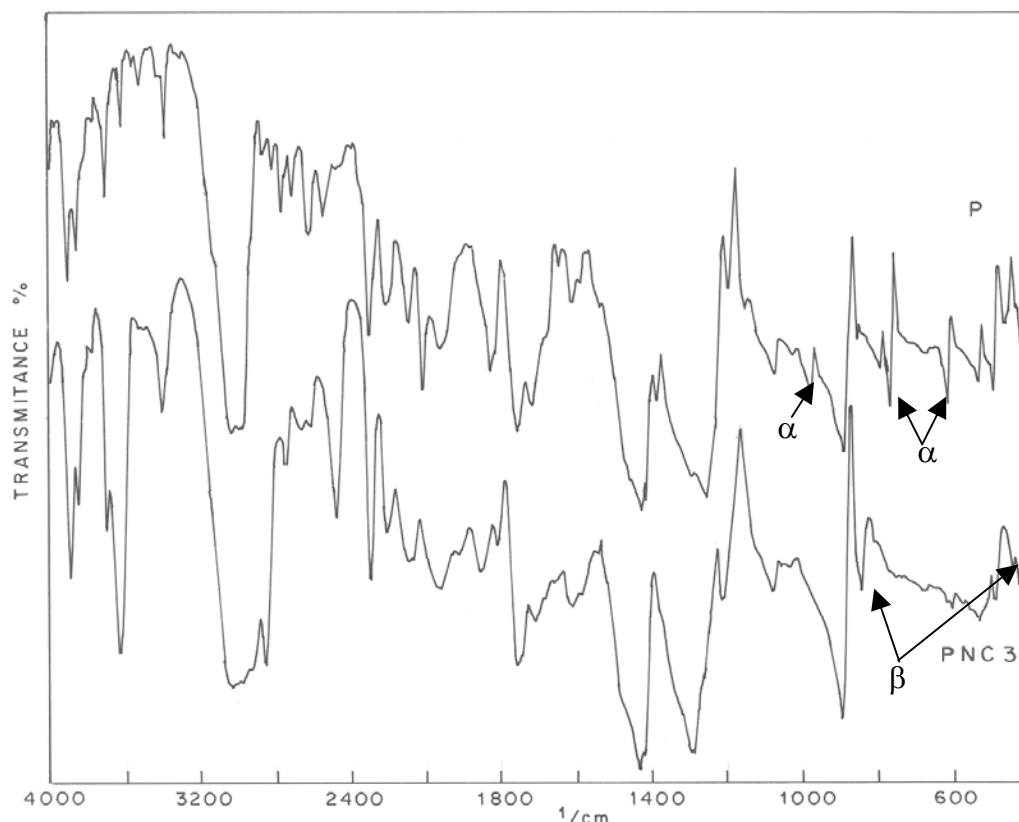


Figure 3.2.3: FTIR of PVDF and one of the nanocomposites containing 3% of 6A showing α and β phases respectively

3.2.2 Morphology

3.2.2.1 Optical Microscopy

PVDF is observed to crystallize in a normal, large, isotropic spherulitic morphology. On full growth, the spherulites are observed to impinge upon each other (figure 3.2.4). Figure 3.2.5 and 3.2.6 shows the effect of addition of clay and intercalation of polymer in the clay layers. The addition of clay affects the spherulitic

morphology. It is seen that the size of the spherulites goes on decreasing with increase in clay content. The addition of 1.5% of clay impedes the spherulitic growth. On further addition of clay (e.g., 5% of clay) the spherulitic growth is completely restricted as can be seen in figure 3.2.6.

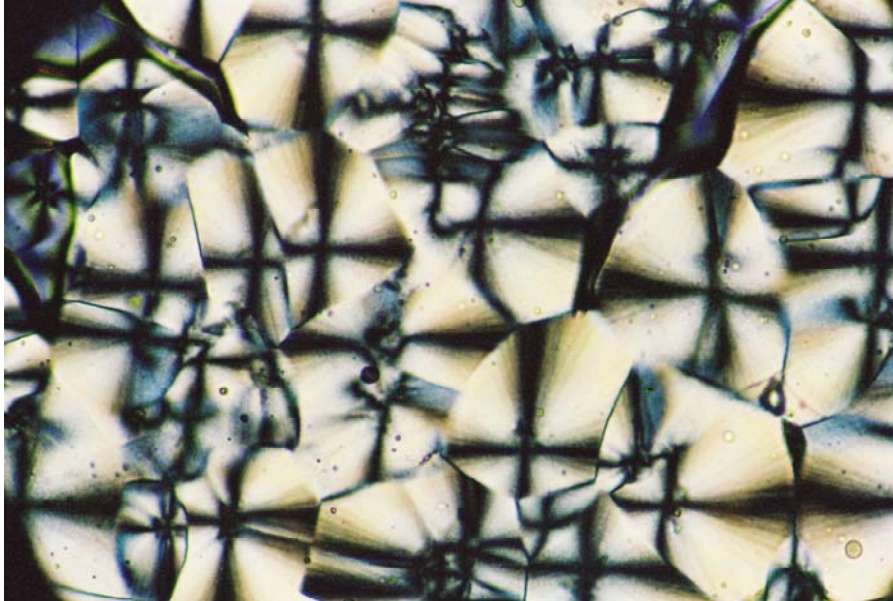


Figure 3.2.4: Optical Micrograph of PVDF crystallized at 148 °C. Magnification 32X

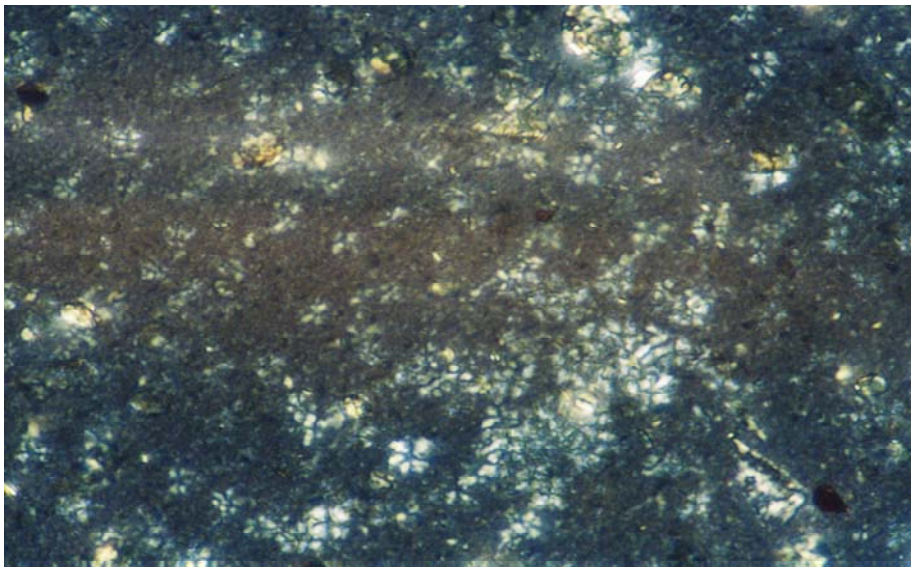


Figure 3.2.5: Optical Micrograph of PNC1.5 crystallized at 152 °C. Magnification 32X



Figure 3.2.6: Optical Micrograph of PNC5 crystallized at 152 °C. Magnification 32X

3.2.3 Thermal Properties- Differential Scanning Calorimetry

3.2.3.1 Melting and Non-Isothermal Crystallization

Table 3.2.1: Non-isothermal melting and crystallization parameters of PVDF and PVDF/6A clay nanocomposites

Sample code	Melting Temperature, T_m (°C)	Crystallization Temperature, T_c (°C)	$\Delta T = (T_m - T_c)$ (°C)	ΔH_f^* (Cal/g)	Crystallinity (%)
P	172	141	31	11.7	47
PNC1.5	178	152	26	11.4	45
PNC3	179	152	27	10.7	43
PNC5	181	152	29	9.56	38
PNC7	181	151	30	9.6	38

* ΔH_f values are normalized with respect to PVDF

Table 3.2.1 presents the melting and crystallization temperatures and degree of crystallinity of PVDF and PVDF/clay nanocomposites. The melting points of PVDF/6A nanocomposites are found to shift from 172 to 178-181 °C (Table-3.2.1).

The melting point of α phase and β phase are reported to be 172 and 178 °C respectively ⁽⁸⁾. The higher melting point of PVDF in the nanocomposites thus supports the XRD results suggesting the β phase of PVDF. The heat of fusion of PVDF is found to decrease from 11.7 to 9.6 cal/g. The decrease in the heat of fusion indicates lower extent of crystallinity of PVDF composites. The percentage crystallinity of PVDF can be calculated using a value of the heat of fusion for the 100% crystalline PVDF as 25 cal/g ⁽¹³⁾. Since similar value of Heat of fusion has been reported for 100% crystalline α and β PVDF, here also it has been used for calculating the percentage crystallinity. The percentage crystallinity of PVDF decreases from 47 % to 38 % on addition of clay as can be seen from the table 3.2.1. The crystallization during cooling takes place under non-isothermal conditions. The non-isothermal crystallization curves show that PVDF in PVDF/clay nanocomposites crystallizes at a higher temperature (about 152 °C) relative to pristine PVDF (141 °C). Thus a shift of about 10-11 °C in the non-isothermal crystallization peak of PVDF indicates that the crystallization process is enhanced in the presence of clay platelets.

3.2.3.2 Isothermal Crystallization

Isothermal crystallization of PVDF and PVDF/clay nanocomposites is studied to find out the effect of clay on the isothermal crystallization behavior. The isothermal exothermic peaks recorded were analyzed using Avrami's theory ^(14, 15, 16).

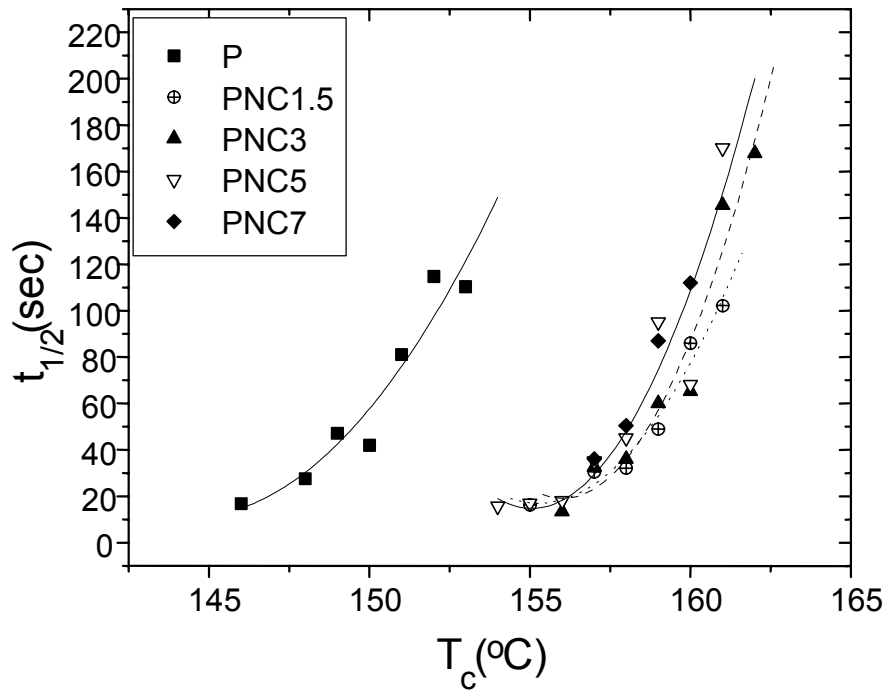


Figure 3.2.7: $t_{1/2}$ vs. T_c of PVDF/6A nanocomposites

Figure 3.2.7 illustrates the temperature dependence of crystallization half time ($t_{1/2}$), on crystallization temperature (T_c) for PVDF and nanocomposites. As is shown in the figure, PVDF/clay nanocomposites exhibit a shift in the crystallization temperature to higher temperatures for all the nanocomposites, over the temperature range studied. This indicates that the crystallization process of PVDF in the nanocomposites is accelerated due to the presence of clay. Similar enhancement of crystallization has been reported in PP/clay⁽¹⁷⁾ and PET/clay nanocomposites⁽¹⁸⁾. However, the extent of enhancement in crystallization behavior does not show any composition dependence.

3.2.4 Dynamic Mechanical Analysis

Dynamic mechanical analysis is often used to study the relaxations in polymers. The analysis of storage modulus and $\tan \delta$ curves is very useful in ascertaining the performance of the sample under stress and temperature.

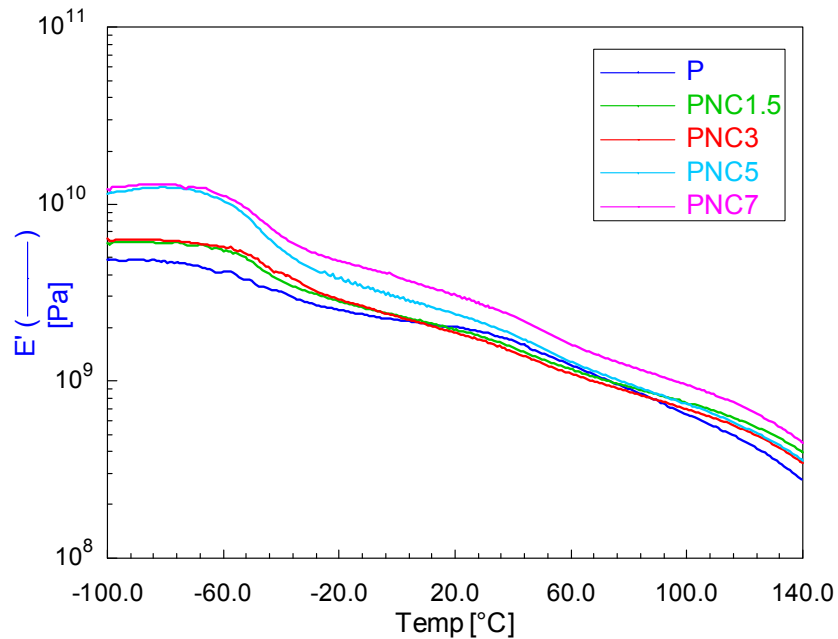


Figure 3.2.8: Temperature dependence of storage modulus (E') for PVDF and PVDF/6A clay nanocomposites

Figure 3.2.8 shows the storage modulus of PVDF and PVDF nanocomposites. As shown in the figure, PVDF nanocomposites show higher values of storage modulus over the entire temperature range of the study (-100 °C to 140 °C). The storage modulus increased with increase in clay content^(19, 20). Similar increase of dynamic storage modulus is reported for polymer/clay nanocomposites^(17, 21).

The effectiveness of clay as reinforcement can be elucidated as follows. The increase in the storage modulus of the nanocomposites is expressed in terms of the ratio of modulus of the composite (E_c') to the modulus of pristine polymer (E_p'). Table 3.2.2 presents the E_c'/E_p' at three temperatures. As can be seen from the table, the ratio E_c'/E_p' increases with increase in clay %. At very low percentage of clay, and low temperature (-100°C) the increase is about 25%; however at room temperature, a decrease of E_c'/E_p' ratio results due to the softening of the matrix phase. As the clay % increases from 1.5 % to about 7 %, the ratio E_c'/E_p' significantly increases from 1.25 to 2.55 corresponding to an increase in the modulus of 25 to 155

%. Even at high temperature i.e., at 100 °C well above the glass transition temperature of the polymer, it is observed that the increase in modulus is about 45 % for 7 % clay content. The significant improvement in the storage modulus at temperatures higher than the glass transition temperature of PVDF clearly confirms the reinforcing effect of clay in PVDF/clay nanocomposites.

Table 3.2.2: E_c/E_p' values of PVDF/6A at different temperatures

Sample identification	E_c/E_p'		
	At -100 °C	At 30 °C	At 100 °C
PNC1.5	1.25	1.0	1.16
PNC3	1.34	1.0	1.06
PNC5	2.36	1.13	1.15
PNC7	2.55	1.40	1.45

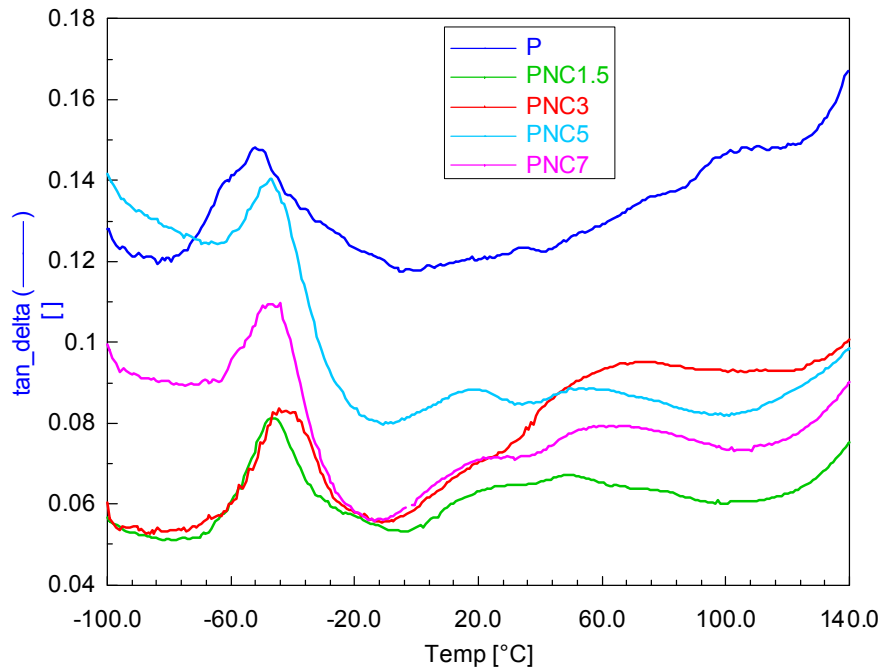


Figure 3.2.9: Tan δ vs. temperature curves for PVDF and PVDF/ 6A clay nanocomposites

Figure 3.2.9 shows the $\tan \delta$ curves of PVDF and PVDF/clay nanocomposites. The $\tan \delta$ curve shows a peak at about $-50\text{ }^{\circ}\text{C}$ for PVDF, which corresponds to the glass transition temperature of PVDF. In the case of PVDF/clay nanocomposites, the $\tan \delta$ peak shifts to higher temperature by approximately $6\text{--}8\text{ }^{\circ}\text{C}$ and the area under the $\tan \delta$ peak decreases as can be seen from figure 3.2.9. The shift of $\tan \delta$ peak to higher temperature may be ascribed to hindered cooperative motion of polymer chains. Similar increase was observed for polyimide/clay nanocomposites by Agag et al ⁽²²⁾. In addition to the $\tan \delta$ peak at about $-50\text{ }^{\circ}\text{C}$, the nanocomposites exhibit two more $\tan \delta$ peaks at $20\text{ }^{\circ}\text{C}$ and $60\text{ }^{\circ}\text{C}$. In PVDF, a high temperature transition (α) has been reported at about $80\text{ }^{\circ}\text{C}$ and is assigned to the liberation of polymer chains in the crystalline regions. The high temperature peak ($60\text{ }^{\circ}\text{C}$) thus can be ascribed to this α transition. The peak at $20\text{ }^{\circ}\text{C}$ may correspond to the release of constrained amorphous phase. The presence of such restrained polymer chain relaxation has been noted in other polymers and polymer composites ⁽²³⁾. In particular additional $\tan \delta$ at temperatures higher than the glass transition temperature has been observed by Tsagaropoulos and Eisenberg ⁽²⁴⁾ in several polymers filled with fine silica. The presence of high temperature $\tan \delta$ peak was assigned to the glass transition of regions containing chains of reduced mobility. As noted earlier, the crystallinity of the nanocomposites is lower than that of pristine polymer suggesting higher amorphous content. Since the $\tan \delta$ peak is related to the amorphous content of the polymer, it is expected that the nanocomposites with higher amorphous content would show a higher $\tan \delta$ peak value. However, the $\tan \delta$ peak values are lower for the composites than for the pristine polymer. The lower values of $\tan \delta$ peak signifies restricted molecular motion of PVDF in PVDF/clay nanocomposites, which could be ascribed to the presence of a constrained fraction as defined by Kojima et al ⁽²⁵⁾ and Shelley et al ⁽²⁶⁾. Similar decrease in $\tan \delta$ peak was observed in the case of Polyamide 6/silica nanocomposites by Yang et al ⁽²⁷⁾. They have attributed it to the good adhesion between the polymer and silica particles. Thus the reduced $\tan \delta$ peak (α transition) and presence of additional $\tan \delta$ peak at temperature higher than the glass transition temperature suggests the presence of

constrained fraction with reduced mobility of polymer chains. This constrained fraction is also responsible for the increase in modulus as shown by Shelley et al ⁽²⁶⁾.

3.2.5 Coefficient of Thermal Expansion

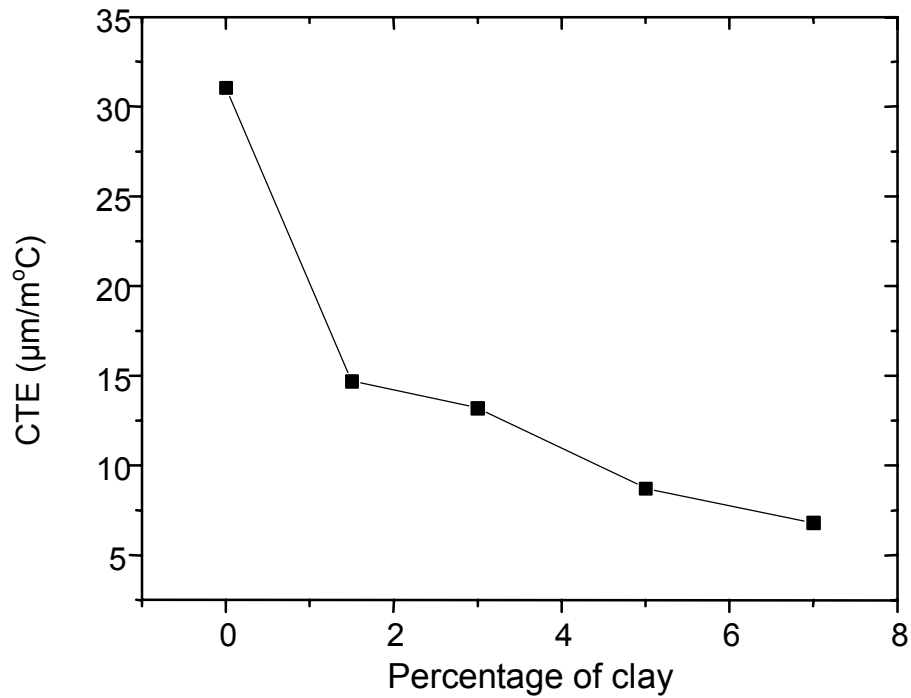


Figure 3.2.10: Variation of Coefficient of Thermal Expansion with percentage of clay for PVDF/6A nanocomposites

The nanocomposites are known to exhibit better dimensional stability as compared to the pristine polymer. Coefficient of thermal expansion (CTE) can be used as a tool to measure the dimensional stability. The coefficient of expansion was measured over a temperature range of $-100\text{ }^\circ\text{C}$ to $140\text{ }^\circ\text{C}$. Figure 3.2.10 depicts the variation of CTE as percentage of clay. It can be seen from the figure that CTE decreases sharply at 1.5 % clay content by about 50 %. Further increase in the clay content results in a decrease in the CTE. The addition of clay platelets thus decreases the coefficient of thermal expansion significantly. The lower CTE values for the nanocomposites confirm the dimensional stability of the nanocomposites ⁽²²⁾.

3.2.6 Melt Rheology

Rheological study of the properties of the nanocomposites is important from the point of view of processing and application of the nanocomposites. The rheological behaviour of PVDF and the nanocomposites were studied at 3 different temperatures, viz., 210, 220, 230 °C.

The storage modulus, loss modulus and complex viscosity as a function of frequency are given in the figures 3.2.11-3.2.13 at a temperature of 210°C. As can be seen from the figures G' , G'' and η^* increases with increase in clay content and show non-terminal behavior at low frequencies.

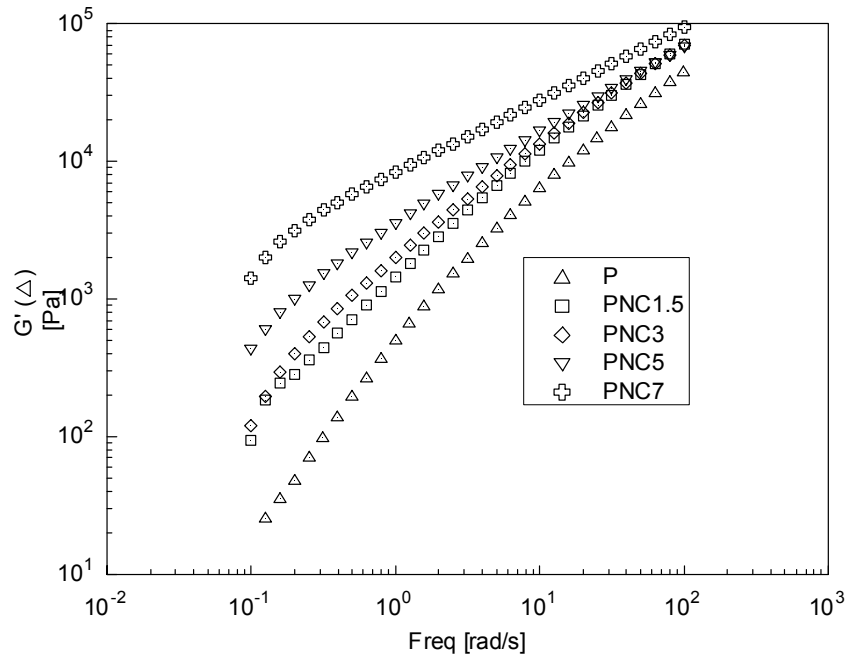


Figure 3.2.11: Frequency response of storage modulus (G') at 210 °C for PVDF/6A nanocomposites

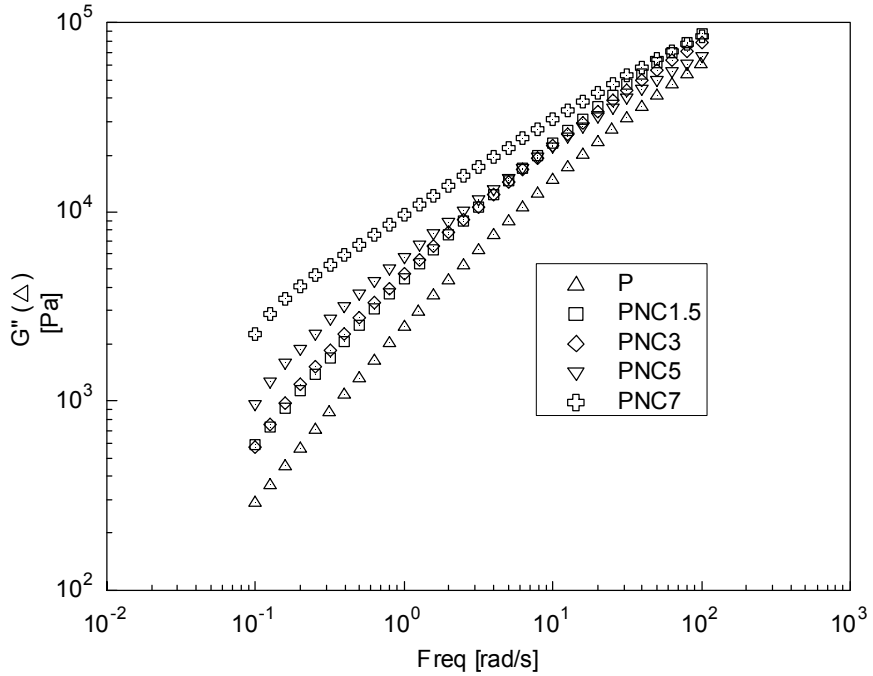


Figure 3.2.12: Frequency response of loss modulus (G'') at 210 °C for PVDF/6A nanocomposites

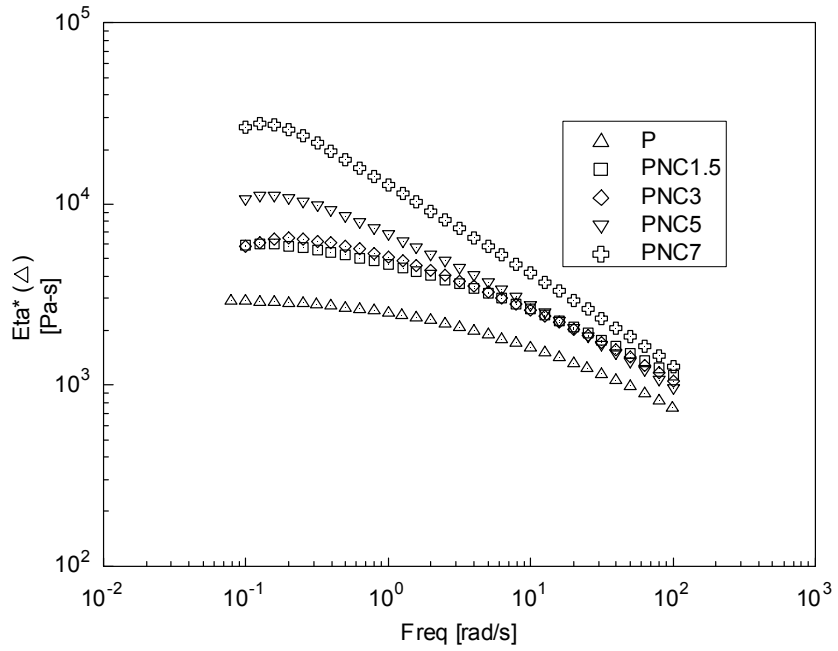


Figure 3.2.13: Frequency response of complex viscosity (η^*) at 210 °C for PVDF/6A nanocomposites

The frequency dependence of the storage modulus and loss modulus decreases to a value less than the homopolymer. The frequency dependence of storage modulus G' and G'' can be given as

$$G' \propto \omega^{1.47}$$

$$G'' \propto \omega^{0.97}$$

According to the Maxwell's model the slope of the log-log plot of frequency and G' and G'' should have been 2 and 1 respectively. But the homopolymer being a poly disperse sample, lesser values are obtained. The slope of the η^* with respect to the frequency is called as the shear thinning exponent (n). For Newtonian liquids $n = -0.2$.

The frequency dependence of the storage, loss modulus and complex viscosity of the nanocomposites are summarized in the table 3.2.3.

Table 3.2.3: Rheology- Low Frequency behaviour of PVDF/6A nanocomposites at 210°C

Sample	Slope of G'	Slope of G''	Slope of η^* (n)
P	1.4731	0.9682	-0.04493
PNC1.5	0.9896	0.8785	-0.1471
PNC3	1.0157	0.8468	-0.2115
PNC5	0.8856	0.7561	-0.2497
PNC7	0.6153	0.5726	-0.4288

Shear thinning exponent (n) decreases on addition of clay. It is a quantitative parameter, which characterizes the nano, and meso disperse composites. The lower value implies that there is a marked difference from the Newtonian flow at low frequencies, which is caused by the intercalated structures. It has been shown by Wagener et al ⁽²⁸⁾ that well exfoliated samples display higher magnitude of 'n' while absence of exfoliation results in 'n' closer to zero. The higher magnitude of 'n' suggests partial exfoliation of clay layers. These results are consistent with those of XRD results, which shows partial exfoliation.

Data was acquired at three temperatures, 210, 220 and 230 °C using a strain of 2% and shifted using time temperature superposition at 210 °C to form the master curve. It was assumed that at these temperatures the polymer chains would be completely relaxed. It is observed that the time temperature superposition holds for all the compositions as is shown in the figure 3.2.14. Only a horizontal shift (a_T) was used for performing this, since there are no special features associated with the modulus data. It was fitted using Arrhenius equation and the graph so obtained was smoothened. There was a monotonic increase in the storage modulus with frequency. The non-terminal behavior observed in the nanocomposites could be a result of the retardation of molecular relaxation processes produced by the intercalation of polymer chains into the clay layers, entanglement or physical cross linking of the polymer chains to the clay surface. The observed low-frequency response is similar to the reported work on other nanocomposites of PS-PI diblock copolymer and PCL (29, 30)

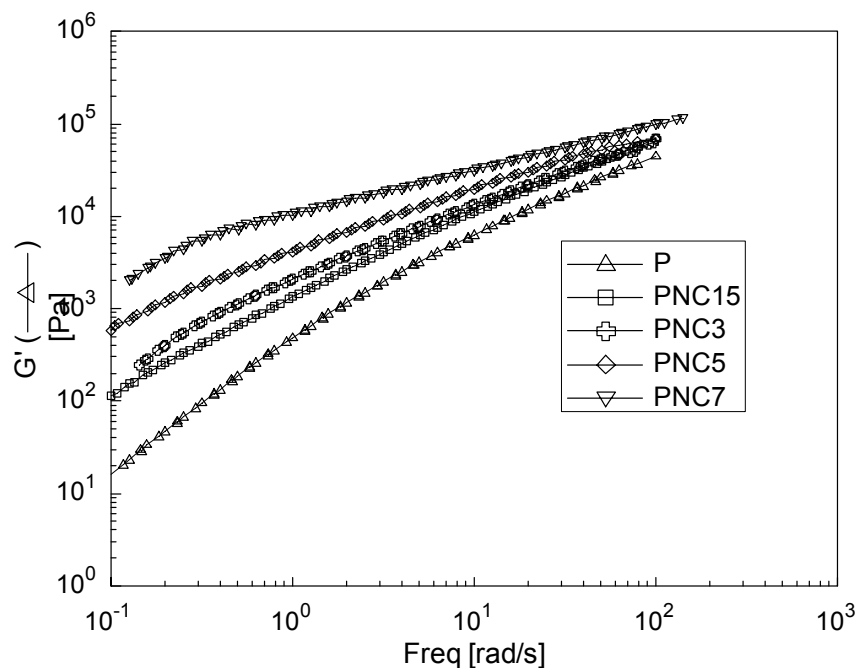


Figure 3.2.14: Master curve overlay of G' of PVDF and PVDF/ 6A shifted to 210°C

3.2.7 Stability of β Phase in PVDF Nanocomposites

Annealing of the PVDF and PVDF nanocomposites is carried out in order to ascertain the thermal stability of β crystals formed in the nanocomposites. The two annealing temperatures 125 °C and 185 °C were chosen such that former was below the melting point while the later was above the melting point, thus ensuring enough molecular mobility in the polymer. Figure 3.2.15 exhibits XRD scans of sample annealed at 185 °C. PVDF remains in the α phase as evidenced from the presence of characteristic peaks at 2θ values of 17.3° (020), 18.15° (110), 26.8° (021) and 38.8° (002). The β phase of PVDF/clay nanocomposites remains unchanged even after annealing at 185°C. It is reported that annealing of α phase films at 185.8 °C and atmospheric pressure leads to transformation into γ phase ⁽⁶⁾. In PVDF/clay nanocomposites however, the γ phase of PVDF is not observed from the XRD pattern and DSC melting point peaks.

On annealing at 125 °C, which is below melting point of the nanocomposite, no changes are observed in the crystal structure of pristine PVDF as well as in that of the nanocomposites. It is observed that after annealing the sample at these temperatures for 24 hours, the PVDF in the nanocomposites remains in β phase as is evidenced by XRD patterns and the melting point peak values observed from the DSC curves. PVDF is also reported to crystallize in β phase in PVDF/PMMA blends by Yang et al ⁽¹⁵⁾. However, the observed β phase was thermodynamically metastable as evidenced by its transformation to a stable phase after annealing. It was observed that the β phase was a result of crystal growth in limited space and time. In the present case the β phase induced by presence of clay remains stable even after annealing.

This result is of particular interest as the stability of β phase is of importance from the processing point of view in down stream processing of the composites.

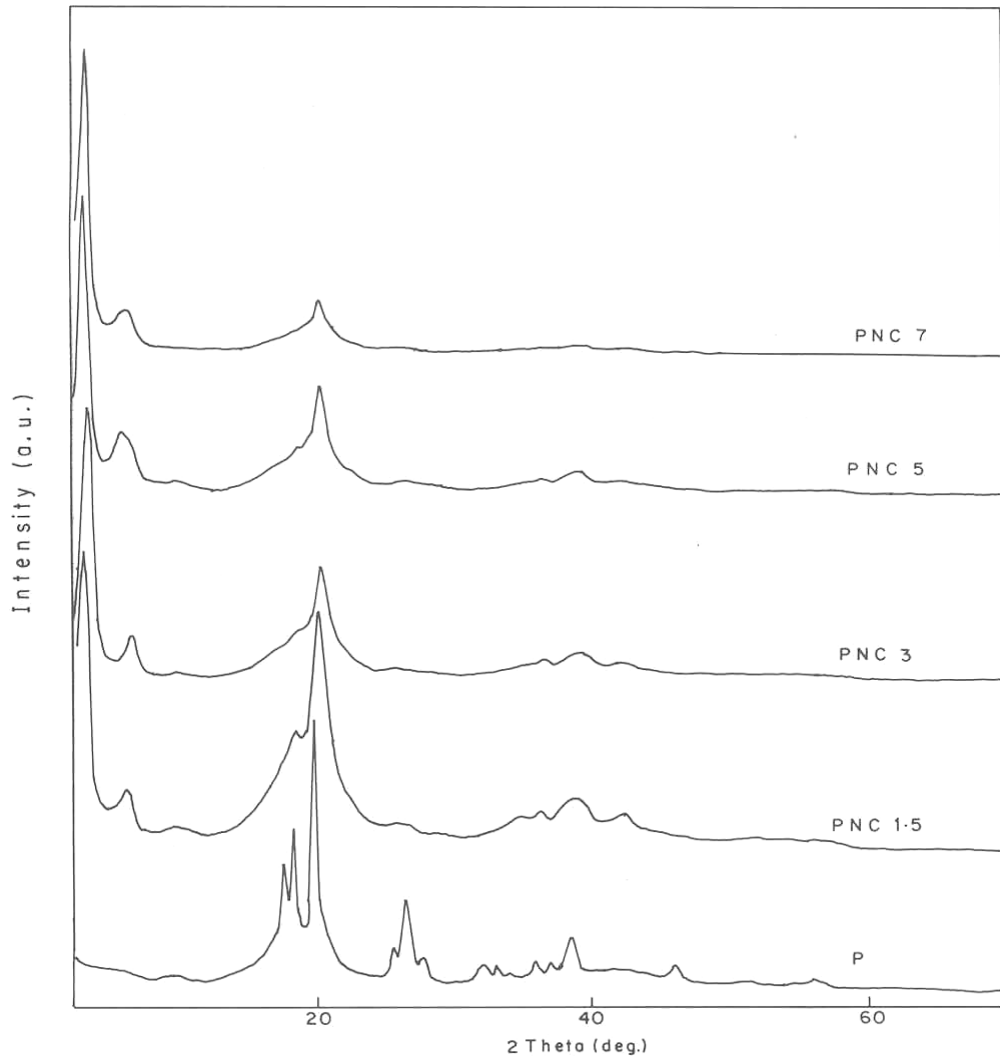


Figure 3.2.15: XRD of samples annealed at 185 °C

The melting point and heat of fusion of the PVDF and nanocomposites annealed at 125 °C and 185 °C are summarized in the table 3.2.4. The melting point remains similar to that of the unannealed samples. This also confirms the stability of the β phase in the nanocomposites. The Heat of fusion of samples annealed at 185 °C is higher indicating the increase in crystallinity.

Table 3.2.4: Melting parameters for annealed PVDF and PVDF/6A nanocomposites samples

Sample code	Annealed at 125°C		Annealed at 185°C	
	T _m (°C)	ΔH _f (Cal/g)	T _m (°C)	ΔH _f (Cal/g)
P	174	10.5	173	13.4
PNC1.5	180	8.8	183	13.6
PNC3	180	8.8	182	13.9
PNC5	182	8.8	183	13.4
PNC7	180	8.5	180	15.1

3.3 Conclusions

The XRD scans of the nanocomposites show intercalated structure and the reduced intensities of the peak indicate partially exfoliated structure. Non-isothermal and the isothermal crystallization studies show enhanced crystallization of PVDF. Dynamic mechanical analysis indicates improved storage modulus over the temperature range studied and the extent of increase is dependent on clay %. Glass transition temperature is found to increase by approximately 6-8 °C indicating restricted chain mobility in the nanocomposite. Tan δ curves exhibit two peaks corresponding to T_g of the polymer and release of constrained phase due to clay. Rheological studies also indicate presence of partially exfoliated structures. Presence of β phase of PVDF is observed when crystallized in the presence of clay. Thermal stability of the observed β phase is ascertained from the thermal annealing experiments carried out at 125°C and 185 °C.

References

1. R. A. Vaia, E. P. Giannelis, *Macromolecules*, **30**, 8000 (1997)
2. R. A. Vaia, K. D. Jandt, E. J. Kramer, E. P. Giannelis, *Chemistry of Materials*, **8**, 2628 (1996)
3. J. Ren, A.S. Silva, R. Krishnamoorthy, *Macromolecules*, **33**, 3739 (2000)
4. M. A. Marcus, *Ferroelectrics*, **40**, 29 (1982)
5. W.T. Chen, E. Sacher, D.H. Strobe, J.J. Woods, *Journal of Macromolecular Science Part B: Physics*, **B21 (3)**, 397 (1982)
6. R. Gregorio, M. Cesari, N. Chaves, P.S. Nociti, J.A. Mendonca, A.A. Lucas, in *The Polymeric materials encyclopedia*, CRC press, Inc, 1996
7. A. Tawnasi, A.H. Oraby, E.M Abdelrazek, M. Abdelaziz, *Polymer testing*, **18**, 569 (1999)
8. R. Gregorio, M. Cesari, N. Chaves, P.S. Nociti, J.A. Mendonca, A.A. Lucas, in *The Polymer Materials Encyclopedia 1996*, CRC Press, Inc
9. X. Yang, X. Kong, S. Tan, G. Li, W. Ling, E. Zhou, *Polymer International*, **49**, 1525 (2000)
10. I.S. Rocha, L.H.C. Mattoso, C.F. Malmonge, R. Gregorio Jr., *Journal of Polymer Science Part B: Polymer Physics*, **137**, 1219 (1999)
11. W. K. Lee, C. S. Ha, *Polymer*, **39**, 7131 (1998)
12. K. M. Kim, K. S. Ryu, S. G. Kasng, S. H. Chang, I. J. Chung, *Macromolecular Chemistry and Physics*, **202**, 866 (2001)
13. H. Nagawada, Y. Ishida, *Journal of Polymer Physics*, **11**, 2153 (1973)
14. M Avrami, *Journal of Chemical Physics*, **7**, 1103 (1939)
15. M Avrami, *Journal of Chemical Physics*, **8**, 212 (1940)
16. M Avrami, *Journal of Chemical Physics*, **9**, 177 (1941)
17. S. S. Hambir, N. N. Bulakh, P. Kodgire, R. A. Kalgaonkar, J. P. Jog, *Journal Polymer Science Part B: Polymer Physics*, **39**, 446 (2001)
18. Y. Ke, C. Long, Z. Qi, *Journal of Applied Polymer Science*, **71**, 1139 (1999)
19. P.B. Messersmith, E.P. Giannelis, *Chemistry Of Materials*, **46**, 1719 (1999)
20. J. Chang, D.K. Park, K.J. Ihn, *Journal Polymer Science Part B: Polymer Physics*, **39**, 471 (2001)

21. P. Kodgire, R. Kalgaonkar, S.S. Hambir, N.N. Bulakh, J.P. Jog, *Journal Of Applied Polymer Science*, **81**, 1786 (2001)
22. T. Agag, T. Koga, T. Takeichi, *Polymer*, **42**,3399 (2001)
23. M.P. Sepe, *Advanced Material Processing*, **4**, 32 (1992)
24. G. Tsagaropoulos, A. Eisenberg, *Macromolecules*, **28**, 6067 (1995)
25. A. Usuki, Y. Kojima, M. Kawasumi, A. Okada, Y. Fukushima, T. Kuraunchi, O. Kamagaito, *Journal of Materials Research*, **8**, 1185 (1993)
26. J.S. Shelley, P. T. Mather, K. L. Devoirs, *Polymer*, **42**, 5849 (2001)
27. F Yang, Y Ou, Z. Yu, *Journal of Applied Polymer Science*, **69**, 355 (1998)
28. R. Wagener, T. J. G. Reisinger, *Polymer*, **44**, 7513 (2003)
29. J. Ren, A. S. Silva, R. Krishnamoorti, *Macromolecules*, **33**, 3379 (2000)
30. R. Krishnamoorti, E. P. Giannelis, *Macromolecules*, **30**, 4097 (1997)

Chapter 4
PVDF (SOLEF 1008)/ Clay
Nanocomposites: Effect of
Modifier and Concentration

Chapter 4

4 PVDF (SOLEF 1008)/Clay Nanocomposites: Effect of modifier and Concentration

4.1 Introduction

This chapter deals with the result of the study of effect of modifier and concentration on the properties of the nanocomposites of PVDF/clay. The effect of concentration of modifier is studied using Cloisite 20A clay, which has the same modifier as 6A but a lower organic content. Since the property enhancement achieved in PVDF/6A system ⁽¹⁾ was marginal, probably due to higher organic content, it is of interest to see the effect of the same clay treatment but different percentage of organic content on the properties of PVDF/clay nanocomposites. The effect of organic modification is investigated by preparing PVDF/clay hybrids using untreated clay.

4.2 Melt intercalation using Batch mixer

The samples in this part of the study were prepared by melt intercalation in Brabender batch mixer. Samples are coded as shown in the table 4.2.1.

Table 4.2.1: Sample code and compositions of PVDF/20A nanocomposites

Weight Percentage of 20A	Sample Code
0	P
1.5	PN1.5
3	PN3
5	PN5
7	PN7

4.2.1 Results and Discussion

4.2.1.1 Structure of Nanocomposites

4.2.1.1.1 X-ray Diffraction

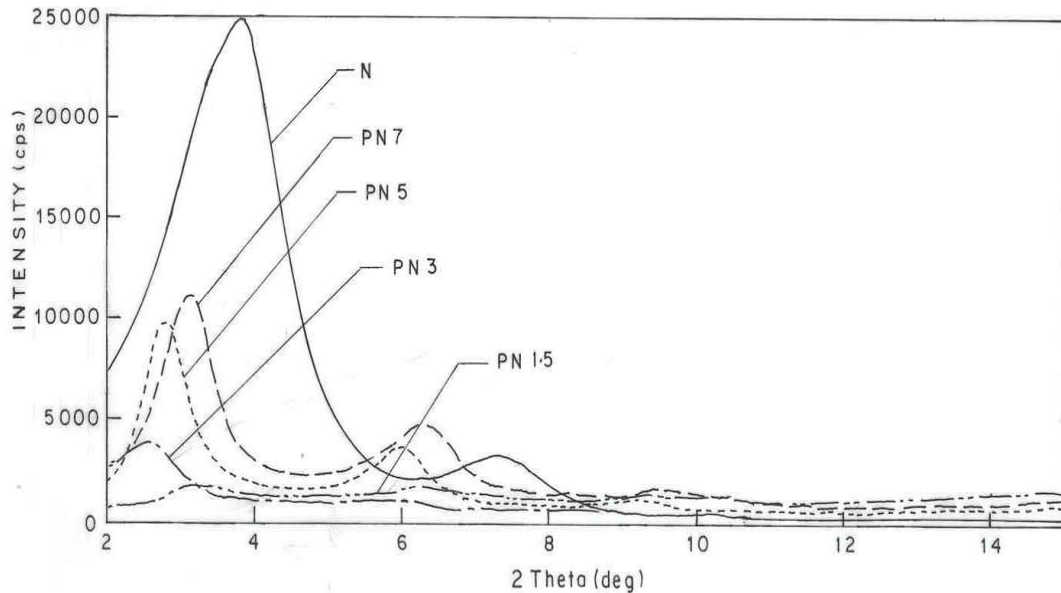


Figure 4.2.1: XRD of 20A and PVDF/20A nanocomposites

Figure 4.2.1 compares the XRD patterns of PVDF/20A nanocomposites. The organically modified clay exhibits three well-defined peaks at d spacing of 2.47 nm, 1.23 nm, and 0.87 nm corresponding to d_{001} , d_{002} and d_{003} planes. In case of nanocomposites, PN1.5 and PN3, as can be seen from the figure 4.3.1, the d_{001} peak of the clay shifted to low angles corresponding to an increase in the 'd' spacing from 2.4 nm (organically modified clay) to 2.8 nm and 3.3 nm respectively. With increase in the clay content, the d_{001} peak is found to be at 3.1 nm and 2.8 nm for PN5 and PN7, respectively. The decrease in the intensity of the peak for all the composites as compared to the pure 20A clay indicates a decrease in coherent layer scattering. The intensity of the peaks is substantially lower for PN1.5 and PN3 whereas for PN5 and PN7 the intensity is increased and the peaks are well defined. The results of XRD

analysis can be explained on the basis of the intercalation of the polymer in clay. The organophilic treatment decreases the attractive forces between the clay layers thus facilitating the intercalation of PVDF in the intergallery space. At low clay content, the intercalation of polymer leads to disordering of the layered clay structure and hence a decrease in the XRD coherent scattering intensity as is observed in Figure 4.2.1. However, on further addition of clay, the intensity of d_{001} peak increases indicating intercalation of polymer in the layers without disruption of ordered structure. For all compositions, the higher ordered peaks are observed, confirming the presence of ordered tactoids^(2, 3, 4, 5).

The crystalline form (α) of PVDF is found to change in nanocomposites. As in the case of PVDF/6A nanocomposites, PVDF is found to crystallize in β form in presence of clay in the nanocomposites. The lattice parameters for the observed β form in the nanocomposites and the α form in the pristine PVDF are calculated. The lattice parameters observed for α form are $a=0.5024$ nm, $b=0.9667$ nm, $c=0.4524$ nm. The lattice parameters for β form is calculated as $a=0.858$ nm, $b=0.491$ nm, $c=0.256$ nm from PN5 nanocomposite. These values vary with in $\pm 0.002-0.01$ nm of reported values. These are consistent with the reported values⁽⁶⁾.

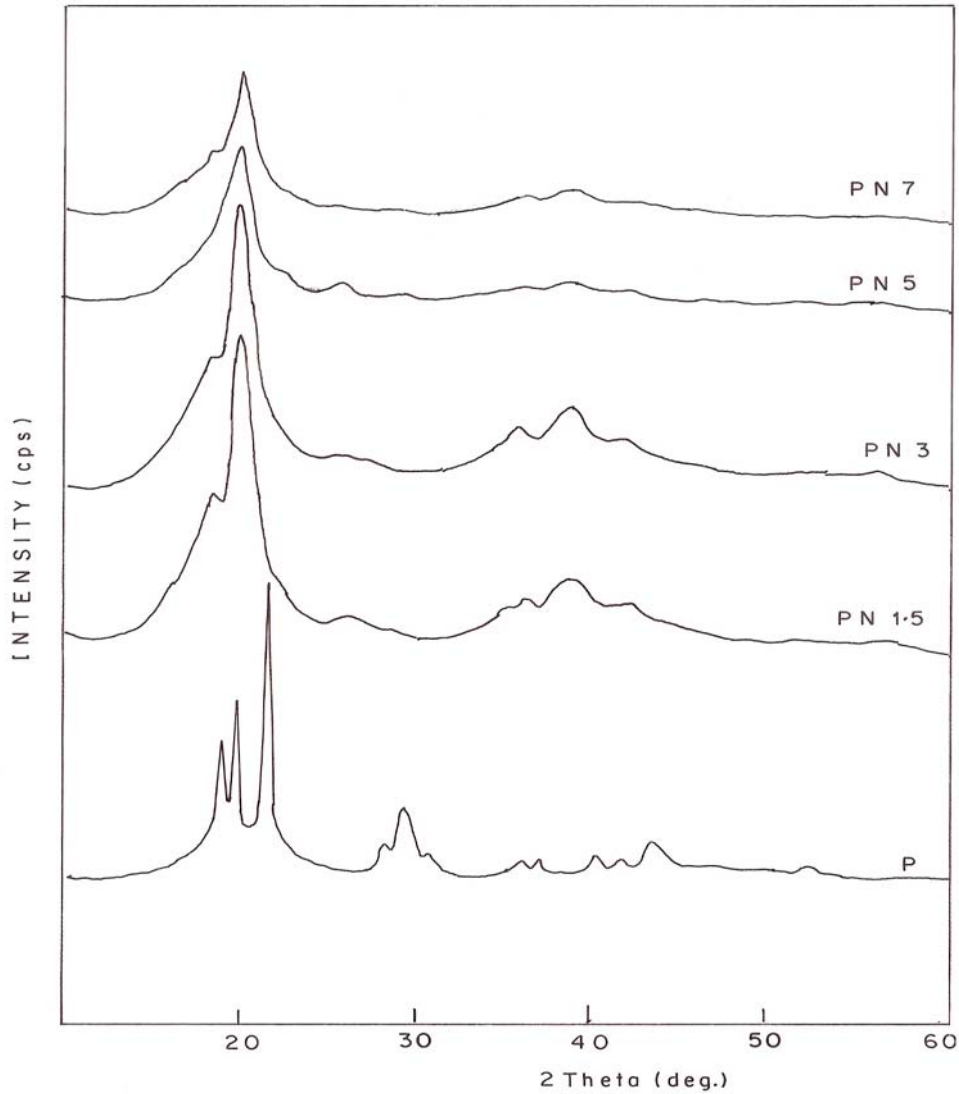
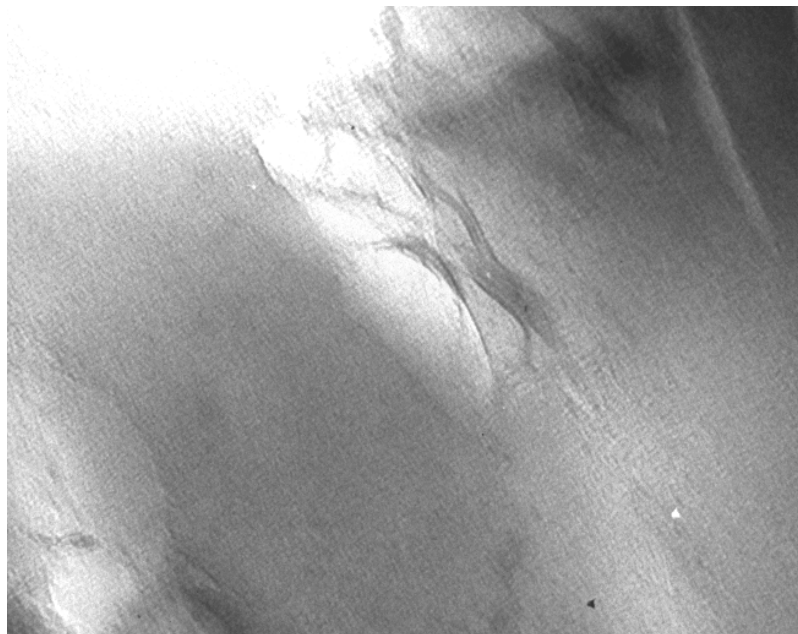


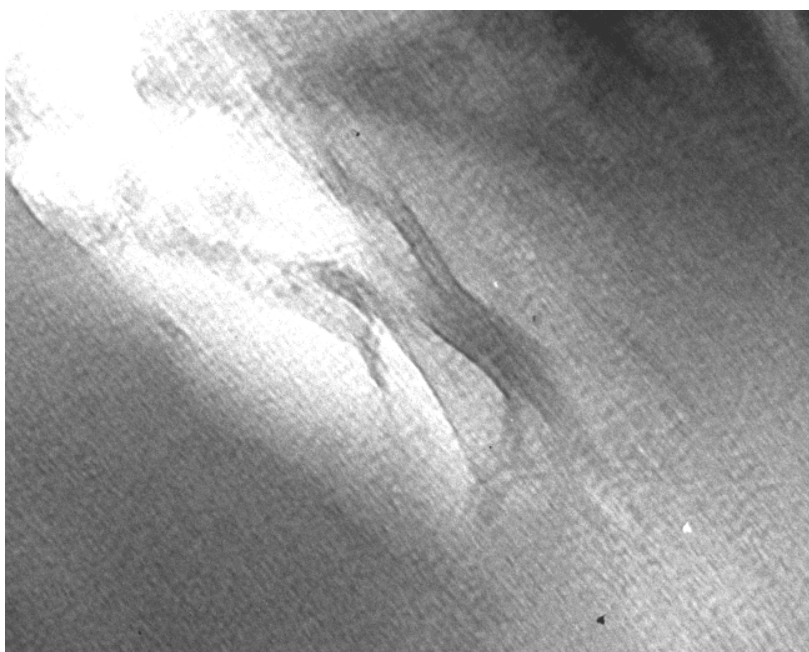
Figure 4.2.2: XRD showing α phase of pristine PVDF and β phase of PVDF in PVDF/20A nanocomposites

4.2.1.1.2 Transmission Electron Microscopy

Figure 4.2.3 illustrates the transmission electron micrograph of one of the samples showing the clay dispersion in the nanocomposites. The clay layers in the form of tactoids are dispersed with in polymer matrix. PVDF and pristine clay has approximately equal density and thus exhibit low contrast in the TEM image.



50 nm



50 nm

Figure 4.2.3: Transmission electron micrograph of PN5 nanocomposite at two different magnifications

4.2.1.2 Morphology

Figure 4.2.4 and 4.2.5 shows the optical micrographs of PVDF and PVDF/20A nanocomposites. The presence of clay layers results in increased nucleation and thus reduction in spherulitic size. With increase in clay percentage the spherulitic growth is impeded as can be seen in figure 4.2.6.

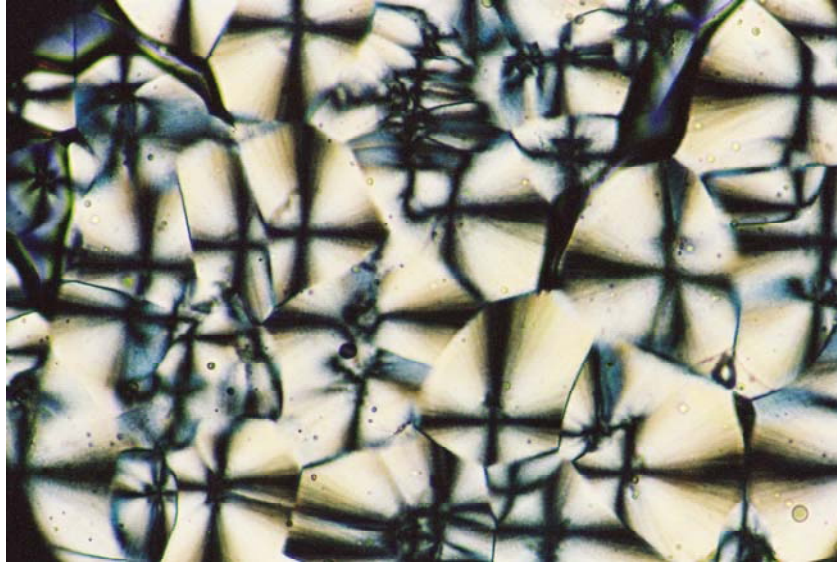


Figure 4.2.4: Optical Micrograph of PVDF crystallized at 148 °C. Magnification 32X

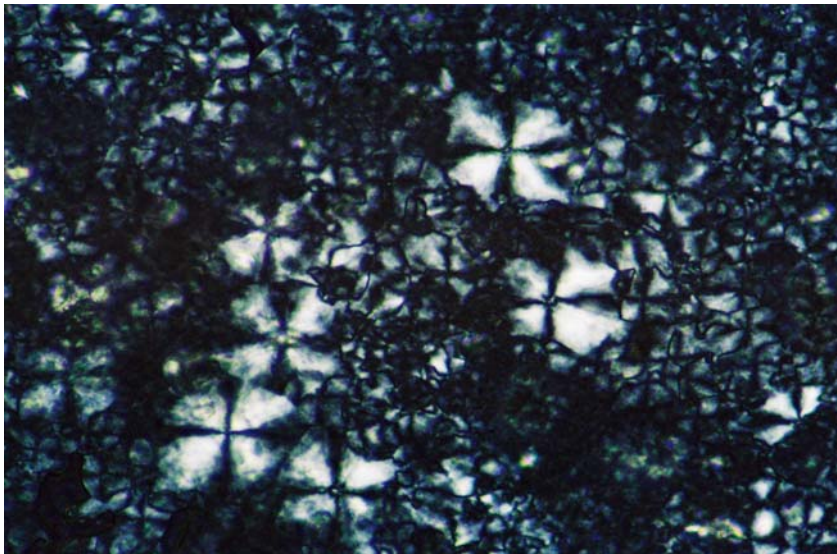


Figure 4.2.5: Optical Micrograph of PN1.5 crystallized at 152 °C. Magnification 32X



Figure 4.2.6: Optical Micrograph of PN5 crystallized at 152 °C. Magnification 32X

4.2.1.3 Thermal Properties-Differential Scanning Calorimetry

4.2.1.3.1 Melting and Non-Isothermal Crystallization

Table 4.2.2 presents the melting and crystallization temperature and degree of crystallinity of PVDF in PVDF/clay nanocomposites. The melting points of PVDF/20A composites are found to shift from 172 to about 178-180 °C (Table 4.2.1). The melting point of α form and β form are reported to be 172 and 178 °C respectively ⁽⁷⁾. The higher melting point of PVDF in the nanocomposites also suggests β form of PVDF.

The heat of fusion of PVDF is found to decrease marginally from 11.7 to 10.5 Cal/g. The decrease in the heat of fusion indicates lower extent of crystallinity of PVDF nanocomposites. The percentage crystallinity of PVDF can be calculated using value of heat of fusion for the 100 % crystalline PVDF as 25 Cal/g ⁽⁸⁾. The percentage crystallinity of PVDF decreases from 47 to 44 % on addition of clay as can be seen from the table 4.2.2. The addition of clay results in marginal decrease in the crystallinity of PVDF.

The non-isothermal crystallization curves show that PVDF in PVDF/clay nanocomposites crystallize at higher temperature (about 152 °C) relative to pristine PVDF (141 °C). Thus, a shift of about 10-11 °C in the non-isothermal crystallization

peak of PVDF indicates that the crystallization process is enhanced in presence of dispersed clay platelets. The degree of super cooling is also lower for PVDF nanocomposites as compared to PVDF indicating enhanced nucleation.

Table 4.2.2: Non-isothermal melting and crystallization parameters of PVDF and PVDF/20A nanocomposites

Sample identification	Melting Temperature, T_m ($^{\circ}\text{C}$)	Crystallization Temperature, T_c ($^{\circ}\text{C}$)	$\Delta T = (T_m - T_c)$ ($^{\circ}\text{C}$)	ΔH_f^* (Cal/g)	Crystallinity (%)
P	172	142	30	11.7	47
PN1.5	180	152	28	10.8	43
PN3	180	152	28	10.5	42
PN5	179	153	26	11.0	43
PN7	179	153	26	11.0	44

* ΔH_f values are normalized with respect to PVDF content

4.2.1.3.2 Isothermal Crystallization

Isothermal crystallization of PVDF and PVDF/20A nanocomposites is studied to find out the effect of clay on the isothermal crystallization behavior. Figure 4.2.7 illustrates the temperature dependence of crystallization half time ($t_{1/2}$) calculated using Avrami equation on crystallization temperature (T_c) for PVDF and nanocomposites. As is shown in the figure 4.2.7, over the temperature range studied, PVDF/clay nanocomposites exhibit a shift in the crystallization temperature to higher temperatures for all the nanocomposites. The crystallization process of PVDF in the nanocomposites is accelerated due to presence of clay, which acts as a nucleating agent⁽⁹⁾. Similar enhancement of crystallization has been reported in other polymer /clay nanocomposites⁽¹⁰⁾.

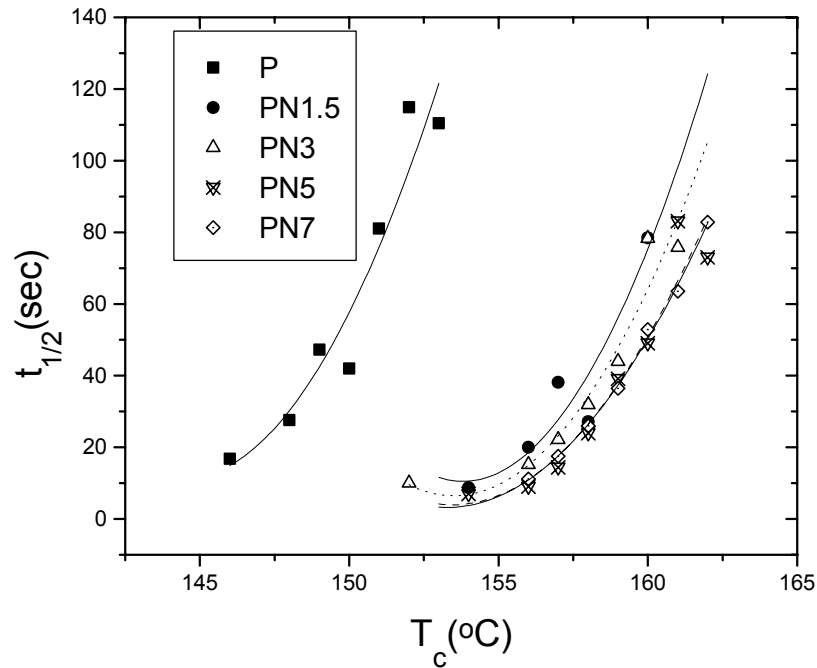


Figure 4.2.7: $t_{1/2}$ vs. T_c of PVDF/20A nanocomposites

4.2.1.4 Dynamic Mechanical Analysis

Figure 4.2.8 depicts the storage modulus of PVDF and PVDF/clay composites over a temperature range of -100 °C to 140 °C. As shown in the figure, PVDF nanocomposites show higher values of storage modulus over the entire temperature range of the study. The storage modulus increased with increase in clay content^(11, 12). Similar increase of dynamic storage modulus is reported for other polymer/clay nanocomposites^(9, 13).

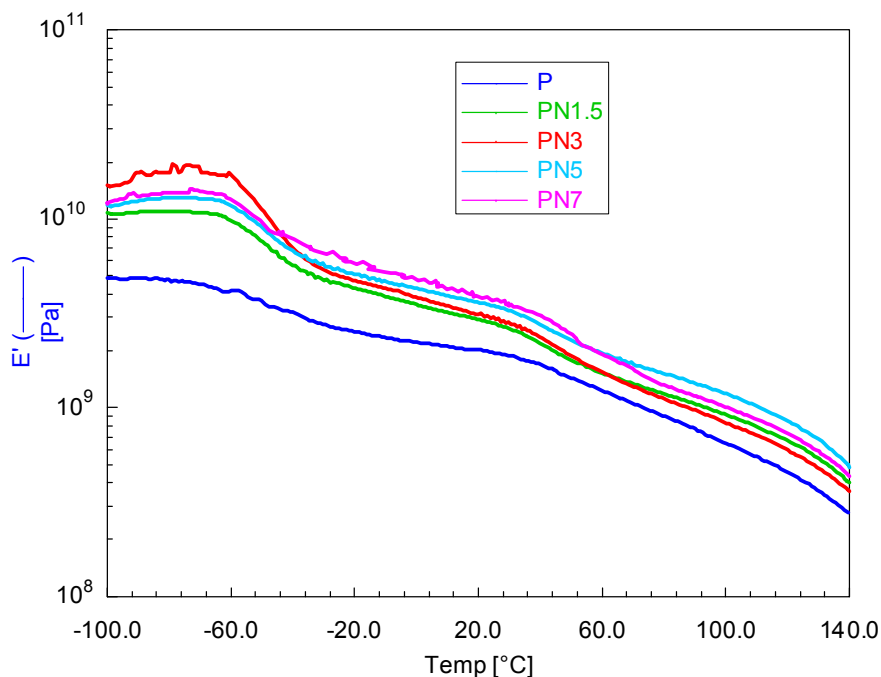


Figure 4.2.8: Temperature dependence of storage modulus (E') for PVDF and PVDF/20A clay nanocomposites

The effectiveness of clay as reinforcement can be elucidated as follows. The increase in the storage modulus of the nanocomposites is expressed in terms of the ratio of modulus of the composite (E_c') to the modulus of pristine polymer (E_p') and is shown in table 4.2.3. The increase in modulus for PN1.5 and PN7 is 40 and 84 % with respect to pristine polymer at room temperature. Even at high temperature i.e., at 100 °C well above the glass transition and crystalline transition temperature of the polymer, it is observed that the increase in modulus is about 56% for 7% clay content. The significant improvement in the storage modulus at temperatures higher than the glass transition and crystalline transition temperature of PVDF clearly confirms the reinforcing effect of clay in PVDF/clay nanocomposites. The enhancement in E' can be ascribed to the dispersion of clay layers and higher aspect ratio of the dispersed clay particles.

Table 4.2.3: E_c/E_p values of PVDF/20A at different temperatures

Sample code	E_c/E_p		
	At -100 °C	At 30 °C	At 100 °C
PN1.5	2.27	1.38	1.41
PN3	3.25	1.45	1.28
PN5	2.48	1.72	1.83
PN7	2.42	1.84	1.56

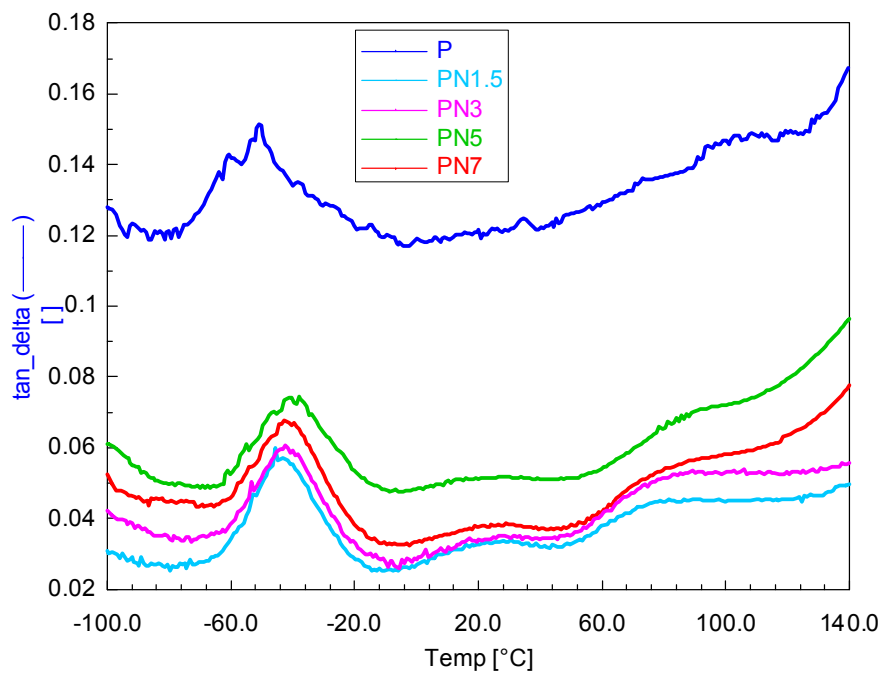


Figure 4.2.9: Tan δ vs. temperature curves for PVDF and PVDF/ 20A clay nanocomposites

Figure 4.2.9 shows the tan δ curves of PVDF and PVDF/clay nanocomposites. The tan δ curve shows a peak at about -50 °C for PVDF, which corresponds to the glass transition temperature of PVDF. In the case of PVDF/clay nanocomposites, the tan δ peak shifts to higher temperature by approximately 6-8 °C and the area under the tan δ peak decreases as can be seen from figure. The shift of

tan δ peak to higher temperature may be ascribed to hindered cooperative motion of polymer chains. Two more peaks are observed in the tan δ curves. The one at around 20 °C corresponds to the relaxation of restricted polymer chains and one at approximately 80 °C corresponds to the relaxation of crystal fraction.

4.2.1.5 Coefficient of Thermal Expansion

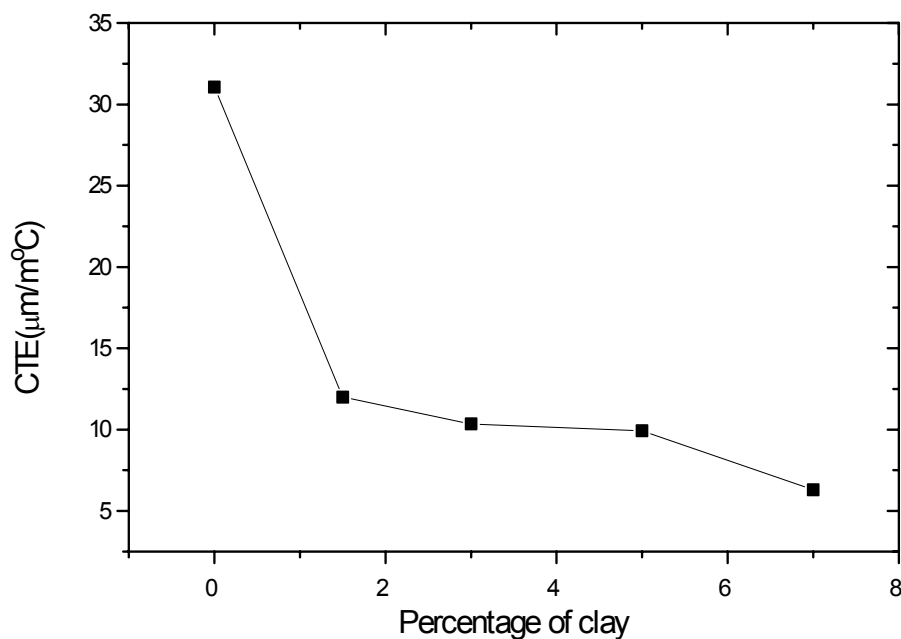


Figure 4.2.10: Variation of Coefficient of Thermal Expansion with percentage of clay for PVDF/20A nanocomposites

The nanocomposites are known to exhibit reduced thermal expansion coefficient and thus better dimensional stability as compared to the pristine polymer. Coefficient of thermal expansion (CTE) was measured over a temperature range of –100 °C to 140 °C. Figure 4.2.10 depicts the variation of CTE as percentage of clay. It can be seen from the Figure 4.2.10 that CTE decreases sharply by about 50 % at 1.5 % clay content. Further, increase in the clay content results in relatively small

decrease in CTE. The addition of clay platelets thus decreases the coefficient of thermal expansion significantly.

4.2.1.6 Melt Rheology

The storage modulus (G'), loss modulus (G'') and complex viscosity (η^*) as function of frequency for PVDF and PVDF/clay nanocomposites are shown in the figures 4.2.11-13.

The frequency dependence of G' decreases on addition of clay. The slopes of the G' curves are observed to decrease from the value 1.4 for the homo polymer as the percentage of clay increases to 0.73 for 7% clay content. The slope values are summarized in the table 4.2.4. It can be seen from the G' vs. Frequency curves that the PN behaves like pseudo-solids like in the case of PNC. The G'' slope is also observed to decrease in the case nanocomposites. The shear-thinning exponent of nanocomposites is also found to decrease.

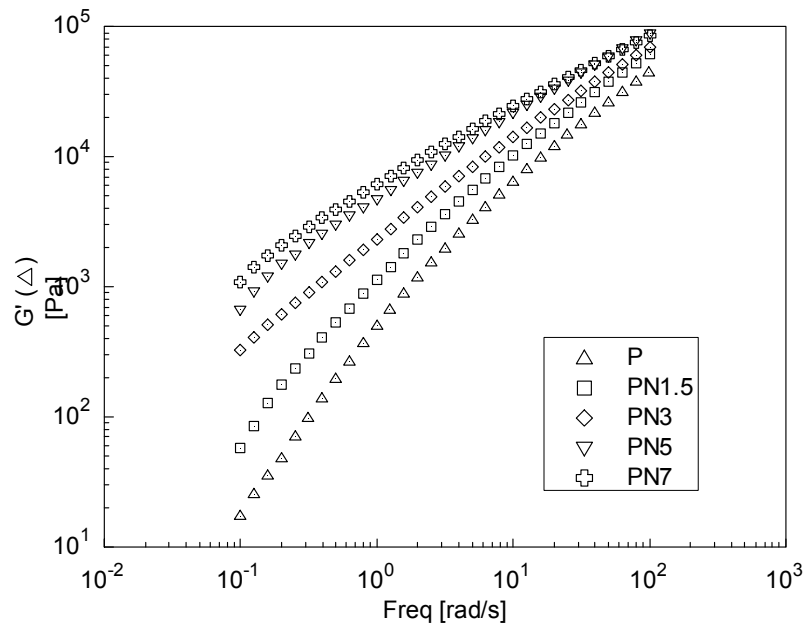


Figure 4.2.11: Frequency response of storage modulus (G') at 210 °C for PVDF/20A nanocomposites

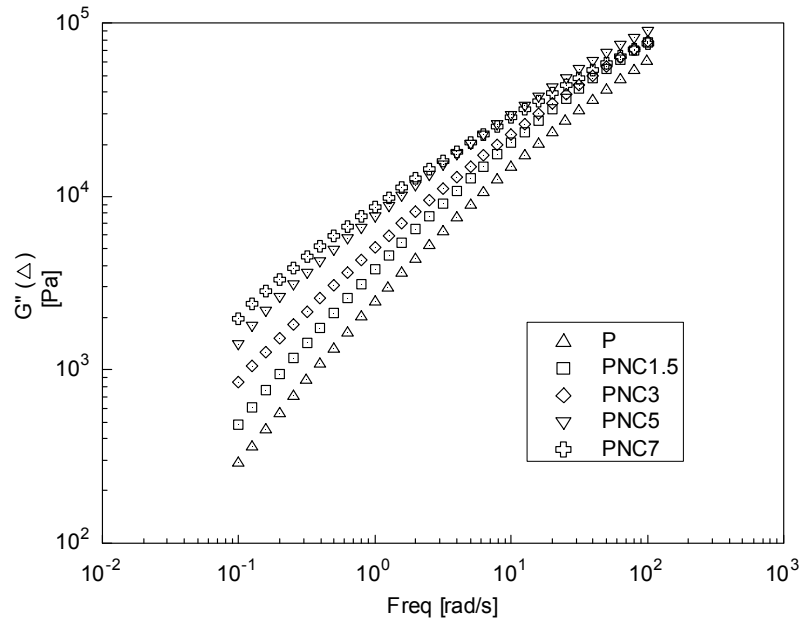


Figure 4.2.12: Frequency response of loss modulus (G'') at 210 °C for PVDF/20A nanocomposites

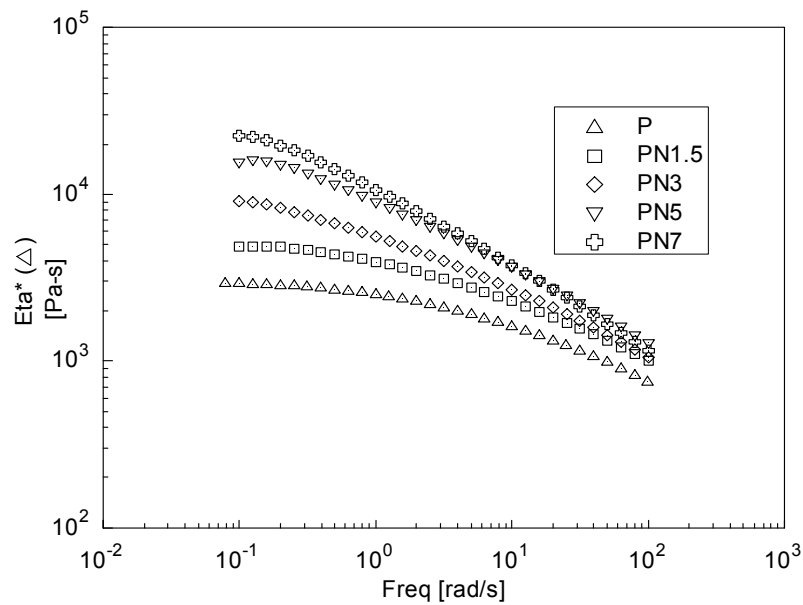


Figure 4.2.13: Frequency response of complex viscosity (η^*) at 210 °C for PVDF/20A nanocomposites

Table 4.2.4: Rheology- Low Frequency behaviour of PVDF/20A nanocomposites at 210°C

Sample	Slope of G'	Slope of G''	Slope of η^* (n)
P	1.4731	0.9682	-0.0449
PN1.5	1.2605	0.8900	-0.0951
PN3	0.8424	0.7694	-0.2198
PN5	0.7805	0.7417	-0.3021
PN7	0.7315	0.6358	-0.3371

The table 4.2.4 shows that the slopes of G' and G'' decreases and the magnitude of n increase with clay content. The higher G' and smaller slope of G' as compared to pristine PVDF indicates better interaction between the polymer and clay and formation of superstructure⁽¹⁴⁾.

The data obtained at 210, 220 and 230°C were used to obtain the master curves of PVDF and PVDF nanocomposites using TTS. Only a horizontal shift (a_T) was used for performing this, since there are no special features associated with the modulus data. It was fitted using Arrhenius equation and the graph so obtained was smoothened. There was a monotonic increase in the storage modulus with frequency. The non-terminal behavior observed in the nanocomposites could be a result of the retardation of molecular relaxation processes produced by the intercalation of polymer chains into the clay layers and hence entanglement or physical cross linking of the polymer chains to the clay surface. As in the case of other nanocomposites the Time Temperature Superposition principle is found to be valid in this case also^(15, 16).

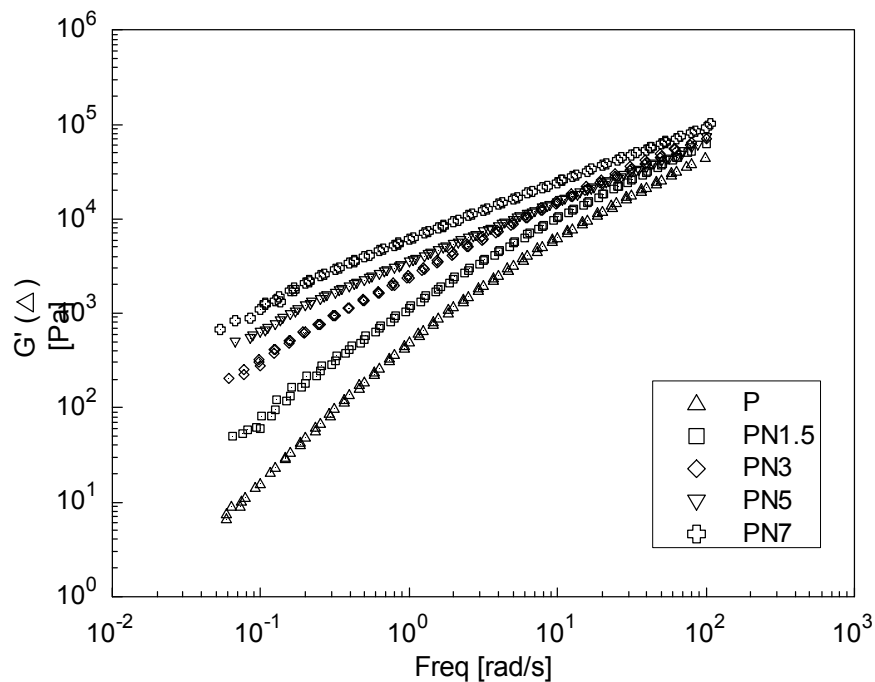


Figure 4.2.14: Master curve overlay of storage modulus (G') of PVDF and PVDF/20A shifted to 210 °C

4.2.1.7 Dielectric Properties

The ϵ' vs. frequency curves for the pristine PVDF and the nanocomposites are shown in the figure 4.2.15.

It is seen that ϵ' is high at low frequencies and decreases as the frequency increases. It was observed that the ϵ' decreases in the whole range of frequencies with clay content except in the case of 1.5% clay at low frequencies. At low frequencies the slope of the curve increases because of the ionic dc conductivity that might have been increased due to the presence of organically treated clay. The decrease in the ϵ' can be attributed to the mobility decrease in the nanocomposite as compared to the pristine polymer matrix due to clay acting as hindrance to dipole orientation. This mobility reduction decreases charge separation and therefore reduces the dielectric constant⁽¹⁷⁾.

It has been observed by many researchers that there is an increase in the ϵ' on formation of the β phase, but the constraints produced due to the nanocomposite formation causes the reduction in ϵ' at all frequencies in PVDF/20A nanocomposites.

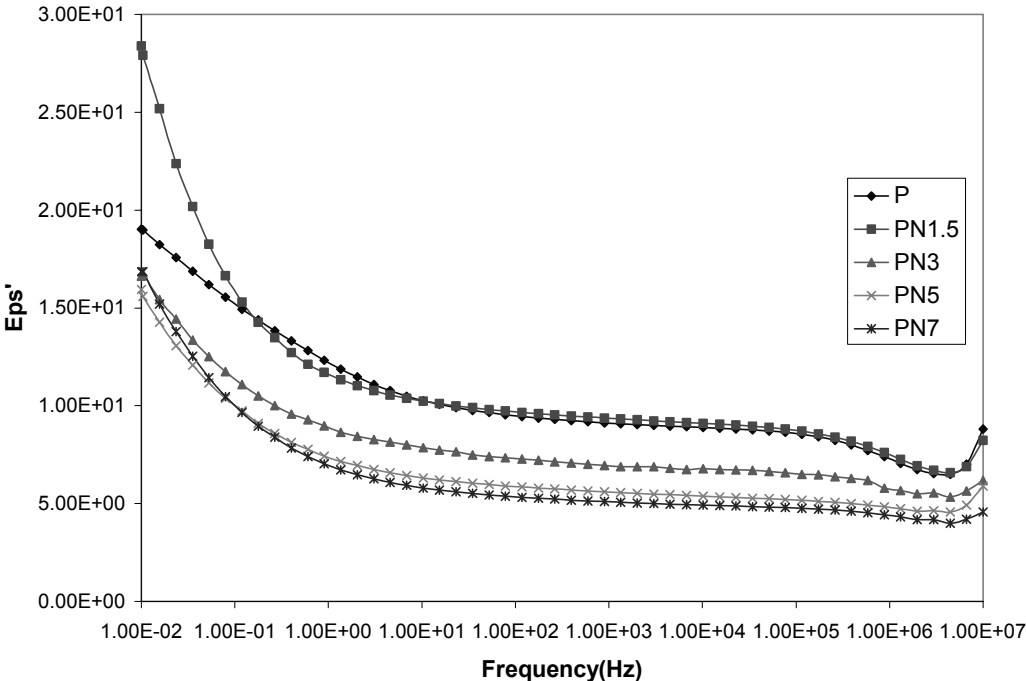


Figure 4.2.15: Comparison of dielectric constant (ϵ') of PVDF/20A nanocomposites

As can be seen from the figure 4.2.16, there are two relaxations corresponding to the ϵ'' for pristine PVDF, the low frequency α relaxation and high frequency β relaxation. β relaxation is due to the glass transition mechanism, but the α relaxation is associated with the molecular motions within the crystalline fraction. In the case of nanocomposites, which is observed to be in the β phase, only the relaxation during glass transition is observed. The α relaxation is observed in the case of α phase PVDF only ⁽¹⁸⁾. Moreover, it is observed that the ϵ'' increases at low frequencies due to ionic conductivity.

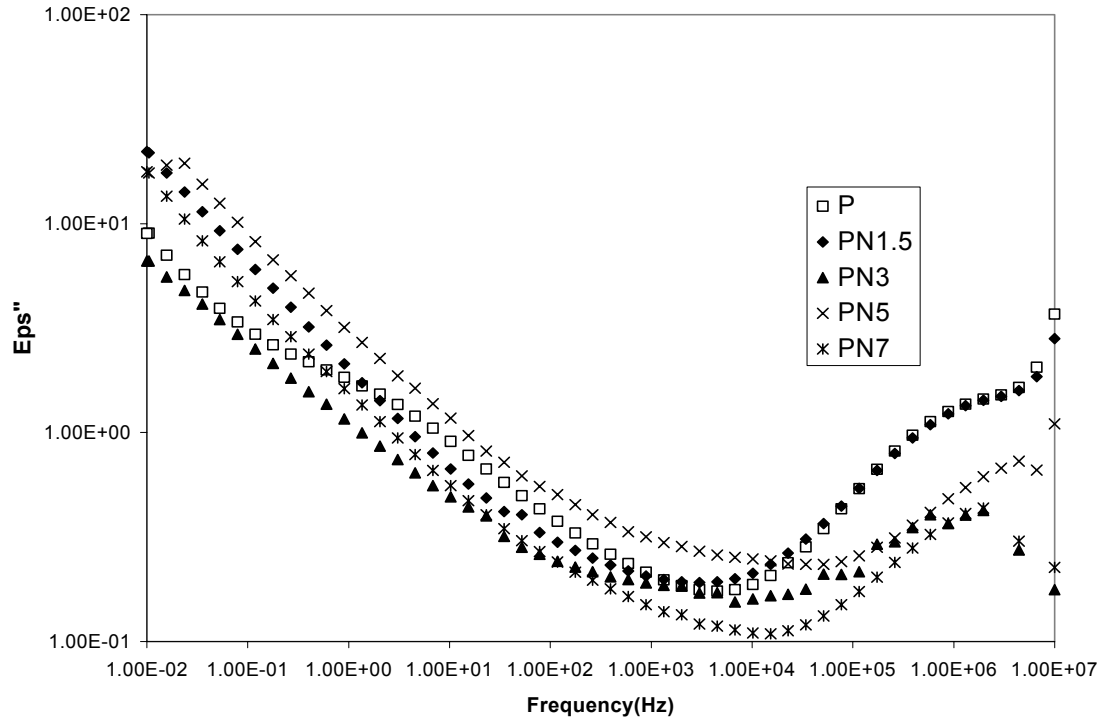


Figure 4.2.16: Comparison of loss factor (ϵ'') of PVDF/20A nanocomposites

It can be summarized that the ϵ' decreases in the nanocomposites and only β relaxation is observed in the nanocomposites.

4.2.1.8 Stability of β Phase in PVDF/20A Nanocomposites

As in the case of PVDF/6A thermal annealing at 125 °C (solid state annealing) and 185 °C (melt state annealing) was carried out for PVDF/20A nanocomposites. The XRD data is used as a tool, for analyzing the stability of the PVDF β phase.

In the figure 4.2.17, P corresponds to the Pristine PVDF and PN corresponds to the PN5. All the other nanocomposites also exhibit a similar behavior. The presence of β phase in all annealed samples confirms the stability of β phase.

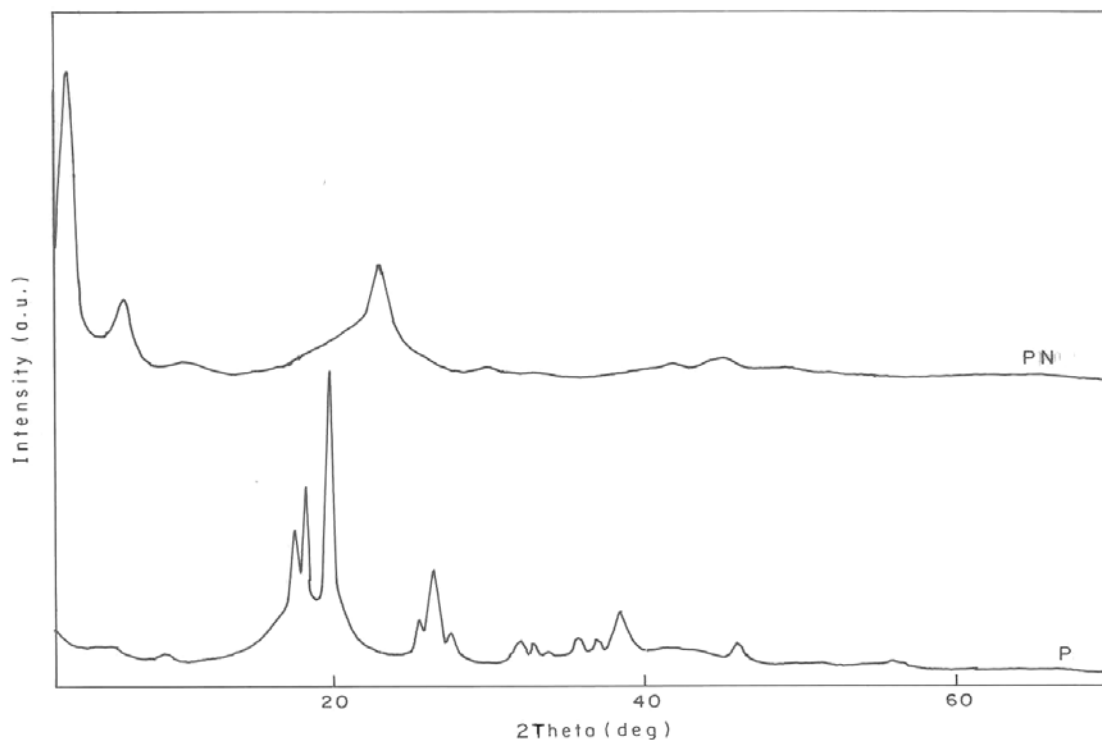


Figure 4.2.17: XRD of retention of PVDF and PN5 after annealing at 185°C showing α phase for PVDF and β phase for PN5

4.3 Effect of Modifier Treatment

PVDF intercalated nanocomposites were obtained by using ditallow dimethyl ammonium treated clays viz., 6A and 20A. It was observed that the intercalation of PVDF into the clay layer leads to change in crystal structure and morphology, and improved dynamic mechanical properties. The organic treatment facilitates the intercalation process in polymer clay nanocomposites. To confirm the effect of organic treatment in the intercalation process untreated clay Na^+ is used to prepare composites of PVDF. The composite was prepared using identical conditions of melt compounding and the clay content was 5% by weight.

4.3.1 Results and Discussion

4.3.1.1 Structure of Composites

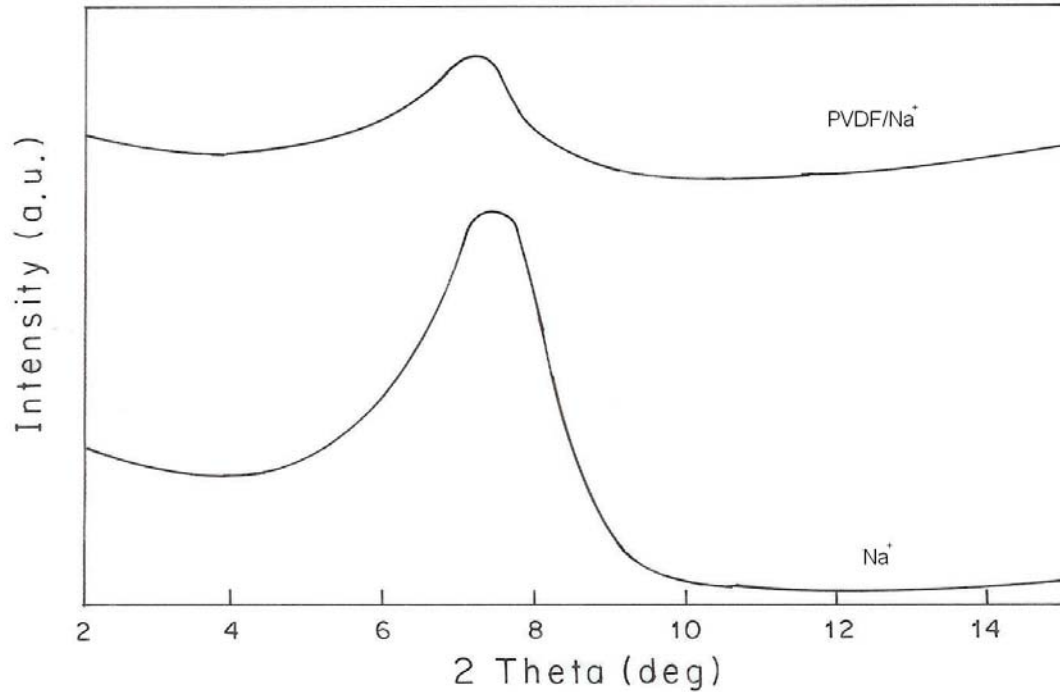


Figure 4.3.1: XRD of Na⁺-clay (a) and PVDF/Na⁺ composite (b)

With Na⁺ Montmorillonite, there was no change observed in the basal reflections. Both Na⁺ montmorillonite as well as the composite were having a d spacing of approximately 1.1 nm, which proves the lack of interaction of the polymer in clay layers and thus forms a microcomposite. In contrast, 20A nanocomposite shows a shift to higher d spacing. The d_{001} spacing is of the order of 3.3 nm where as in the case of 6A d_{001} is observed at 2.84 nm formed after rearrangement of the clay layers. This difference in the final d spacing so formed could be attributed to the amount of polymer that has entered inside the gallery spacing.

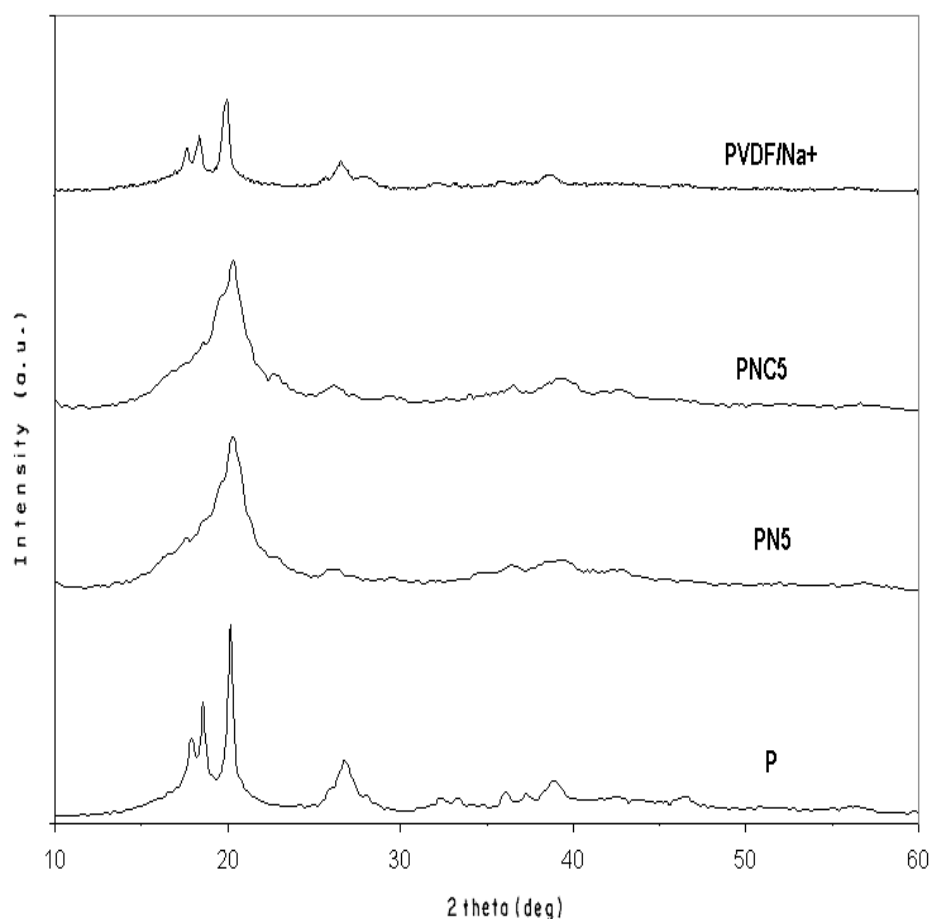


Figure 4.3.2: XRD of PVDF, nanocomposites PNC5, PN% and PVDF/Na⁺ showing α phase in PVDF and PVDF/Na⁺ and β phase in PN5 and PNC5

The XRD of untreated clay (Na⁺) hybrid along with other nanocomposites is as shown in Figure 4.3.2. PVDF crystallizes only in α phase in Na⁺ clay hybrid and secondly there is no shift in d_{001} peak of Na⁺ clay, which has already been shown. This indicates that in the micro composite (PVDF/Na⁺), PVDF does not crystallize in β phase. This result confirms that the β phase observed in PVDF/clay nanocomposite is not just because the presence of clay but because of nanoscale interaction between the polymer and organically modified clay

4.3.1.2 Morphology- Optical Microscopy

Figure 4.3.3 shows optical micrograph of pristine PVDF. PVDF is observed to crystallize in a normal, large, isotropic spherulitic morphology. On full growth,

the spherulites are observed to impinge upon each other. PVDF/Na⁺ (figure 4.3.4), which forms a micro composite, the spherulitic structure of PVDF is retained. However, the size of spherulites is smaller. This is due to the nucleating effect of the clay filler. In the case of nanocomposites, as was seen previously, the size of the spherulites decreases significantly in PN and PNC nanocomposites. Shah et al ⁽¹⁹⁾ also made similar observations in case of PVDF/Clay nanocomposites.

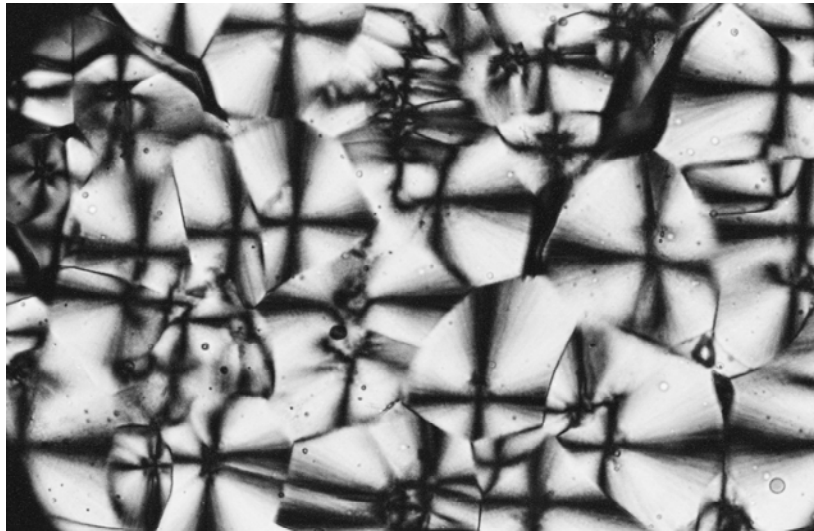


Figure 4.3.3: Optical Micrograph of PVDF crystallized at 148 °C. Magnification 32X

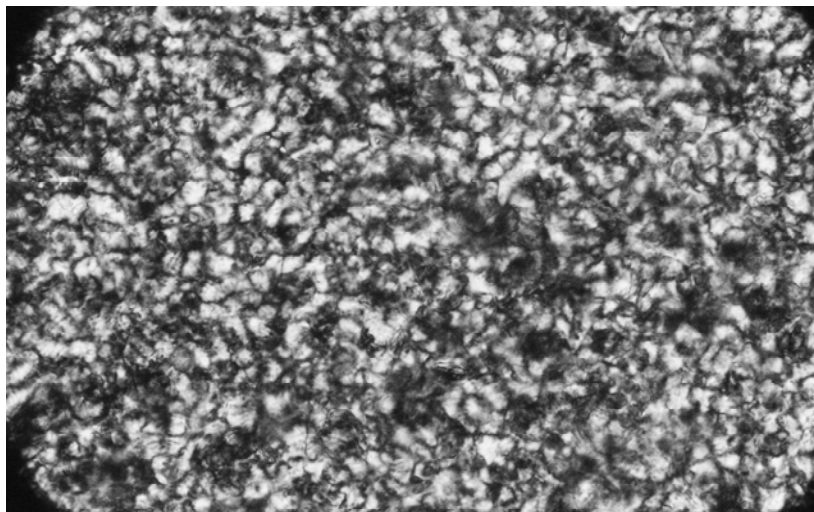


Figure 4.3.4: Optical Micrograph of PVDF/Na⁺ crystallized at 148 °C. Magnification 32X

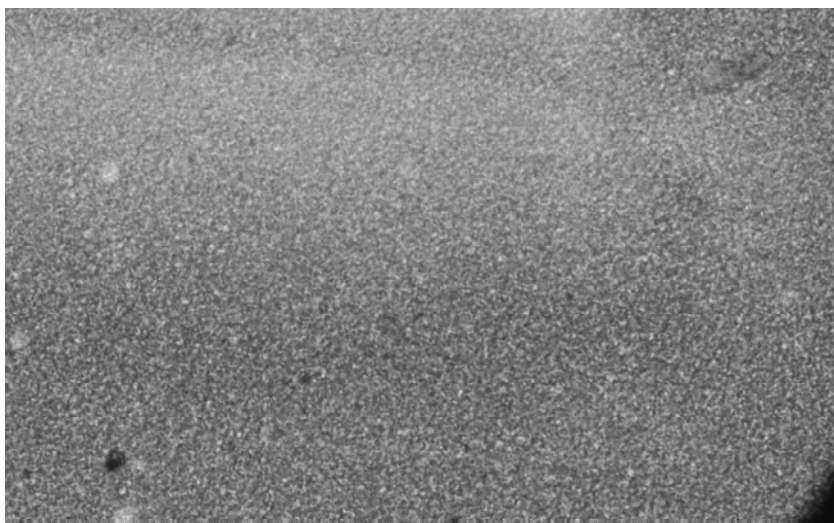


Figure 4.3.5: Optical Micrograph of PNC5 crystallized at 152 °C. Magnification 32X



Figure 4.3.6: Optical Micrograph of PN5 crystallized at 152 °C. Magnification 32X

4.3.1.3 Thermal Properties- Differential Scanning Calorimetry

4.3.1.3.1 Melting and Non-isothermal Crystallization

The melting and crystallization behavior of polymer and composites were studied using DSC. The melting point and heat of fusion were determined from the heating scans while the crystallization temperature and heat of crystallization were determined from the cooling scans.

The as received polymer was observed to melt at a temperature of 174 °C where as the melting point of the melt mixed sample was observed to be 172 °C. Composite with 6A and 20A were observed to have melting points of 181 °C, and 179 °C respectively. A shift in the crystallization temperature from 141 to 152 and 154 °C was observed during cooling in the PVDF clay composite with 6A, and 20A respectively. No shift in melting and crystallization. This implies that β phase is not observed in the case of PVDF/Na⁺. Temperature was observed for Na⁺. The crystallinity of PVDF/Na⁺, PNC5 and PN5 are 41, 38 and 43% respectively.

4.3.1.3.2 Isothermal Crystallization

Figure 4.3.7 illustrates variation of $t_{1/2}$ with crystallization temperature for PVDF, nanocomposites and the microcomposite PVDF/Na⁺.

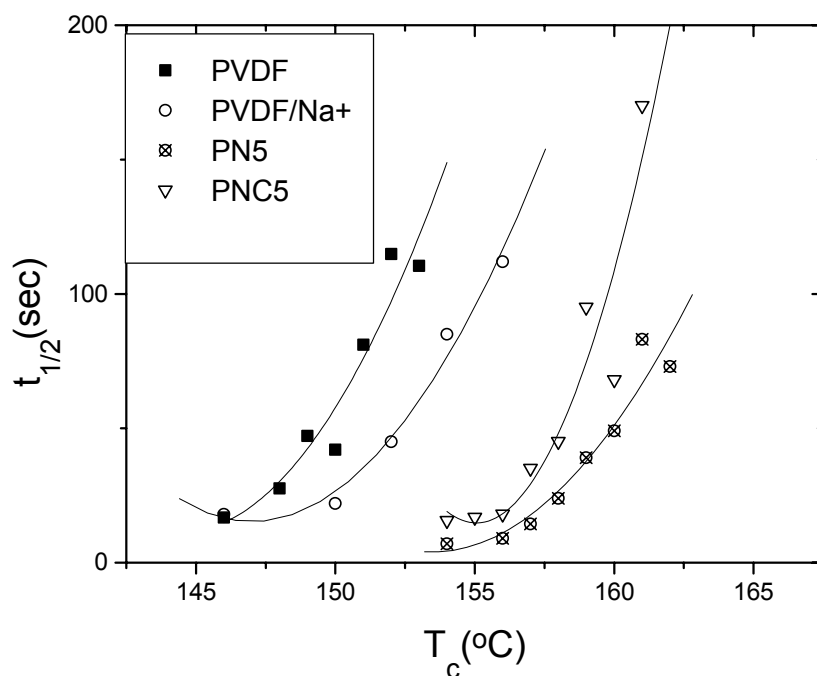


Figure 4.3.7: Isothermal crystallization of PVDF and PVDF/clay composites

It is observed that the nanocomposites of PVDF/6A and PVDF/20A namely PNC5 and PN5 crystallize at higher temperature due to enhanced nucleation process of PVDF in the nanocomposites. The micro composite PVDF/Na⁺ crystallizes at slightly higher temperature than those for the pristine polymer. The results thus

indicate that the extent of enhanced crystallization is more for the nanocomposites than that observed in the microcomposite with Na^+ .

4.3.1.4 Dynamic Mechanical Analysis

The temperature dependence of storage modulus for PVDF and the composites is shown in figure 4.3.8.

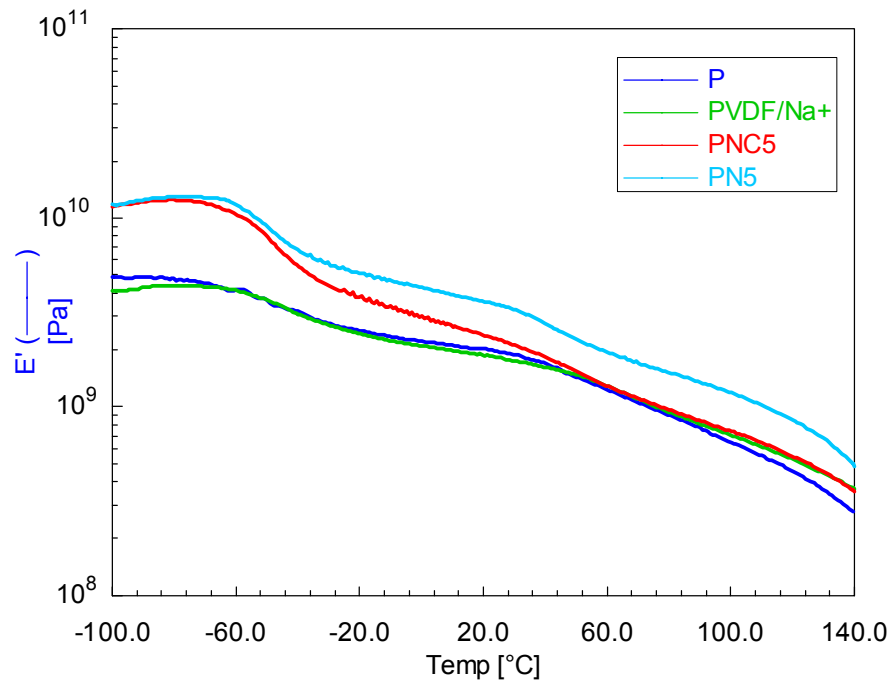


Figure 4.3.8: Temperature dependence of storage modulus (E') for PVDF and PVDF composites with Na^+ , 6A, 20A

The dynamic mechanical analysis indicated an increase in E' as compared to the as received polymer for the composites (Figure 4.3.8). The extent of increase has a pattern of $\text{PVDF}/20\text{A} > \text{PVDF}/6\text{A} > \text{PVDF}$. Increase PVDF/Na^+ as compared to the pristine polymer is almost negligible and might be attributed to the filler effect. The increase in the storage modulus of the nanocomposites is expressed in terms of the ratio of modulus of the composite (E'_c) to the modulus of pristine polymer (E'_p). Table 4.3.1 shows the E'_c/E'_p for the composites at three different temperatures.

Table 4.3.1: E_c/E_p values of PVDF/clays (Na^+ , 6A, 20A) at different temperatures

Sample identification	E_c/E_p		
	At $-100\text{ }^\circ\text{C}$	At $30\text{ }^\circ\text{C}$	At $100\text{ }^\circ\text{C}$
PVDF/ Na^+	0.85	0.95	1.09
PNC5	2.36	1.13	1.15
PN5	2.48	1.72	1.83

As can be seen from the table, the composite with Na^+ show little change while the nanocomposite shows significant increase in the storage modulus over the entire temperature range. The reinforcing effect of the clay layers is thus observed in the nanocomposites whereas the Na^+ clay does not contribute to the modulus.

4.3.1.5 Linear Rheology

Linear rheology of PVDF/clay nanocomposites were carried out using stress controlled ARES rheometer. Figure 4.3.9 represents the dynamic frequency sweep of PVDF and its composites with Na^+ , 6A and 20A at 5% by weight of clay loading.

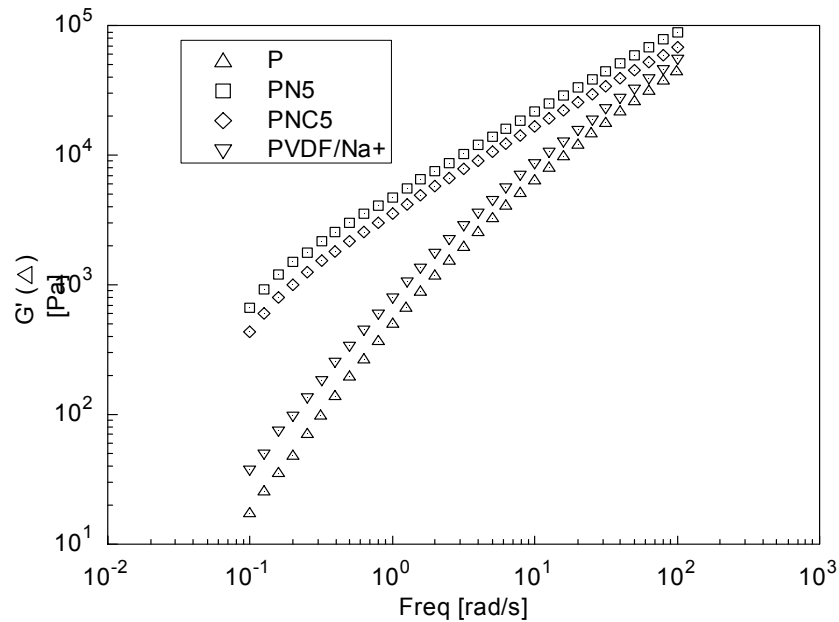


Figure 4.3.9: Frequency response of storage modulus (G') at $210\text{ }^\circ\text{C}$ for PVDF nanocomposites (PVDF/6A, PVDF/20A and micro composites PVDF/ Na^+)

Table 4.3.2: Rheology- Low frequency behaviour of PVDF/clays (Na⁺, 6A, 20A) composites at 210 °C

Sample	Slope of G'	Slope of G''	Slope of η^* (n)
PVDF	1.4731	0.9682	-0.0449
PVDF/Na ⁺	1.3382	0.9471	-0.0588
PNC5	0.8856	0.7561	-0.2497
PN5	0.7805	0.7417	-0.3021

In the terminal region pristine polymer and the composites exhibit the classical viscoelastic behavior viz., $G'' > G'$. The values of the slopes for the polymer and the composites are summarized in the table 4.3.2. It can be seen from the table that the slopes of G' and G'' for the nanocomposites decreases significantly whereas for the microcomposite PVDF/Na⁺ the slope modification is negligible. 'n' for PVDF/Na⁺ composite is closer to that of PVDF where as for the nanocomposite it decreases significantly. In the modified clays, it decreases and a minimum value is observed for PVDF/20A. This indicates that the shear thinning increases on addition of the clay⁽¹⁹⁾. Increase in G' and decrease in the slope of G' as compared to the pristine PVDF and PVDF/Na⁺ indicate superstructure formation⁽¹⁴⁾. It has been shown by Wagener et al⁽²⁰⁾ that well exfoliated samples display higher magnitude of 'n' while absence of exfoliation results in 'n' closer to zero. The values closer to zero in the case of PVDF/Na⁺ sample indicates the absence of intercalation or exfoliation.

4.3.1.6 Dielectric Properties

While studying the dielectric properties of the PVDF/20A nanocomposites, the effect of both the nanocomposite formation as well as the β formation has to be taken into consideration.

The dielectric properties of PVDF/6A, PVDF/20A and PVDF/Na⁺ at 5-weight % of clay are compared to study the properties of nanocomposites and microcomposite (Figure 4.3.10). It is known that the clay tactoids act as hindrance to dipole orientation. As the clay cluster size increases because of poor dispersion, there is more free polymer, which can orient itself to the applied field. Therefore better

intercalation and dispersion reduces the mobility of the polymer. This effect can be seen while comparing the effects of the three clays, viz., 20A, 6A, and Na^+ . The Na^+ clay, which forms a microcomposite with PVDF, has a higher dielectric constant as compared to 6A and 20A nanocomposite. 20A clay, which forms a good intercalated nanocomposite as compared to 6A, has a lesser dielectric constant. Hence, the measurement of dielectric constant can qualitatively be used as a parameter for comparing the structure of nanocomposites.

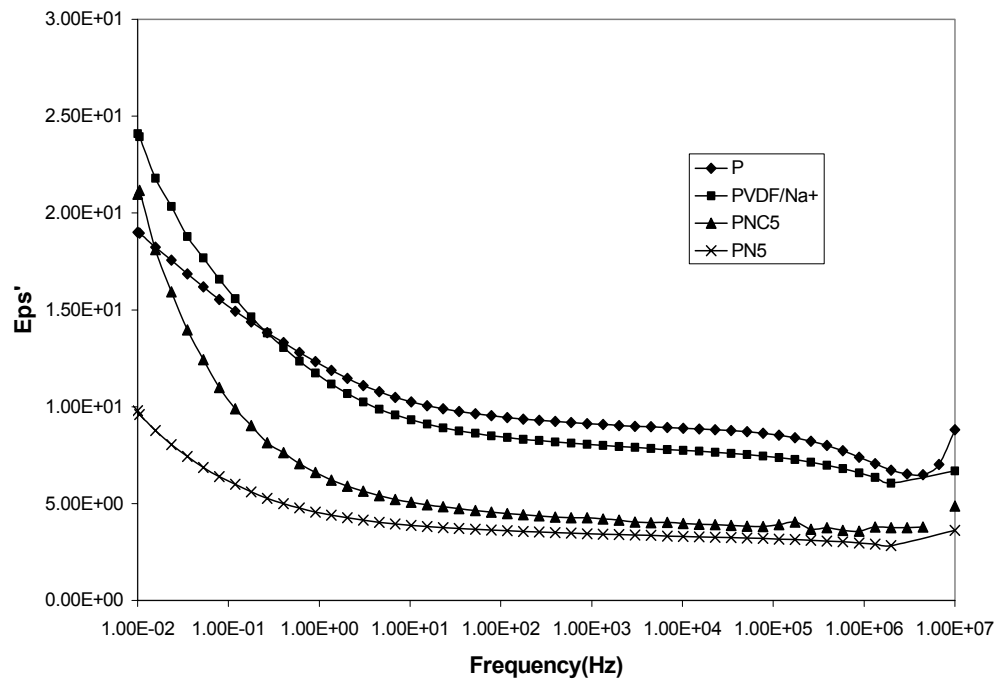


Figure 4.3.10: Comparison of dielectric constant (ϵ') of PVDF, nanocomposites PVDF/6A, PVDF/20A and micro composite PVDF/ Na^+

Figure 4.3.11 shows the ϵ'' vs. frequency curves of PVDF, nanocomposites PVDF/6A, PVDF/20A and microcomposite PVDF/ Na^+ . As can be seen from the figure 4.3.11, there are two relaxations corresponding to the ϵ'' of pristine PVDF, the low frequency α relaxation and high frequency β relaxation. β relaxation is due to the glass transition mechanism, but the α relaxation is associated with the molecular motions within the crystalline fraction. In the case of nanocomposites, which is observed to be in the β phase, only the β relaxation is observed. The α relaxation is

observed in the case of α phase PVDF only ⁽¹⁷⁾. It is also observed that the ϵ'' increases at low frequencies. In PVDF/Na⁺ microcomposite α relaxation similar to that of pristine PVDF is observed. Hence it can be concluded that there is no β phase formation.

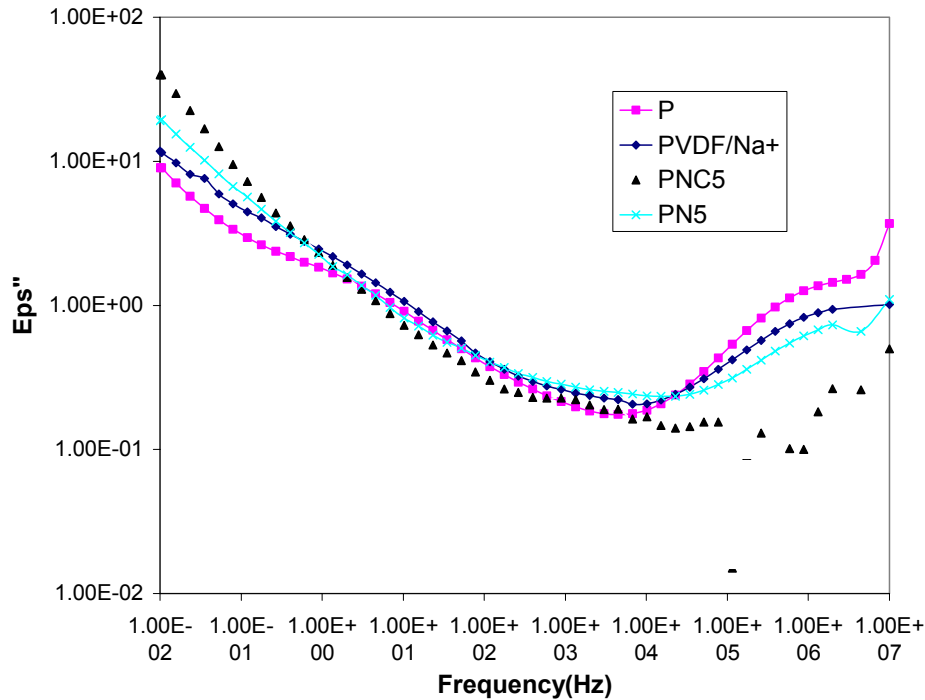


Figure 4.3.11: Comparison of loss factor (ϵ'') of PVDF, nanocomposites PVDF/6A, PVDF/20A and micro composite PVDF/Na⁺

4.4 Effect of Modifier Concentration

The intercalation of PVDF chains into the space between the silicate galleries depends upon the amount of clay layers available and the amount of organic treatment.

Sukpirom et al ⁽²²⁾ suggested that the intercalation yield could be calculated as

$$\chi_t = [I(001)_{nano} + I(002)_{nano}] / [I(001)_{clay} + I(001)_{nano} + I(002)_{nano}] \quad (4.1)$$

Here $I(001)_{nano}$ and $I(002)_{nano}$ represents the intensity of 001 and 002 peaks of the nanocomposites and $I(001)_{clay}$ represents the intensity of 001 peak of the organically treated clay used.

The intercalation yield for the nanocomposites is calculated according to the formula used by Sukpirom et al and is given in Table 4.4.1.

Table 4.4.1: Comparison of intercalation yield of 20A and 6A nanocomposites

Clay Percentage (%)	χ_t for PVDF/6A (%)	χ_t for PVDF/20A
1.5	18	40
3	30	65
5	10	79
7	15	87

The values of intercalation yield for 6A do not show any dependence on the clay content whereas for 20A there is a systematic increase in intercalation yield. The values of intercalation yield calculated for PVDF/20A nanocomposites are very much higher as compared to those for PVDF/6A nanocomposites. This observation is interesting as the organic moiety used to modify both the clays is identical and thus would result in identical interaction with the polymer. The only difference is in organic content and the d spacing. The amount of intercalant and length of organic chains determine the initial d spacing. The increased d spacing in case of 6A clay is presumably due to the higher inter layer packing density⁽²³⁾. The higher packing density in 6A seems to hamper the intercalation of polymer chains in the inter layer and thus results in lower intercalation yield. In case of 20A, the intercalation seems to be less hampered as compared to 6A. This could be due to lower packing density in 20A. The lesser amount of organic content in between the interlayer allows better interaction between the clay layer and the polymer and thus facilitates diffusion of the polymer chains within the interlayer spacing. The observed increase in the interlayer distance and an increase in the intercalation yield in PVDF/20A nanocomposites can thus be attributed to the lower packing density of the organic chains in the organically modified clay. These observations are consistent with the prediction made by Balazs et al⁽²⁴⁾ that an optimal value of organic modifier is required in order to obtain a good intercalated nanocomposite.

Increase in the dynamic modulus at different temperatures can also be used as a parameter for comparing the nanocomposites. The ratio of dynamic modulus of the composite with respect to pristine polymer (E_c'/E_p') is given in the table 4.4.2.

Table 4.4.2: E_c'/E_p' with respect percentage at room temperature

Percentage of clay (%)	E_c'/E_p' at 30 °C	
	PVDF/ 6A	PVDF/ 20A
1.5	1.0	1.38
3	1.0	1.45
5	1.125	1.72
7	1.40	1.84

The E_c'/E_p' values for PVDF/20A nanocomposites are higher than that for PVDF/6A nanocomposites. The higher values can be attributed to the higher intercalation yield observed in case of PVDF/20A nanocomposites with respect to PVDF/6A nanocomposites. The reinforcement observed in the dynamic storage modulus can be further explained on the basis of Guth's theory. The modulus of the composites containing non-spherical fillers is given by

$$E_c = E_m(1 + 0.67f_g v_f + f_g^2 v_f^2) \quad (4.2)$$

where E_c is the modulus of the composite, E_m is the modulus of the matrix, f_g is ratio of filler particle length to width or the apparent aspect ratio, and v_f is the filler volume fraction. The apparent aspect ratio calculated using Guth's equations⁽²²⁾ are presented in table 4.4.3.

The intercalation of a polymer in the silicate layers results in an increase in the active surface area of the filler. Polymer chains confined to the silicate layers are immobilized. Thus, intercalation also increases the effective volume. The effective immobilization of these chains is thought to make them more a part of the filler rather than that of the polymer as is shown in the schematic figure 4.4.1.

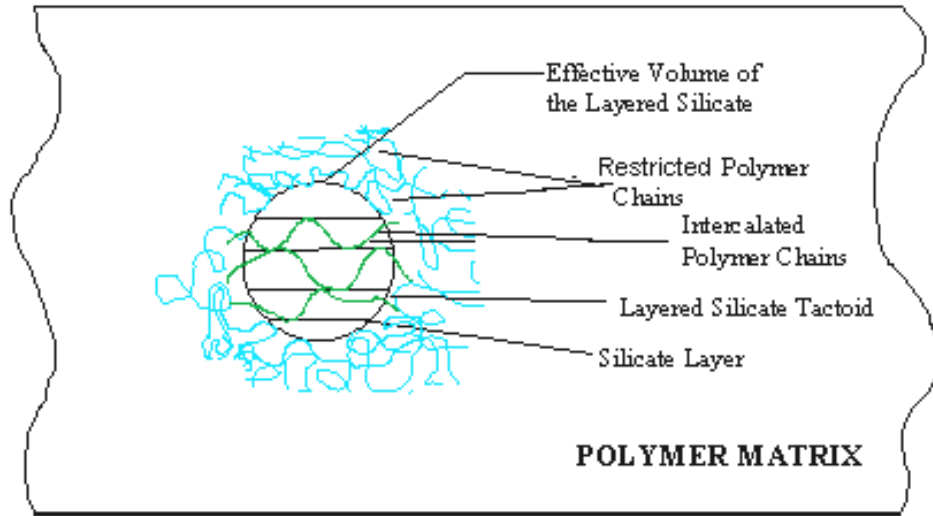


Figure 4.4.1: Schematic representation of formation of intercalated PLS nanocomposite – polymer chains have infiltrated the silicate layers increasing the effective volume on the layered silicate.

To elucidate the contribution of the effective volume fraction, an approach similar to the one discussed by Lim et al⁽²³⁾ was employed. The polymer intercalated to the clay layers together with the clay layers, forms the effective volume fraction of the clay, and is considered to be having a disk shape. Each disk is considered to be circular with radius R and thickness $2a$. The average number density of the disk is considered to be n . Therefore, the average volume fraction of the disk is

$$\phi = 2\pi a R^2 n \quad (4.3)$$

The disk radius to thickness aspect ratio is denoted by

$$\alpha = \frac{R}{2a} \quad (4.4)$$

The effective volume concentration of clay will be

$$nR^3 = \frac{\phi\alpha}{2\pi} \quad (4.5)$$

The effective volume fraction of the clay was calculated using the calculated values of apparent aspect ratio (f_g) calculated using Guth's equation and volume fraction of clay (Table 4.4.3).

As can be seen, effective volume fraction of the clay is greater than the initial volume fraction of the treated clay used. The clay particles can thus form relatively higher concentration regions, which could account for the higher modulus of the nanocomposites. This increase in the effective clay volume fraction and the increase in the apparent aspect ratio of the clay are accountable for the observed increase in the dynamic storage modulus ⁽²³⁾. However, a comparison of effective storage modulus of PVDF/6A and PVDF/20A nanocomposites shows that the extent of increase in the effective volume and aspect ratio are not similar. The 6A nanocomposites have a value lesser than the 20A nanocomposites, which when combined with the earlier result of intercalation yield implies that the PVDF/20A forms a better nanocomposites as compared to PVDF/6A.

Table 4.4.3: Aspect ratio (f_g) and calculated volume concentration of PVDF/6A and PVDF/20A nanocomposites

Clay Percentage (%)	f_g		Volume concentration			
	PVDF/6A	PVDF/20A	PVDF/6A		PVDF/20A	
			Calculated volume	Effective volume	Calculated volume	Effective volume
1.5	7	20	0.010	0.0229	0.0151	0.0955
3	2	15	0.020	0.0215	0.0302	0.1433
5	5	10	0.033	0.053	0.0503	0.175
7	7	7	0.047	0.103	0.0704	0.1559

*Calculated Volume is obtained form weight fraction and density of polymer and clay.

From all these aspects it can be seen that 20A is forming a good nanocomposite as compared to 6A.

4.5 PVDF/20A Extruded Nanocomposites

In this section, PVDF SOLEF 1008 nanocomposites is prepared by extruding the samples in a twin-screw extruder. This is done in order to check the nanocomposite formation under various methods of preparation. It is to be noted that the temperature profile, shear produced etc., while mixing the sample in a Brabender

plasticorder batch mixer and twin screw extruder are entirely different. Hence, this study is important from the point of view of industrial applications.

The samples are coded as TPN for Twin screw extruded PVDF/20A and the number corresponds to the weight percentage of organically treated clay (20A) in it.

4.5.1 Results and Discussion

4.5.1.1 Structure of Nanocomposites- X-Ray Diffraction

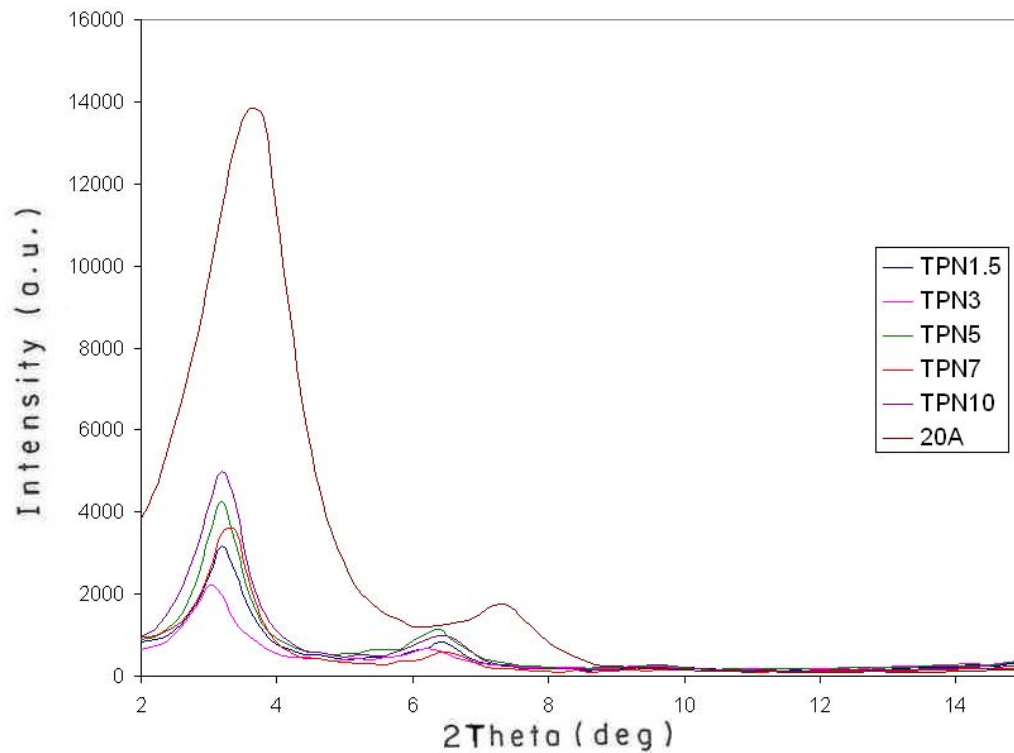


Figure 4.5.1: XRD of 20A and PVDF (SOLEF 1008)/20A extruded nanocomposites

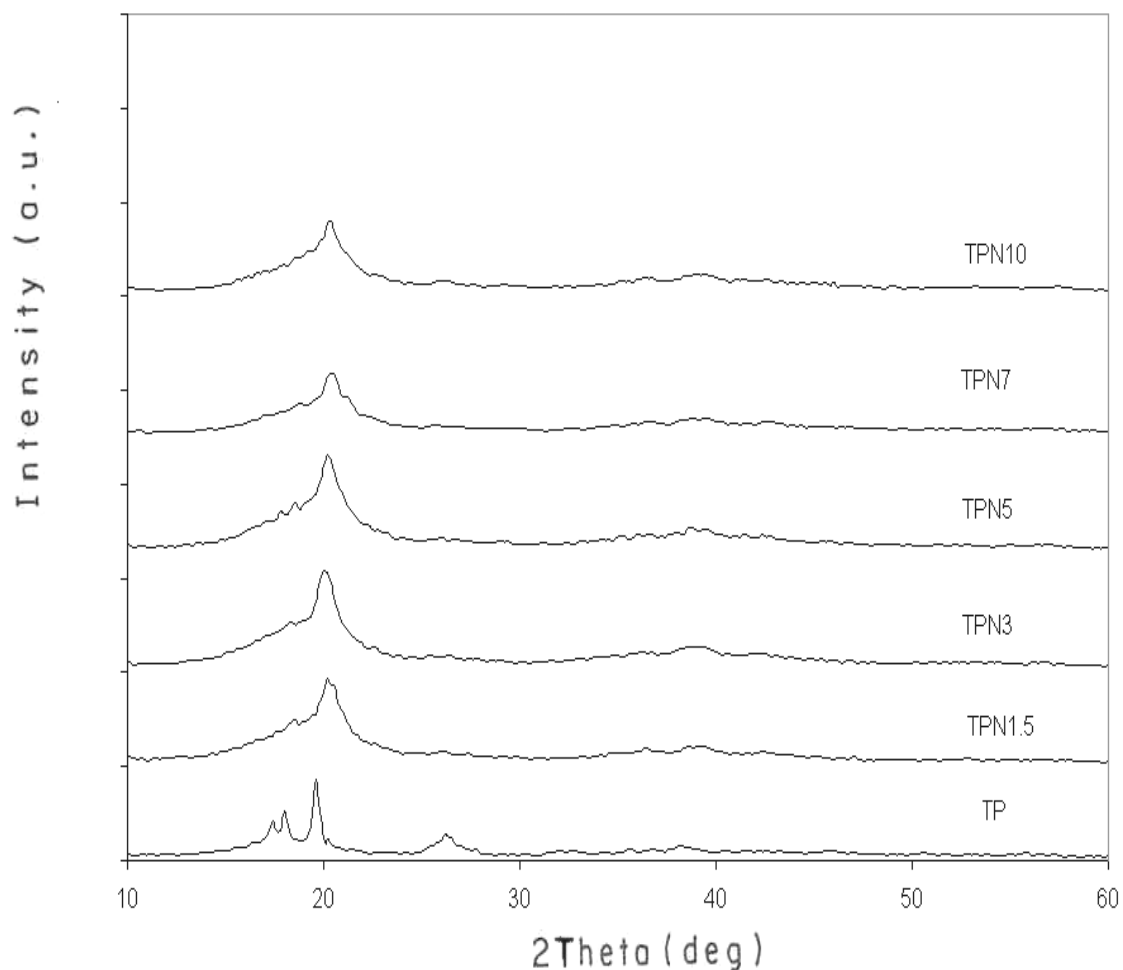


Figure 4.5.2: XRD showing α phase of pristine PVDF (SOLEF 1008) and β phase of PVDF (SOLEF 1008) in PVDF (SOLEF 1008)/20A extruded nanocomposites

The figures 4.5.1 and 4.5.2 show the intercalated structure as well as the formation of the β phase of the twin-screw extruded nanocomposite respectively. The d_{001} spacing of nanocomposite containing 1.5, 3, 5, 7 and 10 weight % 20A is 2.72, 2.89, 2.76, 2.68 and 2.72 nm respectively. It can be seen that the increase in the d spacing so obtained is lesser as compared to the Brabender mixed samples.

Thermal stability of β phase samples was also analyzed as in the case of the Brabender mixed samples. It was observed that the samples so obtained retained the β phase on annealing at 125°C and 185°C.

It is observed in the present case that the increase in the d spacing with percentage of clay follows a specific trend in both Brabender as well as TSE mixed samples. The maximum increase in d spacing has been observed in the case of 3% of clay. After this, there is a decrease in the d spacing in both the cases. This could be due to the large amount of polymer chains that are available for intercalation for the amount of clay. As the clay percentage increases the ratio of available polymer to clay decreases from the previous case and hence there might be a decrease in the d spacing

Figure 4.5.3 shows the composition dependence of d spacing prepared using twin-screw extruder and Brabender batch mixer.

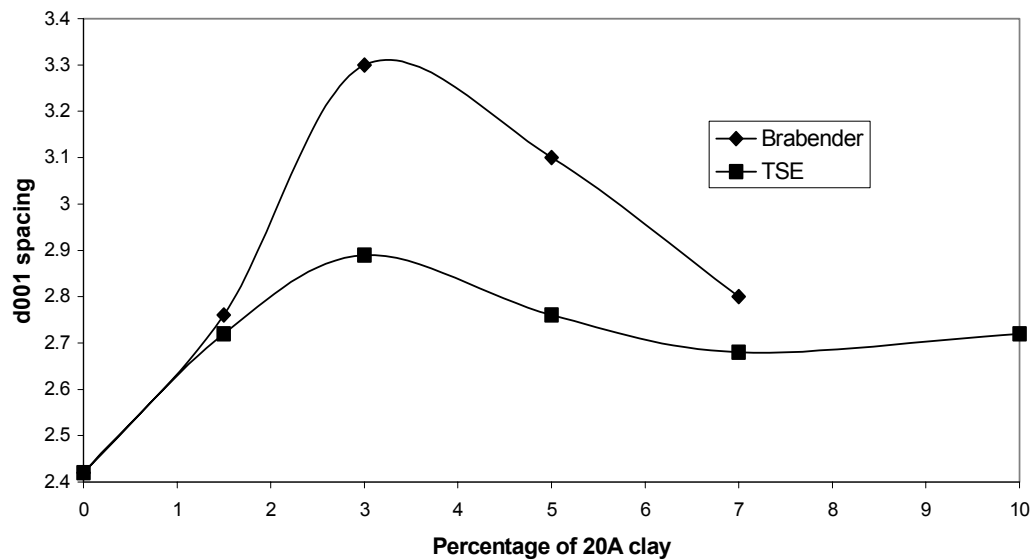


Figure 4.5.3: Comparison of d spacing with percentage of clay for samples prepared using batch mixer and twin-screw extruder

4.5.1.2 Optical Microscopy

Optical micrographs of extruded nanocomposites are as shown in figures 4.5.4 and 4.5.6.

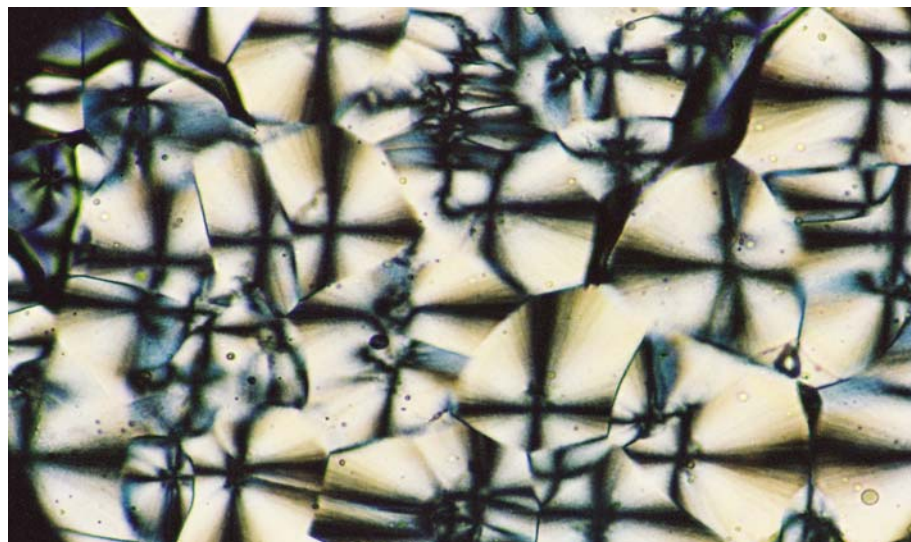


Figure 4.5.4: Optical Micrograph of PVDF at 148 °C. Magnification 32X



Figure 4.5.5: Optical Micrograph of TPN1.5 at 150 °C. Magnification 32X



Figure 4.5.6: Optical Micrograph of TPN7 at 157 °C. Magnification 32X

It can be seen from the optical micrographs, that the inclusion of 1.5% of clay itself produces very small spherulites, which is comparable to those of 7% clay included samples. The reduction in the spherulitic size for higher percentage of clay was similar to those observed for PN samples.

4.5.1.3 Differential Scanning Calorimetry

4.5.1.3.1 Melting and Non-isothermal Crystallization

The non-isothermal heating and cooling scans were carried out in order to ascertain the melting point, crystallization temperature, and the percentage crystallinity of the extruded samples. The parameters are mentioned in the table 4.5.1.

Table 4.5.1: Non-isothermal melting and crystallization parameters of extruded PVDF and PVDF (SOLEF 1008)/20A nanocomposites

Sample identification	Melting Temperature, T_m ($^{\circ}\text{C}$)	Crystallization Temperature, T_c ($^{\circ}\text{C}$)	$\Delta T = (T_m - T_c)$ ($^{\circ}\text{C}$)	ΔH_f (Cal/g)	Crystallinity (%)
TP	175.8	138.8	37	13.8	55
TPN1.5	181.5	150.3	31.2	12.9	52
TPN3	180.0	149.4	30.6	13.3	53
TPN5	182.1	150.5	31.6	11.0	44
TPN7	182.3	149	33.3	11.1	44
TPN10	182.5	150.3	32.2	12.2	49

It can be seen that the melting peak temperature and crystallization peak temperature increases from that of the pristine extruded PVDF. This in conjunction with the X- ray diffraction results show β phase. There is a small decrease in crystallinity observed in the nanocomposites.

4.5.1.3.2 Isothermal Crystallization

The isothermal crystallization curves of extruded PVDF/20A nanocomposites are as shown in the figure 4.5.7.

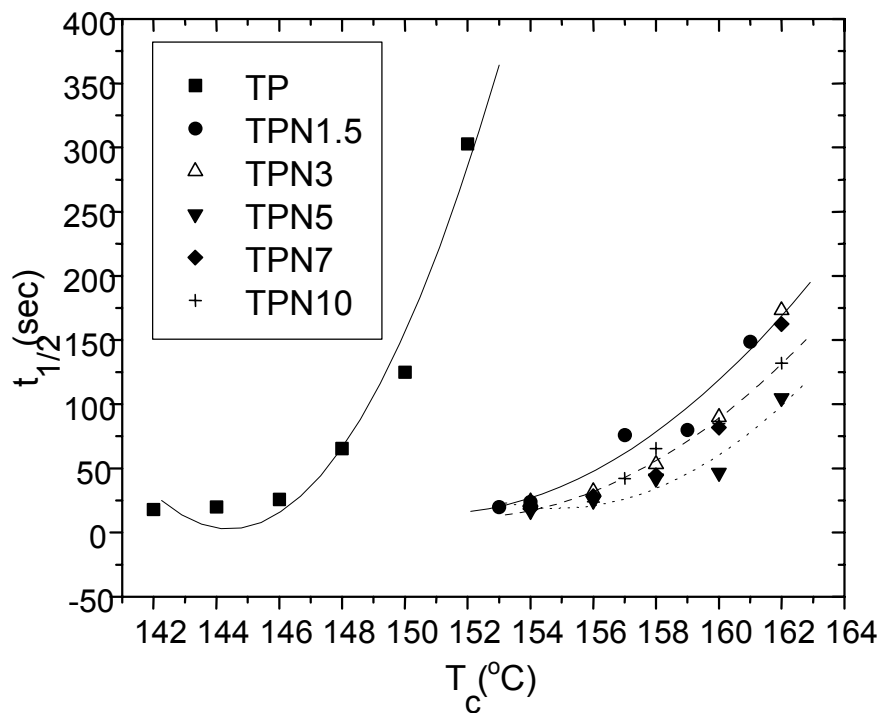


Figure 4.5.7: Isothermal crystallization of PVDF (SOLEF 1008)/20A extruded nanocomposites

The $t_{1/2}$ values were calculated from the Avrami equation as in the previous cases and are plotted against crystallization temperature. The crystallization curves show a shift in the crystallization temperatures of nanocomposites as compared to pristine polymer. The nanocomposites crystallizes in the same range of temperature and the rate of crystallization is accelerated. The temperature dependence of the nanocomposites is weak as compared to pure polymer indicating better interaction between polymer and clay ⁽²⁷⁾. This was not observed in case of Brabender mixed samples.

4.5.1.4 Static Mechanical Properties

4.5.1.4.1 Tensile Properties

The tensile modulus of the injection-molded samples was measured and the results are summarized in the table 4.5.2. Yield stress decreases from 48.3 Mpa for pristine polymer to 41.5 MPa for 10% clay content. It can be seen that there is no increase in the modulus upto 5% of clay. For 7% and 10% inclusion of 20A clay there is an increase of modulus by 10 and 22% respectively.

Table 4.5.2: Static Mechanical properties of extruded PVDF (SOLEF 1008)/20A Clay Nanocomposites

Sample Code	Tensile stress at yield (MPa)	Tensile Modulus (MPa)	Percentage increase in modulus (%)	Impact Strength (J/m)	
				Notched	Unnotched
TP	48.3	1583		268	NB
TPN1.5	48.2	1326		268	NB
TPN3	47.0	1442		291	NB
TPN5	44.8	1616	2	264	NB
TPN7	43.0	1749	10	267	NB
TPN10	41.5	2054	22	235	877

4.5.1.4.2 Impact Properties

The notched and unnotched impact strength of PVDF and PVDF (SOLEF 1008) nanocomposites are shown in the table 4.5.2. The notched impact strength of PVDF is 268 J/m. This slightly decreases except in case of 3% of clay. This decrease in the notched impact strength is associated with the propagation of crack in the presence of stress concentration points. The unnotched impact strength does not change, implying that the mechanism of initiation and hence the propagation of crack remains unaltered in the case of nanocomposites. Even in the case of 10% clay loading the energy required is quite high.

4.5.1.5 Dynamic Mechanical Analysis

Dynamic mechanical analysis is often used to study the relaxations in polymers. The analysis of storage modulus and $\tan \delta$ curves is very useful in ascertaining the performance of the sample under stress and temperature.

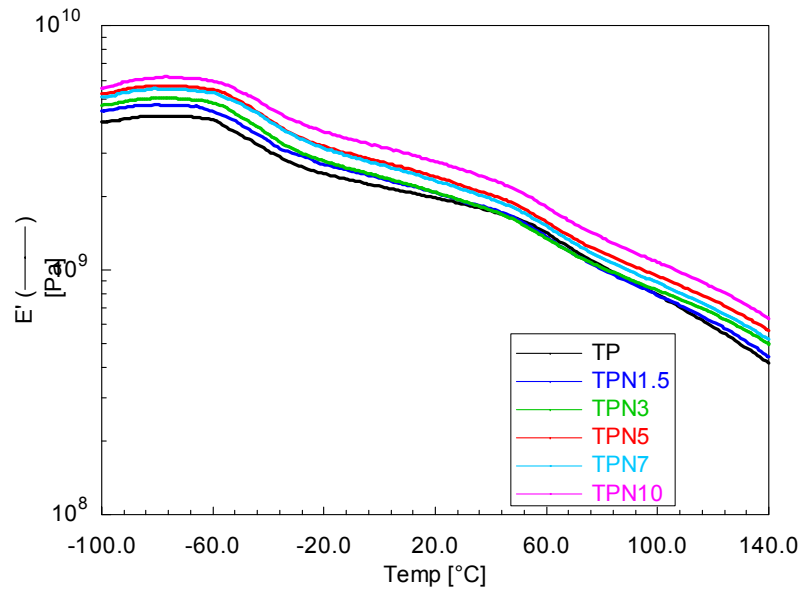


Figure 4.5.8: Temperature dependence of storage modulus (E') for extruded PVDF (SOLEF 1008) and PVDF (SOLEF 1008)/20A clay nanocomposites

Figure 4.5.8 shows the storage modulus vs. temperature graph of PVDF and PVDF/20A nanocomposites. Increase in the modulus is observed in the whole range of temperature for the higher percentages, where as for low percentage of clays the increase in modulus above room temperature is comparatively less. The E_c'/E_p' of the nanocomposites at two temperatures one below glass transition ($-100\text{ }^\circ\text{C}$) and one above the glass transition ($30\text{ }^\circ\text{C}$) is shown in the table 4.5.4. It shows that the modulus increases in both the regions indicating the dispersion of the clay layers in the polymer matrix. The values of E_c'/E_p' obtained for the extruded samples were lesser than the Brabender mixed samples (table 4.2.3).

Table 4.5.3: E_c'/E_p' values of extruded PVDF (SOLEF 1008)/20A at different temperatures

Sample code	E_c'/E_p'		
	At -100 °C	At 30 °C	At 100 °C
TPN1.5	1.11	1.12	1.01
TPN3	1.17	1.03	1.06
TPN5	1.31	1.20	1.21
TPN7	1.28	1.15	1.13
TPN10	1.38	1.37	1.38

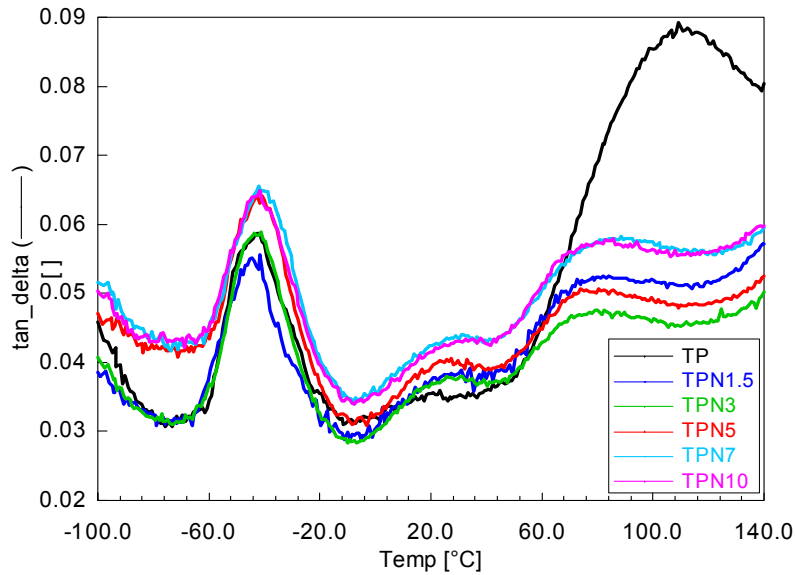


Figure 4.5.9: Tan δ vs. temperature curves for extruded PVDF (SOLEF 1008) and PVDF (SOLEF 1008)/20A clay nanocomposites

Tan δ vs. temperature of PVDF and PVDF/20A nanocomposites is as shown in the figure 4.5.9. The T_g slightly shifts to higher values with the clay percentage, indicating the hindered co-operative motion of the polymer chains. The height of the T_g peak marginally decreases for 1.5% of clay and for higher percentage of clays the peak increases, which is due to an increase in amorphous fraction. The constrained amorphous fraction peak, which is observed at around 20°C, also increases with

percentage clay. The crystalline relaxation of the chains (α transition) decreases as indicated by the high temperature peak height and is shifted to lower temperatures in nanocomposites as compared to PVDF. This shift may be attributed to the changes in crystalline morphology of PVDF in PVDF/clay nanocomposites.

4.5.1.6 Melt Rheology

Rheological study is used as a tool to measure the formation of nanocomposite.

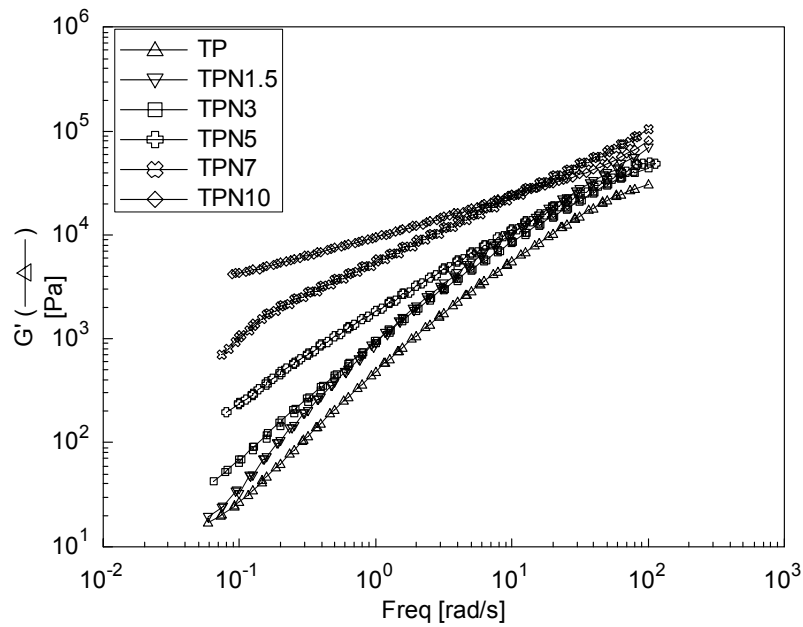


Figure 4.5.10: Master curve overlay of storage modulus (G') of extruded PVDF (SOLEF 1008) and PVDF (SOLEF 1008)/20A shifted to 210 °C

The measurement of G' , G'' and η^* over a range of frequency and temperature and producing the Master curve by Time Temperature Superposition is the general method adopted to find any microstructure changes during the nanocomposite formation. The master curve overlay of G' produced by Time Temperature superposition at a reference temperature 210°C is as shown in the figure 4.5.10. The frequency dependence goes on decreasing as the clay percentage

increases. For low percentage of clays, the slope in the terminal frequency region is quite closer to that of the pristine polymer. Above 5% of clay, the terminal slope increases and it reaches a maximum for 10% clay. This is due to intercalation as well as good dispersion of the clay.

Slope of G' does not change much indicating the absence of any exfoliated structures. It is interesting to note that for PN5 the G' slope and n was observed to be 0.88 and 0.2497 respectively indicating intercalated structure formation. However for TPN5 the values were 1.0306 and 0.1628 respectively indicating the lesser extent of intercalation.

4.6 Conclusions

Nanocomposites of PVDF with 20A clay are obtained by mixing it in batch mixer as well as Twin-screw extruder. The twin-screw extruded samples show lesser values of d spacing as compared to batch mixer. Formation of β phase is observed in both samples. The calculated values of lattice parameters for PVDF/20A samples prepared in batch mixer show good agreement with the β phase values provided in the literature. Non-isothermal crystallization samples prepared in batch mixer as well as twin-screw extruder show increase in melting point and crystallization temperature and decrease in crystallinity. Isothermal crystallization shows increase in rate of crystallinity. In the extruded nanocomposites, the temperature dependence of $t_{1/2}$ is weaker indicating better interaction between polymer and clay. Dynamic mechanical analysis indicates increase in storage modulus of samples prepared in twin-screw extruder as well as Brabender mixed samples. However, the extent of increase in storage modulus of twin-screw extruded samples was lesser as compared to the samples prepared in Brabender batch mixer. Rheological studies of nanocomposite indicate that the slope of G' and G'' are lower than pristine polymer. The slope of η^* (n) increases with increase in clay content. These two observations confirm the network formation of clay layers. Comparison of PVDF/20A and PVDF/6A nanocomposites using E_c'/E_p' and effective volume fraction shows that the 20A has optimum modifier concentration in order to form a nanocomposite with PVDF. PVDF/ Na^+ nanocomposites forms an unintercalated microcomposite. In

case of PVDF/Na⁺, which is a microcomposite PVDF crystallized in α phase. The formation of β phase in nanocomposites was attributed to the nanosize dispersion of clay layers in the PVDF matrix.

References

1. L. Priya, J. P. Jog, *Journal of Polymer Science: Part B: Polymer Physics*, **40**, 1682 (2002)
2. R. A. Vaia, E. P. Giannelis, *Macromolecules*, **30**, 8000 (1997)
3. R. A. Vaia, K. D. Jandt, E. J. Kramer, E. P. Giannelis, *Chemistry of Materials*, **8**, 2628 (1996)
4. P.H. Nam, P. Maiti, M. Okamoto, T. Kotaka, N. Hasegawa, A. Usuki, *Polymer*, **42**, 9633 (2001)
5. J. Ren, A.S. Silva, R. Krishnamoorthy, *Macromolecules*, **33**, 3739 (2000)
6. R. Gregorio Jr., M. Cestari, N.Chaves, P. S. Nociti, J. A. Mendonca, A. A. Lucas, Poly(vinylidene fluoride) phases and morphology (Effect of crystallization conditions), *The polymeric materials encyclopedia*, 1996, CRC Press
7. R. Gregorio, M. Cesari, N. Chaves, P.S. Nociti, J.A. Mendonca, A.A. Lucas, in *The Polymeric materials encyclopedia*, CRC press, Inc, 1996
8. H. Nagawada, Y. Ishida, *Journal of Polymer Physics*, **11**, 2153 (1973)
9. S.S. Hambir, N.N. Bulakh, P. Kodgire, R.A. Kalgaonkar, J.P. Jog, *Journal of Polymer Science Part B: Polymer Physics*, **39**, 446 (2001)
10. Y. Ke, C. Long, Z.Qi, *Journal of Applied Polymer Science*, **71**, 1139 (1999)
11. P.B. Messersmith, E.P. Giannelis, *Chemistry Of Materials*, **46**,1719 (1999)
12. J. Chang, D.K. Park, K.J. Ihn, *Journal Polymer Science Part B: Polymer Physics*, **39**, 471 (2001)
13. P. Kodgire, R. Kalgaonkar, S.S. Hambir, N.N. Bulakh, J.P. Jog, *Journal Of Applied Polymer Science*, **81**, 1786 (2001)
14. B. Hoffmann, J. Kressler, G. Stoppelmann, Chr. Friedrich, G. M. Kim, *Colloid Polymer Science*, **278**, 629 (2000)
15. Ren, A. S. Silva, R. Krishnamoorti, *Macromolecules*, **33**, 337 (2000)
16. R. Krishnamoorti, E. P. Giannelis, *Macromolecules*, **30**, 4097 (1997)
17. F.Yang, Y.Ou, Z.Yu, *Journal of Applied Polymer Science*, **69**, 355 (1998)
18. S. Lanceros-Mendez, M. V. Moriera, J. F. Mano, V. H. Schmidt, G. Bohannan, *Ferroelectrics*, **273**,15, (2002)

19. D. Shah, P. Maiti, E. Gunn, D. F. Schmitt, D. D. Jiang, C. A. Batt, E. P. Giannelis, *Advanced Materials*, **16**, 1173 (2004)
20. R. Wagener, T. J. G. Reisinger, *Polymer*, **44**, 7513 (2003)
21. S. Y. Gu, J. Ren, Q. F. Wang, *Journal of applied polymer science*, **91**, 2427 (2004)
22. N. Sukupiom, C.O. Oriakhi, M.M. Lerner, *Materials Research Bulletin*, **3**, 325 (2000)
23. K.Y. Kim, H. Kim, J.W. Lee, *Polymer Engineering and Science*, **41**, 1963 (2001)
24. V. V. Ginzburg, A. C. Balazs, *Advanced Materials*, **12**, 1805 (2000)
25. A. Dufresne, J.Y. Cavaille, *Journal Polymer Science Part B: Polymer Physics*, **36**, 2211 (1998)
26. Y.T. Lim, J.H. Park, O.O. Park, *Journal of Colloidal and Interface Science*, **245**, 198 (2002)
27. D. M. Lincoln, R. A. Vaia, R. Krishnamoorti, *Macromolecules*, **37**, 4554 (2004)

Chapter 5
PVDF (HYLAR 460)/Clay
Nanocomposites:
Properties and Creep
Studies

Chapter 5

5 PVDF (HYLAR 460)/Clay Nanocomposites: Properties and Creep Studies

5.1 Introduction

In the previous chapter PVDF (SOLEF 1008)/20A nanocomposites were found to exhibit significant property improvements. In this chapter we present results of study of nanocomposites prepared using different grade of PVDF. The HYLAR 460 grade of PVDF homopolymer was used for the experiments. The sample code and compositions are presented in table 5.1.1.

Table 5.1.1: Sample code and compositions of extruded PVDF (HYLAR 460)/20A nanocomposites

Weight percentage of 20A	Sample code
0	P0
1.5	P1.5
3	P3
5	P5
7	P7
10	P10

5.2 Results and Discussion

5.2.1 Structure of Nanocomposites

5.2.1.1 X-ray Diffraction

Figure 5.2.1 compares the XRD patterns of PVDF (HYLAR 460)/20A nanocomposites. The organically modified clay exhibits a well-defined d_{001} peak at 2.5 nm. For the nanocomposites P1.5 and P3 the d_{001} peak of the clay shifted to 3.2 and 3.3 nm respectively. As clay percentage increases to 5, 7 and 10 weight percentage, the d spacing shifted to lower angles corresponding to of 2.9, 3.0 and 2.8 nm, respectively. However, it is higher than the d spacing of 20A. This observed

increase in the d_{001} spacing can be attributed to the intercalation of PVDF into the intergallery spacing of clay^(1, 2, 3, 4).

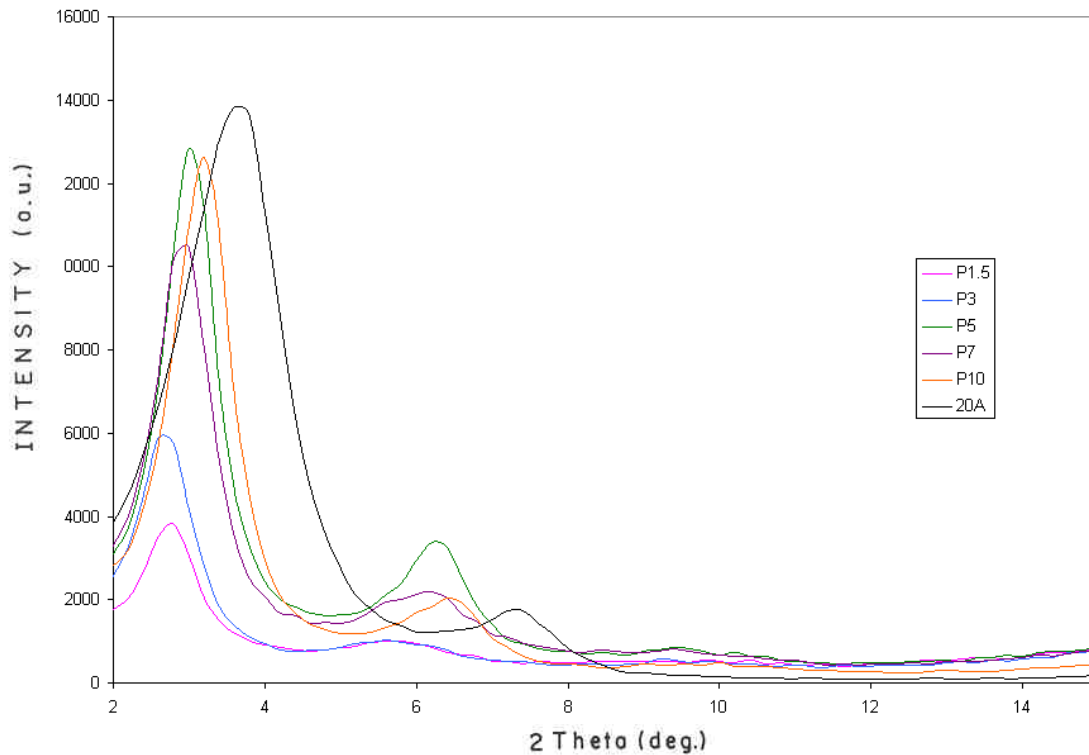


Figure 5.2.1: XRD of 20A and PVDF (HYLAR 460)/20A extruded Nanocomposites

The structure of PVDF was also examined using WAXD. The XRD pattern of the PVDF (HYLAR 460)/clay nanocomposites showing α phase of for PVDF (HYLAR 460) and β phase of PVDF in PVDF (HYLAR 460) nanocomposites is as shown in figure 5.2.2. This observation is similar to that of PVDF (SOLEF 1008) nanocomposites^(7, 8). This observation leads us to the conclusion that the β phase of PVDF can be induced by dispersed clay layers for both grades of PVDF. The stability of β phase PVDF was also confirmed by annealing experiments.

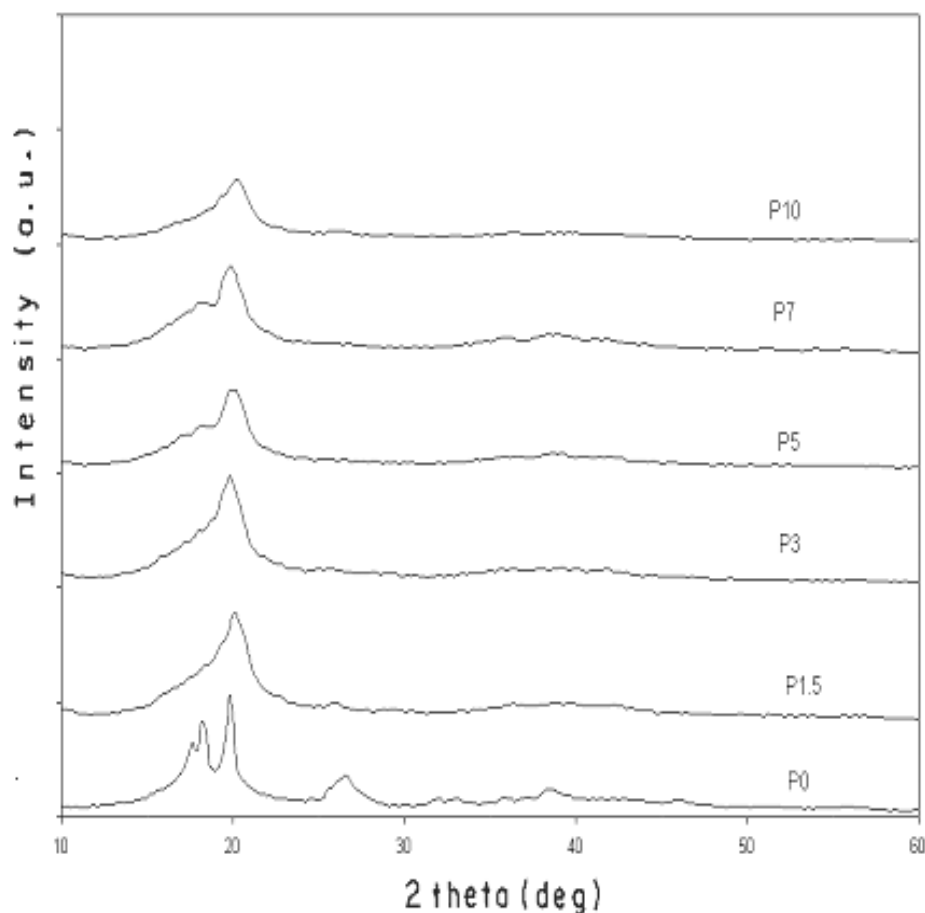


Figure 5.2.2: XRD showing α phase of pristine PVDF (HYLAR 460) and β phase of PVDF in extruded PVDF (HYLAR 460)/20A nanocomposites

5.2.1.2 Transmission Electron Microscopy

The dispersion of clay layers in nanocomposites can be visualized qualitatively from transmission electron micrographs. Transmission electron micrograph of 7% 20A in PVDF (HYLAR460) is shown in the figure 5.2.3. It shows that there are dispersed clay layers in the polymer matrix along with a few tactoids. In this case also lesser contrast between polymer and clay is observed due to the lesser density difference between the polymer and the clay.

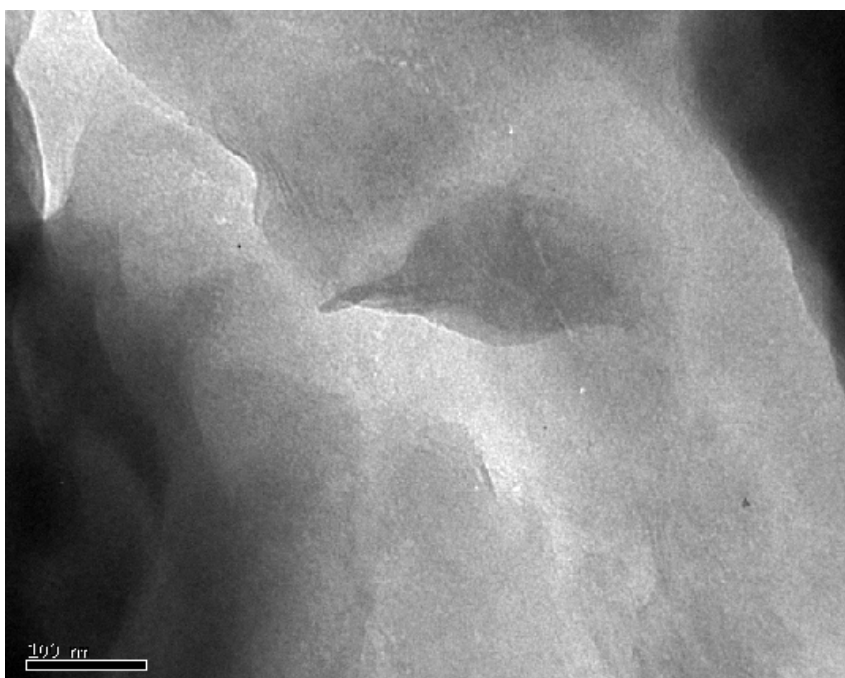
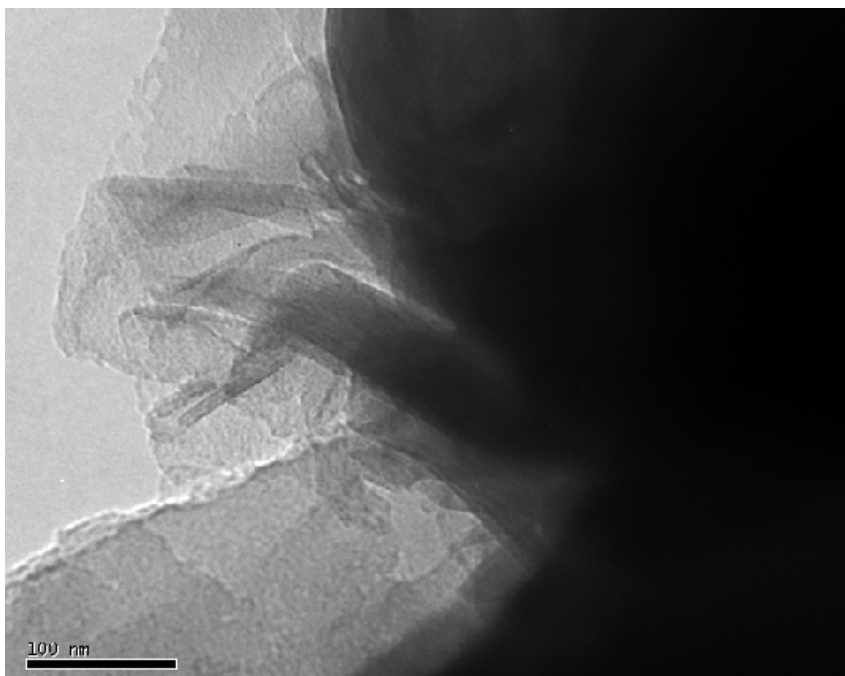


Figure 5.2.3: Transmission electron micrograph of P7 nanocomposite

5.2.2 Morphology

PVDF (HYLAR 460) samples crystallize into smaller size spherulites as can be seen from figure 5.2.4. The nanocomposites formed have smaller, not well-defined spherulites even at 1.5% clay content (figure 5.2.5). Higher clay content nanocomposites show even lesser size. This observation suggests that the clay layers act as nucleation agent.

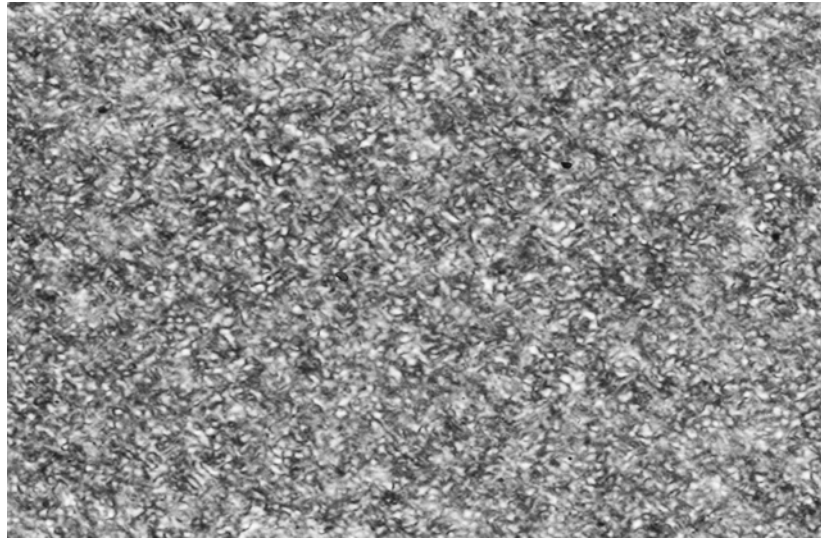


Figure 5.2.4: Optical Micrograph of P0 crystallized at 141 °C. Magnification 32X

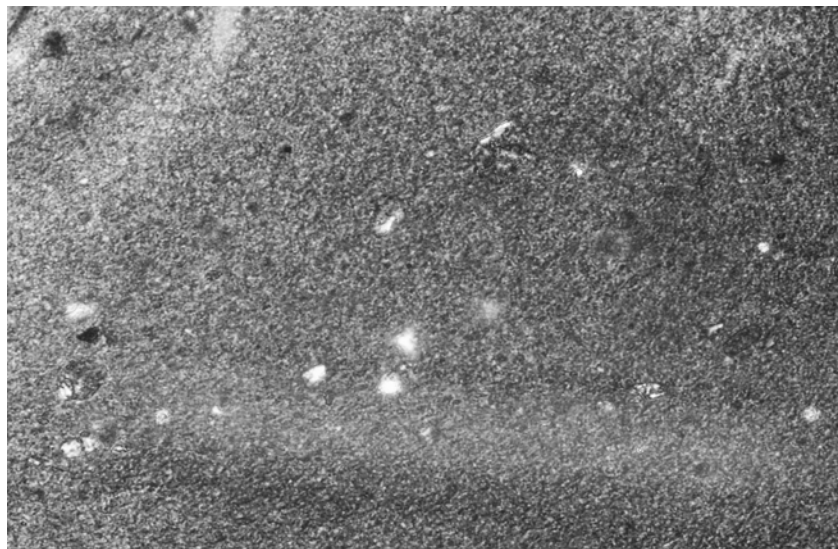


Figure 5.2.5: Optical Micrograph of P1.5 crystallized at 144 °C. Magnification 32X

5.2.3 Thermal Properties- Differential Scanning Calorimetry

Table 5.2.1 shows the melting temperature (T_m), crystallization temperature (T_c), and degree of crystallinity of the PVDF in PVDF/clay nanocomposites. The temperature of crystallization increased by approximately 4 to 6 °C. The melting point however did not show an increase as observed in the case of SOLEF 1008. It has been reported by Prest and Luca ⁽⁷⁾ and Shah et al ⁽⁸⁾ have reported that the β phase of PVDF did not show an increase in melting point in PVDF and PVDF /clay nanocomposites, respectively. The heat of fusion decreased from 10.1 to 5.2 Cal/g implying the decrease in crystallinity of PVDF in the case of nanocomposite. There is approximately 50% decrease in the crystallinity.

Table 5.2.1: Non-isothermal melting and crystallization parameters of extruded PVDF (HYLAR 460) and PVDF (HYLAR 460)/20A clay nanocomposites

Sample Code	Melting Temperature (°C)	Crystallization Temperature (°C)	$\Delta T = (T_m - T_c)$ (°C)	ΔH_f (Cal/g)	Crystallinity (%)
P0	163	134	30	10.1	40
P1.5	164	138	26	10.2	41
P3	164	137	27	6.8	30
P5	165	140	25	6.4	26
P7	164	140	24	5.2	20
P10	166	139	27	5.2	21

5.2.4 Static Mechanical properties

5.2.4.1 Tensile Properties

Tensile properties were measured for injection molded samples and the results of tensile testing are presented in the table 5.2.2. Tensile stress at yield decreases on addition of clay. It can be seen from the table, that there is an increase in the tensile modulus with increase in clay percentage. It is approximately 30% at 7-weight % loading of clay and approximately 48% at 10-weight % loading of clay. The elongation decreases from 25% for pristine polymer to 8% for 10-weight % clay

included nanocomposite. In case of the nanocomposites the increase in the tensile modulus of clay layers confirm the reinforcing effect of the clay.

Table 5.2.2: Static Mechanical properties of extruded PVDF (HYLAR 460)/20A Clay Nanocomposites

Sample Code	Tensile stress at yield (MPa)	Tensile Modulus (MPa)	Percentage increase in modulus (%)	Impact Strength (J/m)	
				Notched	Unnotched
P0	58.7	1217	-	461	NB
P1.5	57.2	1210	0	359	NB
P3	52.1	1519	25	353	NB
P5	49.5	1550	27	240	NB
P7	45.8	1589	30	137	983
P10	42.6	1806	48	79	816

* NB indicates No Break

5.2.4.2 Impact Properties

PVDF has very highnotched impact energy of 461 J/m. This could be due to high crack propagation energy. But, addition of the organically treated clay reduces the crack propagation energy of PVDF. At 3% loading of clay 25% decrease in the impact strength is observed. Above this loading the impact strength significantly decreases and at 10% loading of clay, impact strength decreases to 17%. No break is observed in the un-notched impact sample till 5% loading of clay. Above 5% of clay there is a break observed but the energy required is comparatively on the higher side. This indicates that the mechanism of initiation and hence the propagation of crack remains almost unaltered in the case of nanocomposites upto 5% loading of clay.

Static mechanical properties of extruded HYLAR 460 nanocomposites show 25 to 48% increase in the modulus and a corresponding decrease in the impact strength.

5.2.5 Dynamic Mechanical Analysis

Figure 5.2.6 shows the storage modulus of PVDF and PVDF/20A nanocomposite over a temperature range of -100 to 140 °C. The PVDF nanocomposites showed higher values of elastic modulus over the entire range of temperature^(9, 10).

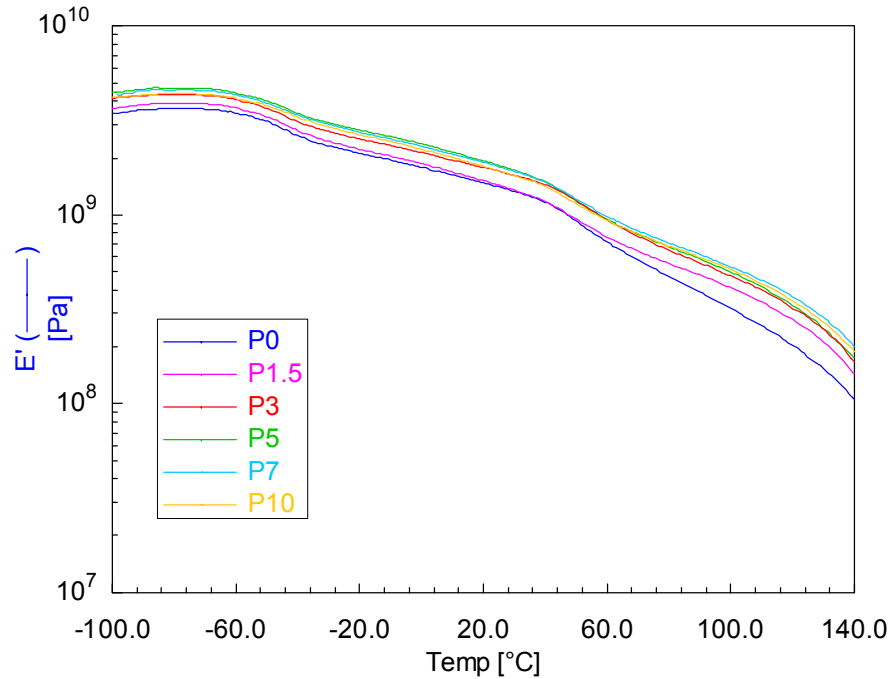


Figure 5.2.6: Temperature dependence of storage modulus (E') for PVDF (HYLAR 460) and PVDF (HYLAR 460)/20A nanocomposites

Table 5.2.3 presents the ratio of dynamic modulus of the composite with respect to pristine polymer (E_c'/E_p') values at three temperatures. As can be seen from the table, the increase in modulus is approximately equal in glassy and room temperature indicating the reinforcing effect of clay. The E_c'/E_p' values in the rubbery state (above the crystalline transition) also exhibit 30 to 70%. This increase in modulus above T_g is attributed to the reinforcing effect of clay layers on the polymer matrix.

Table 5.2.3: E_c'/E_p' values of extruded PVDF (HYLAR 460)/20A at different temperatures

Sample code	E_c'/E_p'		
	At $-100\text{ }^\circ\text{C}$	At $30\text{ }^\circ\text{C}$	At $100\text{ }^\circ\text{C}$
P1.5	1.07	1.07	1.30
P3	1.21	1.21	1.51
P5	1.31	1.29	1.57
P7	1.26	1.28	1.70
P10	1.24	1.20	1.64

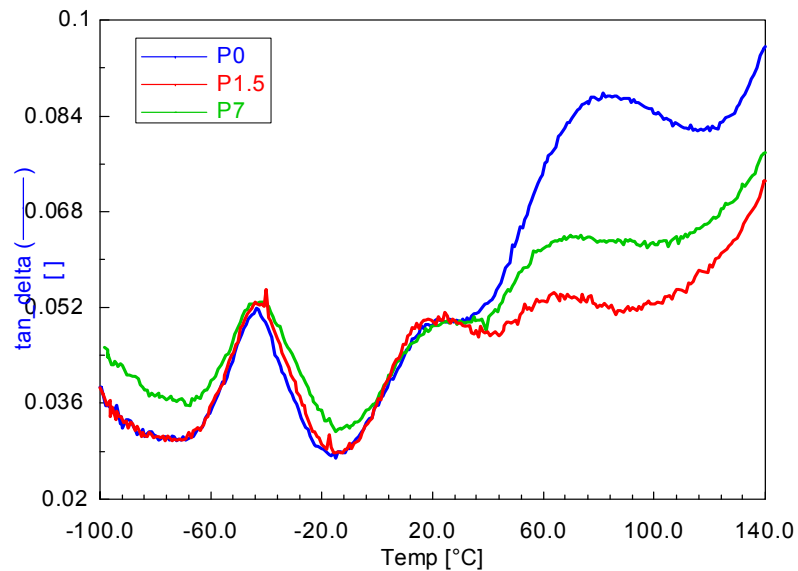


Figure 5.2.7: $\tan \delta$ vs. temperature curves for PVDF (HYLAR 460) and PVDF (HYLAR 460)/20A clay nanocomposites

Figure 5.2.7 shows the $\tan \delta$ curves of PVDF and PVDF/20A nanocomposites. The $\tan \delta$ curve of the nanocomposite shows three peaks corresponding to temperatures -46 , 20 , and $80\text{ }^\circ\text{C}$. These peaks corresponds to the three relaxation mechanisms and are reported to be similar for α and β phase of PVDF⁽¹¹⁾. The peak at $-46\text{ }^\circ\text{C}$ corresponds to the glass transition temperature. This is due to the cooperative segmental motions of the amorphous chains. In the case of

nanocomposites as well as the pristine polymer, this temperature is similar. The high temperature peak at 80 °C is due to the liberation of polymer chains in crystalline region and is ascribed to the α transition. In case of nanocomposites, it can be observed that the peak corresponding to this crystalline α transition shifts towards lower temperature by approximately 10-15 °C and it has lower amplitude as compared to pristine PVDF. This shift in the position of α transition can be attributed to changes taking place in the crystalline morphology during the formation of the nanocomposites. It has been observed in the non-isothermal melting and crystallization studies that the nanocomposites exhibit lower crystallinity as compared to the pristine polymer^(5, 6). Thus, the reduction in the crystalline relaxation peak could be due to lower crystallinity in the nanocomposites. The third peak at 20 °C occurs as a shoulder in the case of pristine PVDF and a well-defined peak in the nanocomposites. This may correspond to the relaxation of chains of reduced mobility. This includes the highly constrained tie chains and amorphous segments from chain folding surfaces in the case of pristine polymers. In the case of nanocomposites, there is an additional contribution to the constrained amorphous fraction due to the intercalated polymer chains and the polymer chains adhered on the clay surface. Tsgaropoulos and Eisenberg observed similar additional transitions in polymers filled with silica particles⁽¹²⁾. The increase in the constrained amorphous fraction intensity could be due to the intercalated polymer and immobilized surface chains. This increase in constrained amorphous fraction also accounts for the increase in effective volume of the clay in the nanocomposites and hence an increase in the storage modulus of the nanocomposites^(13, 14).

5.2.6 Creep Studies

Polymer and polymer composites being viscoelastic materials, their applications are mainly dependant on the long-term strength or load bearing capacity and dimensional stability of the materials. Creep is a common phenomenon for engineering materials. Creep studies can predict long-term properties of materials namely, strength and dimensional stability. Viscoelastic creep and creep rupture behaviors are critical properties required to assess long-term properties of the

material and for selection of materials for different applications such as aerospace, biomedical, and civil engineering. Creep test is a powerful tool to study the plastic deformation mechanism from which micro structural processes can be studied. High-performance polymer composites exhibit time dependant degradation in modulus (creep) and strength (creep rupture) as a consequence of viscoelasticity of the polymer matrix. In general creep of a polymer is a result of interactions of one or more of the events such as viscoelastic deformation, primary and secondary bond rupture, shear yielding and crazing (which involves chain slippage, void formation and growth). Depending on the polymer and its structure and their interaction with conditions such as temperature, stress, and time, different events will dominate the process. The role of filler in altering the matrix deformation properties can be evaluated based on creep tests.

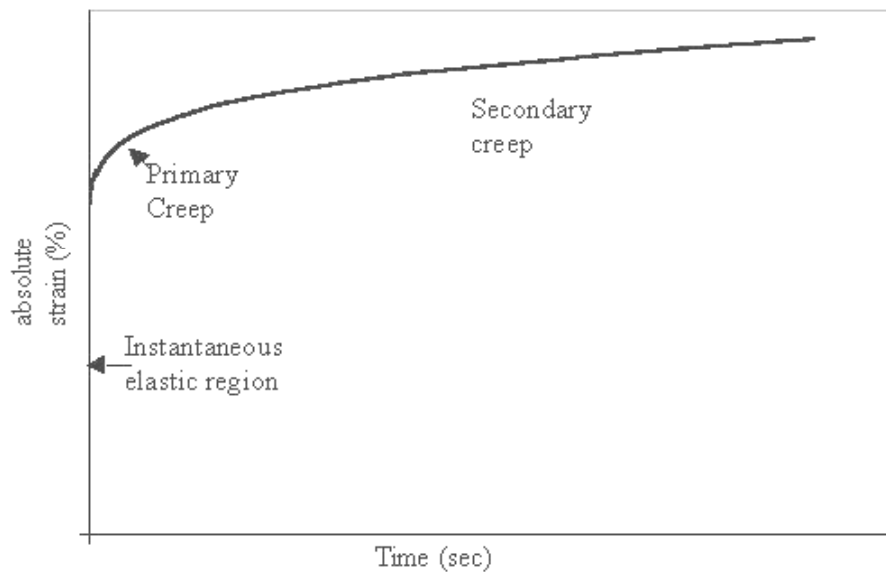


Figure 5.2.8: Creep curve of PVDF at 15% yield stress

A typical creep curve is shown in the figure 5.2.8. The time versus strain graph shows three specific regions viz., the instantaneous elastic region, primary creep and the secondary creep region. The primary creep region is characterized by the decreasing strain rate caused by increase in defect density, which causes reduction in the chain mobility. In the secondary creep region, the strain rate is

constant because of chain relaxation and local rearrangements. The tertiary region of the creep mechanism (not shown in the figure 5.2.8) occurs at very long periods of testing. Here the creep rate increases very rapidly and finally creep fracture occurs.

Strain vs. time graph of pristine PVDF and one of the nanocomposites P7 at 15% yield stress, at room temperature and high temperature are shown in the figures 5.2.9 and 5.2.10, respectively. Similar strain vs. time graph was obtained for other nanocomposites also. It is reported that at higher yield stresses, matrix yielding is the dominant mechanism and structure of the nanocomposite does not influence creep mechanism⁽¹⁵⁾. In order to understand the interaction between the polymer and clay the lower region of stresses are useful. Similar studies were carried out by Mano et al⁽¹¹⁾. Longer creep times are required for studying the creep fracture mechanism.

Strain reached in the instantaneous elastic region in PVDF is more than that attained in the case of nanocomposites at room temperature as well as at 100°C. This indicates that the elastic deformation of PVDF is significantly altered by the presence of clay layers. PVDF/clay nanocomposite exhibit lower strain as compared to pristine PVDF at different stresses and temperatures. This reduction in the absolute strain relates to the dimensional stability of the nanocomposites. At room temperature, which is above the glass transition temperature but below the secondary glass transition and relaxation of the constrained amorphous fraction, the free amorphous phase will contribute to the instantaneous elastic behavior. Since, at this temperature the cooperative segmental motion associated with the main chains is completely relaxed, the macroscopic behavior is due to the crystalline and constrained amorphous fraction contribution. The reduction of the chain mobility due to the presence of the clay layers can be observed from the fact that the secondary creep region in the case of nanocomposites is attained in a very short time.

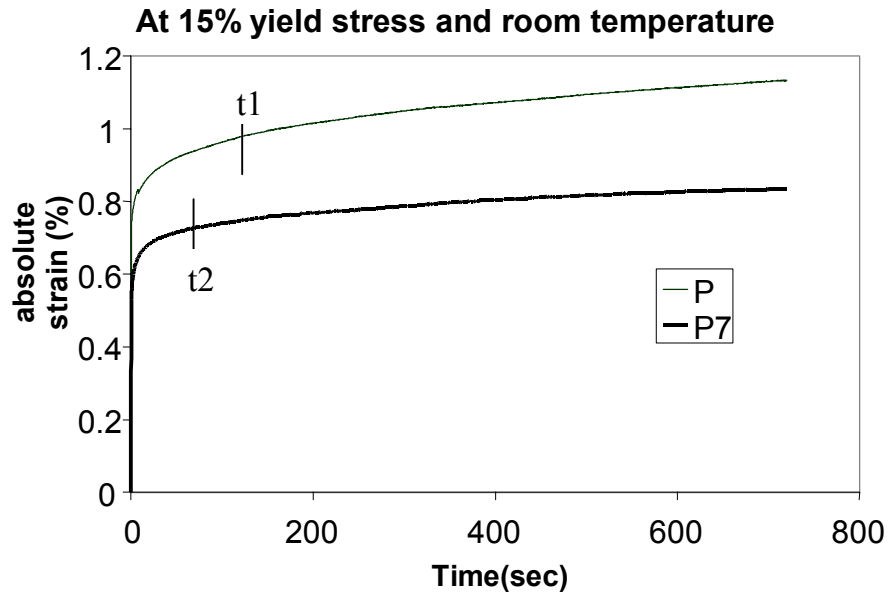


Figure 5.2.9: Strain vs. time graph for PVDF and one nanocomposite (P7) at room temperature for 15% of yield stress

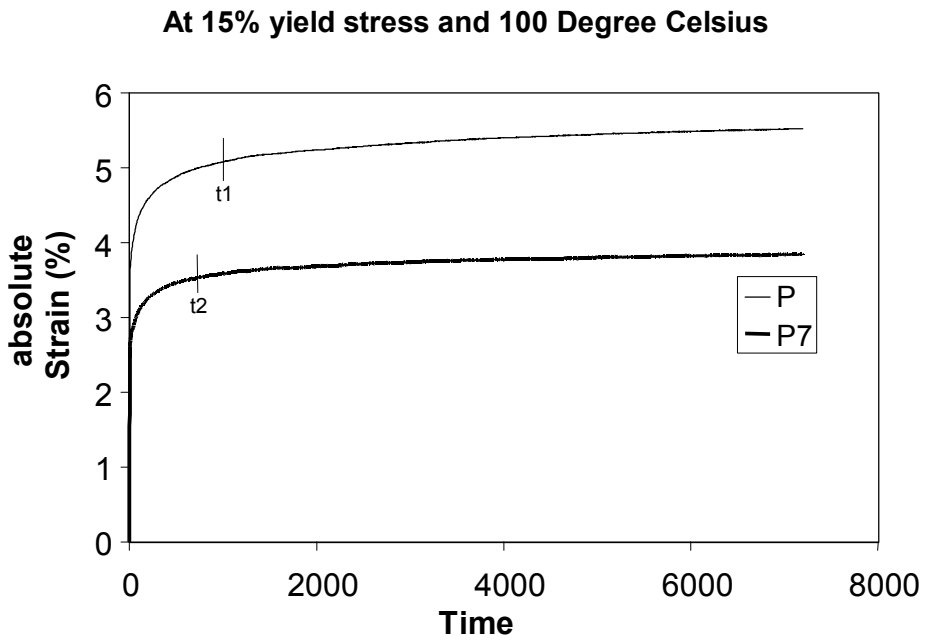


Figure 5.2.10: Strain vs. time graph for PVDF and one nanocomposite (P7) at 100°C for 15% of yield stress

The primary creep region time is determined by fitting linear graph in the steady state region and finding the deviation from the linear region. Time t_1 and t_2 corresponds to the primary creep time of pristine polymer and that of the nanocomposite as shown in figure 5.2.9 and 5.2.10. The primary creep region for the nanocomposite is less ($t_2 < t_1$) as compared to the pristine polymer. This could be due to the increase in defect density or reduced chain mobility. The reduced chain mobility could be due to the dispersion of the clay layers. The slope of the secondary creep region is higher for PVDF than the nanocomposites. This reduction in the secondary creep region slope is also because of the constraint in the chain relaxation. The clay layers act as reinforcing agents thus reducing creep. Zhang et al have recently reported that the nanometer sized TiO_2 is used for improving the creep behavior of Nylon 6, 6 at room temperature and elevated temperatures ⁽¹⁶⁾. The pristine α and β PVDF has a similar plastic deformation mechanism. Therefore, the difference in the creep is essentially because of the formation of the nanocomposite and not because of the change in crystal form ⁽¹¹⁾.

At higher temperature (100 °C), the slopes of creep curve for PVDF and nanocomposites are different. This could be either due to change in structure or due to different creep mechanism in PVDF and PVDF/clay nanocomposites. It has reported that α and β phase of PVDF have similar creep mechanism ⁽¹¹⁾. Therefore, the slope modification is either due to transition and propagation of micro voids or an increase in the site for nucleation because of micro structural modifications ^(17, 18).

In case of PVDF/clay nanocomposite, the clay layers are known to act as nucleation centers ^(5, 6). This might create large energy barriers to motion and hence might retard the relaxation process leading to inhibition of creep mechanism. The improved creep performance of PVDF/Clay nanocomposites as compared to PVDF also suggests good interface formation between clay layers and PVDF. Indeed, it has been reported that there is a direct correlation between interface and creep performance. When the interface is softer than the matrix, the creep strength and load carrying capacity of the composite may be greatly reduced by its presence, whereas when there is a hard interface improved creep strength is observed. We have

observed such an improved creep performance for PVDF/clay nanocomposites confirming a good interface⁽¹⁹⁾.

Creep mechanism can be expressed in terms of compliance. Creep curves of all polymers can be fitted to an equation of the form

$$D(t) = D_0 \exp(Bt)^{1/3} \tag{5.1}$$

where

$D(t)$ - is the creep compliance at time t

D_0 - short-term compliance constant. The short-term compliance constant is independent of stress and thermal history and varies only with temperature. Short-term compliance constant accounts for the instantaneous behavior of the sample.

B - is a constant, which defines the rate at which creep processes occur. It increases with an increase in temperature or stress or an increase in the molecular mobility due to shorter aging time^(20, 21).

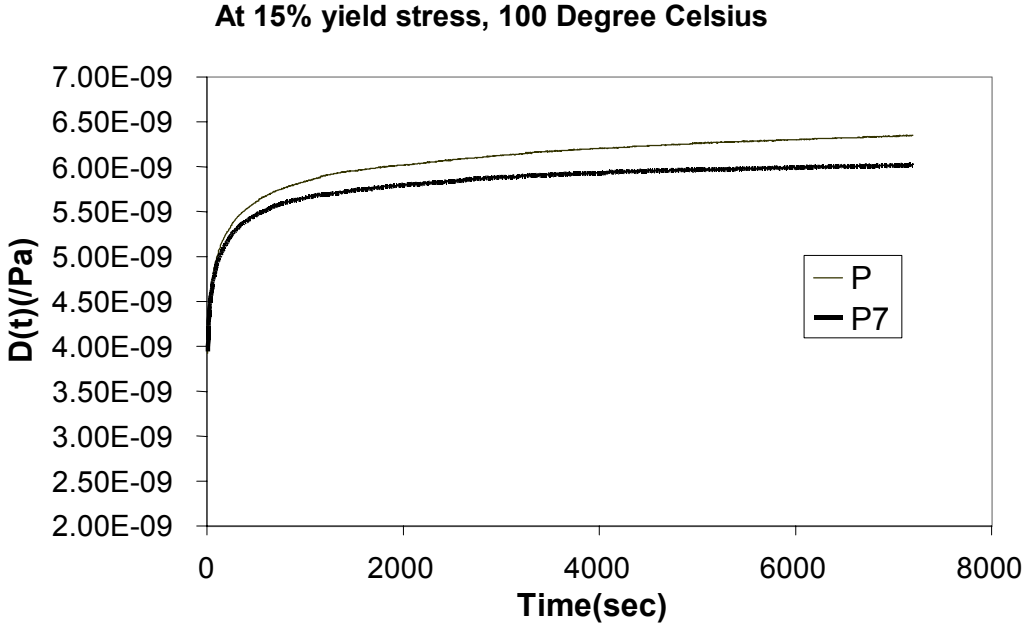


Figure 5.2.11: Time vs. compliance at 100 °C at 15% yield stress for PVDF and one nanocomposite (P7)

Creep compliance vs. time for PVDF and PVDF/clay nanocomposites are shown in figure 5.2.11. At room temperature the glassy constrained phase is responsible for the deformation mechanism, whereas above 80°C (i.e., secondary

glass transition represented as T_g' or α transition) the whole polymer is in rubbery state. The decrease in creep compliance of nanocomposites as compared to that of the pristine polymer at room temperature and 100°C might be because increase in the resistance to chain mobility. Raghavan and Meshii⁽²²⁾ have shown that for a polymer/fiber reinforced system the changes in the creep behavior i.e. change in the creep magnitude and rate could be due to increasing resistance to co-operative chain segmental mobility of the polymer chains. Similarly the observed decrease in the creep compliance of the nanocomposites as compared to the pristine PVDF at room temperature as well as at 100 °C can be ascribed to the resistance to the mobility of polymer chains.

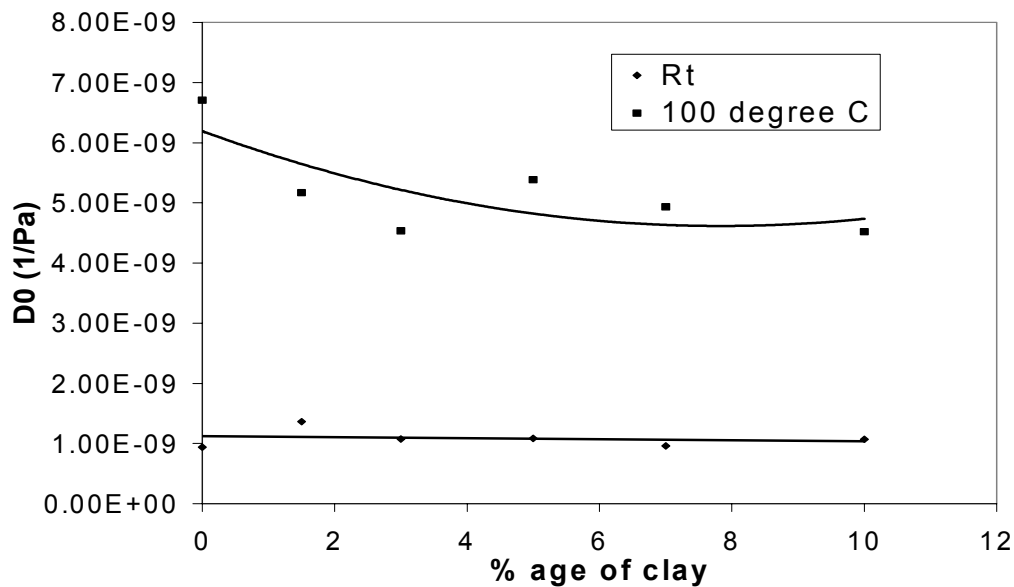


Figure 5.2.12: Comparison of short-term compliance constant (D_0) as function of percentage of clay and temperature

At room temperature the short-term compliance constant remains almost same (figure 5.2.12), where as at 100°C there is a decrease in the value as compared to the pristine polymer. The constant nature of the short-term compliance constant shows that, at room temperature the free amorphous fraction, which contributes to the instantaneous elastic behavior, is almost a constant and whatever changes occur

are due to the variation in quantities of crystalline and constrained amorphous fraction and network of clay layers.

5.3 Conclusions

PVDF (HYLAR 420)/20A nanocomposites were prepared by melt extrusion process. These nanocomposites exhibit intercalated structure as evidenced by X-ray diffraction and Transmission electron microscopy. PVDF crystallizes in β phase in the nanocomposites and its stability is confirmed in annealed samples. The inclusion of clay results in significant reduction in crystallinity. The static and dynamic mechanical testing shows significant increase in modulus. Creep studies at Room Temperature and 100°C shows that the resistance to creep in polymer/clay nanocomposites greatly improves due to the presence of nano-clay layers. The dispersion of nano-clay in the polymer matrix affects both elastic as well as inelastic regions. The primary creep region is of shorter time for the nanocomposites. The slope of the secondary region at higher temperature (100°C) varies for the nanocomposite as compared to PVDF. Further, the creep compliance decreases on addition of clay, which is attributed to the network formation and to the reinforcing effect of the clay layers in polymer/clay nanocomposites.

References

1. R.A. Vaia, E.P. Giannelis, *Macromolecules*, **30**, 8000 (1997)
2. R.A. Vaia, K. D. Jandt, E. J. Kramer, E. P. Giannelis, *Chemistry of Materials*, **8**, 2628 (1996)
3. P.H. Nam, P. Maiti, M. Okamoto, T. Kotaka, N. Hasegawa, A. Usuki, *Polymer*, **42**, 9633 (2001)
4. J. Ren, A.S. Silva and R. Krishnamoorthy, *Macromolecules*, **33**, 3739 (2000)
5. L. Priya, J.P. Jog, *Journal of Polymer Science Part B: Polymer Physics*, **40**, 1682 (2002)
6. L. Priya, J.P. Jog, *Journal of Polymer Science Part B: Polymer Physics*, **41**, 31(2003)
7. W.M. Prest Jr., D. J. Luca, *Journal of Applied Physics*, **49**, 5042 (1978)
8. D.Shah, P. Maiti, E.Gunn, D. F. Schmidt, D. D. Jiang, C. A. Batt, E. P. Giannelis, *Advanced Materials*, **16** (2004)
9. J. Chang, D.K. Park, K.J. Ihn, *Journal of Polymer Science Part B: Polymer Physics*, **39**, 471(2001)
10. P. Kodgire, R. Kalgaonkar, S.S. Hambir, N.N. Bulakh, J.P Jog, *Journal of Applied Polymer Science*, **81**, 1786 (2001)
11. J. F. Mano, J. L. Lopes, R.A. Silva, W. Brostow, *Polymer*, **44**, 4293 (2003)
12. G. Tsagaropoulos, A.Eisenberg, *Macromolecules*, **28**, 6067-6077 (1995)
13. Y.T. Lim, J.H. Park, O.O. Park, *Journal of Colloidal and Interface Science*, **245**, 198 (2002)
14. Y.T. Vu, J.E. Mark, L.H. Pham, M. Engelhardt, *Journal of Applied Polymer Science*, **82**, 1391 (2001)
15. X. Kornmann, Ph. D. Thesis, Lulea University of Technology, Sweden, 2001
16. Z. Zhang, J. Yang, K Friedrich, *Polymer*, **45**, 3481 (2004)
17. S. Elkoun, C. G'ssell, L. Cangemi, Y.Meimon, *Journal of Polymer Science Part B: Polymer Physics*, **40**,1754 (2002)
18. J. Li, G. J.Weng, *Composites*, **27 B**, 589 (1996)
19. Y.T. Vu, J.E. Mark, L.H. Pham, M. Engelhardt, *Journal of Applied Polymer Science*, **82**, 1391 (2001)

20. J. C. Arnold, V.E.White, *Materials Science and Engineering*, **A197**, 251 (1995)
21. L. C. E. Struik, *Polymer*, **2**, 962 (1980)
22. J. Raghavan, M. Meshii, *Composites Science and Technology*, **57**,1673 (1997)

Chapter 6
Conclusions and Scope for
Future Work

Chapter 6

6 Conclusions and Scope for Future Work

6.1 Conclusions

The objective of this work was to prepare the nanocomposites of PVDF using organoclays and to study the effect of clay on the structure and properties of PVDF. The nanocomposites were prepared using melt intercalation technique and characterized using various experimental techniques. The major results are summarized as follows.

1. The nanocomposites of PVDF were prepared by melt intercalation technique for the first time. Two commercially available organophilic clays, viz., Cloisite 6A and 20A which are treated with ditallow dimethyl ammonium salt was used for this study. The final properties of the PVDF nanocomposites were found to be dependant on the organic treatment of the montmorillonite clay used. It was also observed that the extent of intercalation depends on the modifier concentration. The nanocomposites exhibited significant improvement in the properties.
2. PVDF clay nanocomposites prepared by melt intercalation show intercalated structures as evidenced by X-ray diffraction pattern. The dispersion of nanometer sized clay layers was found to induce hetero phase nucleation as evidenced by the crystallization at higher temperature than the pristine polymer. Dynamic mechanical analysis indicated improved storage modulus over the temperature range studied and the extent of increase was dependent on clay percentage and modifier content. The glass transition temperature was found to increase by approximately 6-8 °C indicating restricted chain mobility in the nanocomposite. The $\tan \delta$ curves exhibited three peaks corresponding to T_g of the polymer, liberation of polymer chains in the crystalline region and release of constrained phase due to clay.
3. PVDF was found to crystallize in β form. PVDF crystallized in β phase in the PVDF/clay nanocomposites and this phase was found to be stable even after annealing at 185°C. The composite formed with untreated Na^+ clay and

PVDF, remained as a micro composite. Moreover, the crystal structure of PVDF was observed to remain in α phase. Hence it was concluded that the β phase formation is due to the crystallization of PVDF in the confined state.

4. In dielectric studies, it was observed that the real part of dielectric constant (ϵ') decreases in the whole range of frequencies with clay content. The decrease in ϵ' was attributed to the mobility decrease in the nanocomposites as compared to the pristine polymer matrix and to clay layers acting as hindrance to the dipole orientation. The relaxation behaviour of PVDF gets altered due to the β phase formation.
5. The creep studies of PVDF and PVDF/clay nanocomposites showed that the resistance to creep in polymer/clay nanocomposites improves due to the presence of nano-clay layers. The dispersion of nano-clay in the polymer matrix affects both elastic as well as inelastic regions. Creep compliance decreases on addition of clay, which is attributed to the network formation and to the reinforcing effect of the clay layers in the polymer/clay nanocomposites.
6. The formation of the nanocomposites is also shown for two grades of PVDF.

6.2 Scope for Future Work

One of the important observations was the formation of the β phase. The β phase of PVDF is of great interest as it exhibits various interesting physical properties like piezoelectricity and pyroelectricity. The formation of β phase in PVDF/6A and PVDF/20A nanocomposites may be attributed to the crystallization of PVDF in the confined state. Formation of β phase in PVDF/clay can be further investigated using techniques such as IR, ESCA, NMR etc. Stretching and poling of the nanocomposites can be studied to find the effect on dielectric constant.

Effect of orientation of clay and the size of the clay tactoids can be studied using 3-D XRD with possible correlations to the mechanical properties.

Havrilliak-Negami like model can be used for predicting the mechanical as well as dielectric behavior over a range of frequencies as well as temperatures. This and similar models can be developed and applied in order to predict the mechanical

and dielectric properties of the nanocomposites in general and for PVDF in particular. This will aid us in the designing and development of transducer technology using the nanocomposites.

The effect of other inorganic nano fillers can be explored and effect of the fillers on the structure and properties can be studied.

List of Publications

1. Poly(vinylidene fluoride)/Clay Nanocomposites Prepared by melt Intercalation: Crystallization and Dynamic Mechanical Behavior Studies, L. Priya, J. P. Jog, Journal of Polymer Science: Part B; Polymer Physics, Vol. 40, 1682-1689 (2002)
2. Intercalated Poly(vinylidene fluoride)/Clay Nanocomposites: Structure and Properties, L. Priya, J. P. Jog, Journal of Polymer Science: Part B; Polymer Physics, Vol. 41, 31-38 (2003)
3. Polymorphism In Intercalated PVDF/Clay Nanocomposites, L. Priya, J. P. Jog, Journal of Applied Polymer Science, Vol 89, 2036-2040(2003)
4. Creep Studies in PVDF/clay Nanocomposites, L. Priya, J. P. Jog, Communicated

Posters presented in conferences

1. Preparation and characterization of PVDF/Clay Nanocomposites, L. Priya, J. P. Jog, Polymer Nanocomposites 2001, International Conference on Polymer Nanocomposites Science and Technology, Montreal, Canada, 2001
2. Creep Studies in PVDF /Clay Nano-composites, L. Priya, J. P. Jog, Polymer Nanocomposites 2003, International Conference on Polymer Nanocomposites Science and Technology, Boucherville, Canada, 2003